2001

Characterization of corrosion fatigue damage in the fastener holes of a Boeing 707

Mary Chilton Latham
Lehigh University

Latham, Mary Chilton

CHARACTERI-ZATION OF CORROSION FATIGUE DAMAGE IN...

June 2001

CHARACTERIZATION OF CORROSION FATIGUE DAMAGE IN THE FASTENER HOLES OF A BOEING 707

by

Mary Chilton Latham

A Thesis

Presented to the Graduate and Research Committee

of Lehigh University

in Candidacy for the Degree of

Master of Science

in

Mechanical Engineering

Lehigh University

April 2001

This thesis is accepted and approved in partial fulfillment of the requirements for the Master of Science.

April 30, 2001

Date

Dr. Robert P. Wei
Thesis Advisor

Dr. Charles R. Smith
Chairperson of Department

ACKNOWLEDGMENT

I would like to express sincere gratitude to Professor Robert P. Wei for his support and guidance throughout this research. Professor Wei's experience in the field of fracture mechanics combined with his exemplary research and teaching skills has made this work both challenging and exciting. I would also like to thank Dr. D. Gary Harlow for his helpful discussions on topics pertaining to the previous work that was performed on these wing panels, which paved the way for the work in this thesis to be done.

Thank you to Mr. Arlan Benscoter, whose technical assistance with metallographic techniques was greatly needed and appreciated. I also wish to thank Dr. Evan J. Dolley for his help in the early stages of this research, Mrs. Shirley Simmons for her kind help during my graduate work, and Dr. Christopher F. Miller for his assistance during the past year.

I am grateful to the P.C. Rossin College of Engineering and Applied Science for providing me with a fellowship during my first year as a graduate student at Lehigh University. I am equally grateful to the National Science Foundation for awarding me a Graduate Research Fellowship which allowed me to complete this work.

I would also like to thank the professors at Bucknell University who assisted in providing me with a solid undergraduate Mechanical Engineering background.

Finally, I want to thank my parents, Joseph and Margaret Latham, for their constant love and support. They've always encouraged me to do my best, and in doing so have helped me understand that overcoming hurdles in life builds character. Thanks also to my sister Anne, who has taught me to live life to its fullest everyday.

TABLE OF CONTENTS

LIST OF TABLES

LIST OF FIGURES

ABSTRACT

This thesis presents the results from a detailed metallographic analysis for corrosion fatigue damage in the fastener holes from wing panels of a B707-321B aircraft. The aircraft accumulated 57,382 flight hours and 22,533 flight cycles in 24 years before being disassembled by the United States Air Force (USAF). The examinations included optical microscopy at magnitudes up to 200X to determine the size and distribution of the damage, followed by serial sectioning and scanning electron microscopy (SEM) to characterize their nature and geometry.

Damage in the fastener holes occurs as a result of localized corrosion (pitting) and subsequent corrosion fatigue cracking (CFC). It was postulated that damage in aluminum alloys develops from a hemispherical corrosion pit that transitions to a semi-circular crack and later to a through-thickness crack. Based on this postulate, a mechanistically based probability model was constructed and correlated to the observed surface damage in the fastener holes. From the surface observations however, it is not certain whether the actual damage is semi-circular. In addition, the model assumes a single dominant flaw in the material, whereas multiple cracks that link together to form one crack were observed on the surface. A more comprehensive metallographic analysis was conducted to determine the size and shape of CFC.

The actual damage in the fastener holes was characterized by serial sectioning to observe the three-dimensional shape of CFC. The largest crack was found to be 1.45mm in length with a maximum depth of 0.34mm. Non-destructive inspection (NDI)

techniques were explored, but the resolution of the techniques was found to be inadequate for characterizing the damage.

The results showed that not all damage is semi-circular in shape, and that the evolution and coalescence of multiple CF damage need to be modeled as part of a mechanistically based probability model. The model needs to be refined to include varying crack geometries and multiple crack growth behavior for more accurate fatigue life assessments.

CHAPTER 1 - INTRODUCTION

1.1 Research Motivation

Commercial and military aircraft are exposed to deleterious environments that result in corrosion fatigue (CF) during their years in service. While on the ground, aircraft are exposed to a humid environment at temperatures that cause the aluminum alloy to break down or corrode. In sheltered areas, localized corrosion pits form and their development is accelerated by the presence of chloride ions that may be present in moist environments. In addition, some aircraft use steel fasteners in the wing panels, which further promotes galvanic corrosion of the aluminum alloy.

During flight, aircraft undergo mechanical stresses (tensile and compressive bending stresses) that contribute to metal fatigue cracking. Since corrosion is strongly dependent on temperature and pH, it is not kinetically supported at high altitudes and thus fatigue primarily occurs during flight. The coupled effect of corrosion and fatigue cracking during repeated ground-air-ground flight cycles is the greatest structural concern that aging aircraft face.

Aircraft were initially designed with a design service objective (DSO) of 20 years, but many planes flying today are nearing or over 30 years of age due to economic factors. Improved models, therefore, are needed for use in life prediction and management of aging fleets of aircraft. The USAF is in the process of converting retired Boeing 707 (B707) aircraft into E-8C Joint Surveillance Target and Attack Radar Systems (J-STARS) aircraft. Left-hand wing sections of 2024-T3 aluminum alloy from two B707 aircraft were disassembled for damage inspection and analysis. One aircraft was a B707-

123 that accumulated 78,416 flight hours and 36,359 flight cycles after 30 years in service. The second aircraft was a B707-321B with 57,382 flight hours and 22,533 flight cycles following 24 years in service.

Previous studies conducted at Lehigh University on the B707-321B aircraft inspected the lower wingskin fastener and stiffener holes for pitting corrosion and fatigue cracks that appear as surface damage. The data were then used in the correlation of a mechanistically based probability model for estimating damage evolution, distribution, and accumulation for structural integrity assessments. While this preliminary inspection acknowledged that CF damage exists on the surface, further metallographic work is needed to accurately characterize the nature of actual damage in the fastener holes. Investigating the three-dimensional shape of CF in the fastener holes will allow improvements to be made in the existing mechanistically based probability model.

1.2 Problem Statement

Life prediction and management of aging aircraft requires accurate modeling of fatigue data for the evolution of damage in the structure. Earlier inspection of fastener holes in the lower wingskin of a B707 investigated only surface damage, upon which a mechanistically based probability model was made. Whether the model is representative of the actual evolution of damage is in question because the three-dimensional character of CF damage in these fastener holes has not been investigated. In particular, are the fatigue cracks in the fastener holes truly semi-circular in shape as modeled or are they of a different geometry? Also, the current model is based upon a single dominant flaw in

the material, but is this an accurate modeling method when multiple cracks have been observed in the fastener holes? It is necessary to investigate whether multiple cracks that are offset along the length of the fastener hole and form one crack can be modeled as a single dominant crack.

The objectives of this research are to experimentally determine through metallography the actual geometry of CF and the relevancy of multiple damage sites to a dominant crack model. Serial sectioning was performed along the damage in the fastener holes followed by geometry measurements and SEM work to verify the measurements and obtain micrographs of the cracks. The information gathered by characterizing the CF damage will provide basis for the development of a revised mechanically based probability model for more accurate fatigue life prediction and analysis.

1.3 Thesis Structure

Chapter 1 is an introduction that describes the motivation for performing the research, defines the problem statement, and states the fundamental objectives.

Chapter 2 discusses the technical and conceptual information related to this study and reviews the existing mechanistically based probability model that is relevant to the current research.

Chapter 3 describes the experimental procedures used to achieve the objectives stated in Chapter 1 and the subsequent observations. Specimen preparation, metallographic techniques, optical microscopy, and SEM are discussed.

Chapter 4 presents and discusses the experimental results of serial sectioning and

SEM on the fastener holes. The influence of the results upon the existing mechanistically based probability model is described.

Chapter 5 provides a summary of the thesis work and suggestions for future work.

CHAPTER 2 – BACKGROUND

2.1 Introduction

Aluminum alloys are susceptible to a damage evolution process that involves pitting corrosion and fatigue cracking. When coupled, CFC is a principal degradation mechanism that affects the structural integrity of commercial transport and military aircraft [1]. This chapter reviews localized corrosion (in the form of pitting) and fatigue cracking in order to provide a basic understanding of the processes that contribute to damage evolution. Fatigue cracking will be explained in greater detail to include the subjects of crack driving force, crack growth rate, and the transition from pitting to fatigue cracking. A discussion of the existing mechanistically based probability model used in predicting the evolution and accumulation of pitting corrosion and CF will follow. A summary of the preliminary inspection of fastener holes along the lower left-hand wingskin of a torn down B707 aircraft will conclude this chapter.

2.2 Damage Evolution Process in Aluminum Alloys

Aluminum alloys are subject to localized corrosion damage in the form of particle induced pitting corrosion when exposed to a deleterious environment [2]. This begins the damage evolution process that negatively affects the structural integrity of an engineered structure. Particle induced pitting corrosion in aircraft aluminum alloys is caused by dissolution of the matrix through galvanic coupling with constituent particles in the alloys [3]. Formed corrosion pits of a critical depth serve as nucleation sites for subsequent fatigue cracking. The damage evolution process is therefore considered to be dominated

by localized (or pitting) corrosion in the early stages, followed by fatigue crack growth in the later stages, as seen in Figure 2.1. For example, localized corrosion damage in the fastener holes of an aircraft is taken to be particle induced pitting corrosion. The aircraft fuselage is subject to a cyclic stress upon pressurization and depressurization during ground-air-ground flight cycles, while the wings undergo mechanical tensile and compressive bending stresses. These cyclic stresses cause fatigue cracks to nucleate at severe corrosion pits, resulting in corrosion fatigue, which is illustrated in Figure 2.2. The nucleating crack then undergoes a regime of chemically short and long crack growth until it is either detected and repaired, or results in a potentially catastrophic failure [4].

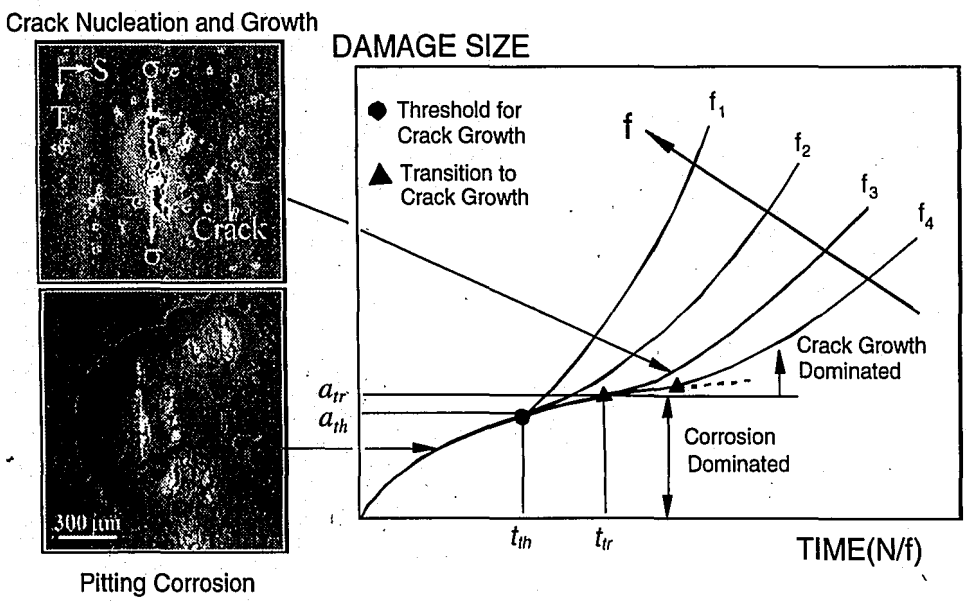

Figure 2.1: Schematic diagram of corrosion fatigue development [5].

by localized (or pitting) corrosion in the early stages, followed by fatigue crack growth in the later stages, as seen in Figure 2.1. For example, localized corrosion damage in the fastener holes of an aircraft is taken to be particle induced pitting corrosion. The aircraft fuselage is subject to a cyclic stress upon pressurization and depressurization during ground-air-ground flight cycles, while the wings undergo mechanical tensile and compressive bending stresses. These cyclic stresses cause fatigue cracks to nucleate at severe corrosion pits, resulting in corrosion fatigue, which is illustrated in Figure 2.2. The nucleating crack then undergoes a regime of chemically short and long crack growth until it is either detected and repaired, or results in a potentially catastrophic failure [4].

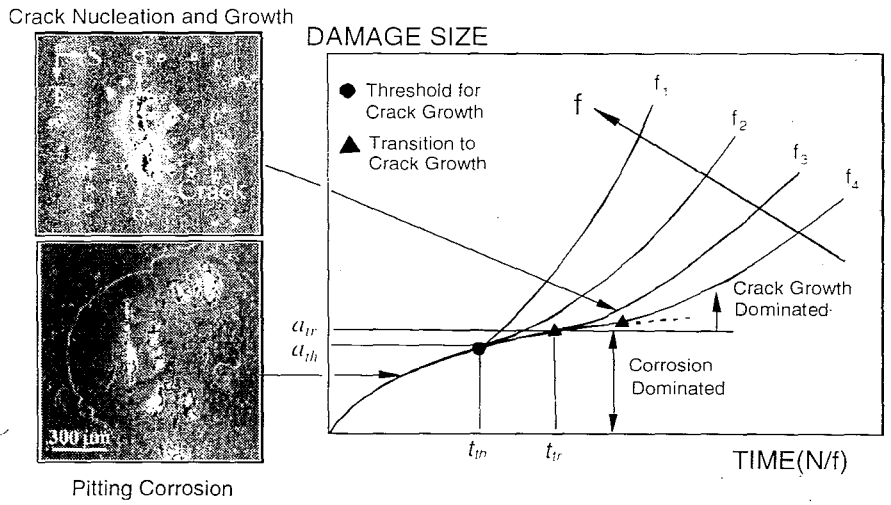

Figure 2.1: Schematic diagram of corrosion fatigue development [5].

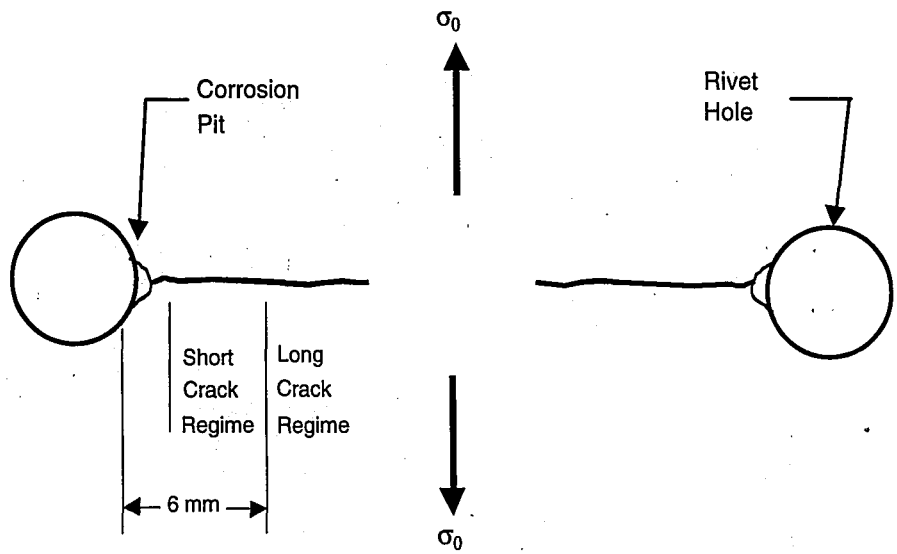

Figure 2.2: Damage evolution process in engineering materials susceptible to corrosion pitting and chemically short-crack growth behavior [4].

2.2.1 Pitting Corrosion

Pitting corrosion is a highly localized form of corrosion that results in material removal from discrete areas, thus contributing to the degradation of structural integrity. It is insidious and destructive because the attack is usually shielded from view or hidden by corrosion products [6].

Pitting in sheltered areas occurs as a result of the penetration of ions that break down a material's passive layer, or by an electrochemical reaction of galvanic coupling between two dissimilar metals in a conducting solution [6]. Since alloys are characteristically heterogeneous materials, galvanic coupling between constituent particles and the surrounding matrix promotes particle induced pitting corrosion in a deleterious environment. Particle induced pitting corrosion can be observed in Figure 2.3. Pitting corrosion depends strongly on temperature and solution pH. The pitting rate increases with an increase in temperature, and is higher in solutions that are more acidic (i.e., having a lower pH) [2].

Because of its widespread occurrence and damaging effects, pitting is an area of concern for engineering and industrial applications. Pitting corrosion has been known to affect the life of a material since the early 1900's [7-9]. Particle induced corrosion pits may reduce or eliminate the initial portion (or nucleation) of a material's fatigue life, thereby compromising its structural integrity. In addition, corrosion pits of a critical depth serve as sites for fatigue crack nucleation. The pit size at crack nucleation depends on the applied stress at that location and on the crack growth properties of the material [3]. When coupled with fatigue, CF is considered to be a principal degradation method.

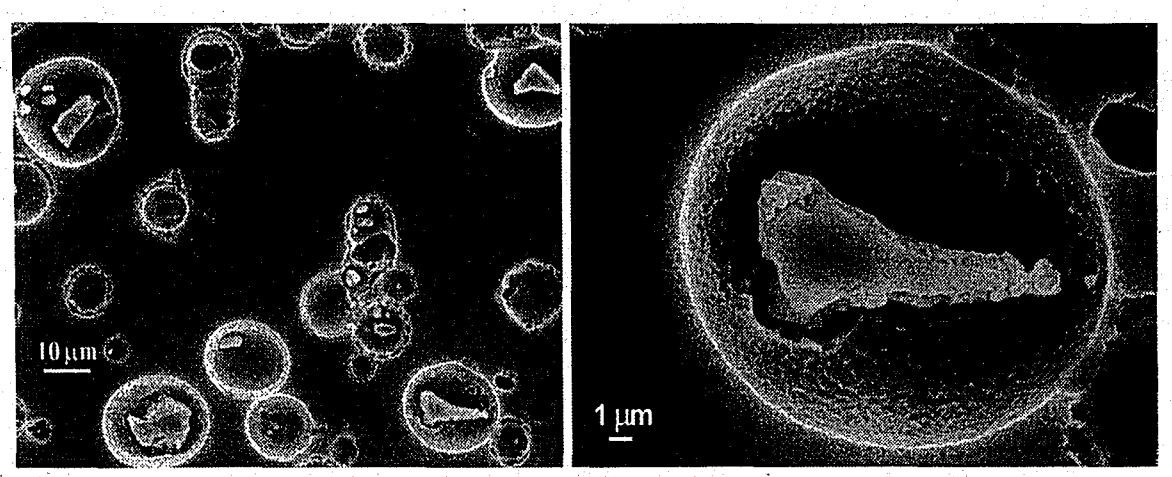

Figure 2.3: SEM micrograph showing pitting induced by constituent particles in 2024-T3 aluminum alloy [5].

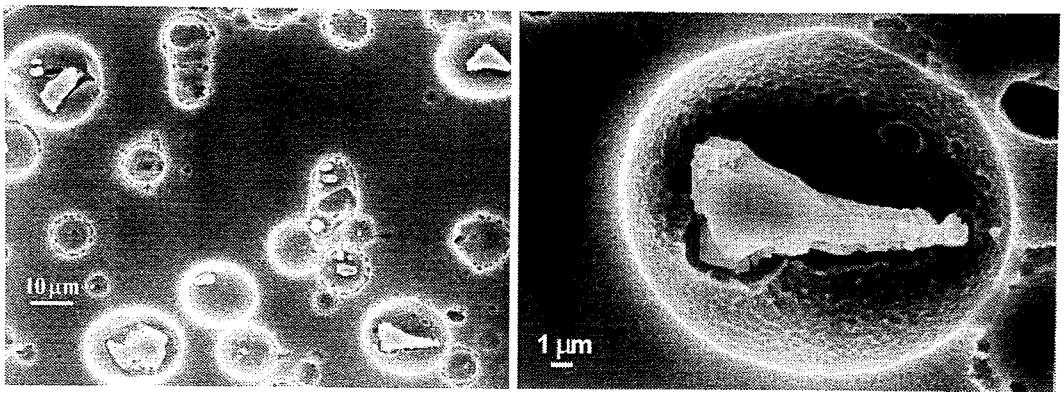

Figure 2.3: SEM micrograph showing pitting induced by constituent particles in 2024-T3 aluminum alloy [5].

2.2.1.1 Constituent Particles of 2024-T3 Aluminum Alloy

Severe localized pitting is attributed to the formation of local galvanic cells by clusters of constituent particles, which result in larger and deeper pits, as seen from the epoxy replications in Figure 2.4. Previous research of pitting corrosion on 2024-T3 aluminum alloy (the material from which the lower wingskin of the disassembled B707 aircraft is constructed) identified the anodic (actively corroding) and cathodic constituent particles using energy dispersive x-ray spectroscopy (EDS) in the SEM. Anodic particles in the 2024-T3 alloy are those that contain Al and Cu (Al_2Cu), or Al, Cu, and Mg (Al_2CuMg). Cathodic particles include Al, Cu, Fe, Mn, and sometimes Si, and are of the type $(Fe,Mn)_xSi(CuAl)_y$. The cathodic particles appear to be modified forms of Al_8Fe_2Si or $Al_{10}Mn_3Si$. The more detailed characterizations of the constituent particles were conducted by analytical electron microscopy (AEM) and x-ray microprobe analysis [10].

Experiments showed that particle density was approximately 3000 particles/mm^2, where nearly 75% of the particles in the 2024-T3 alloy were anodic, and thus tend to dissolve themselves. Particles of Al_2Cu and Al_2CuMg are nominally anodic with respect to the matrix, but behaved cathodically as a result of Cu deposition or dealloying to promote matrix dissolution with current densities of 0.2 and 0.18 mA/cm^2, respectively [11]. Particles containing Fe and Mn had a current density of 0.04 mA/cm^2 and were cathodic to both the matrix and pure aluminum, thereby promoting dissolution of the matrix and pure aluminum [10].

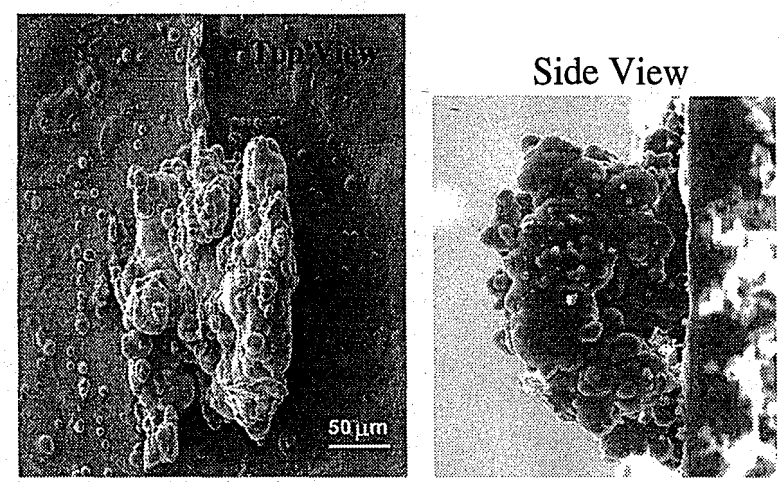

Figure 2.4: SEM micrographs of the epoxy replica of a severe corrosion pit in 2024-T3 aluminum alloy: (a) plan (bottom) and (b) elevation (side) view relative to the original pit [5].

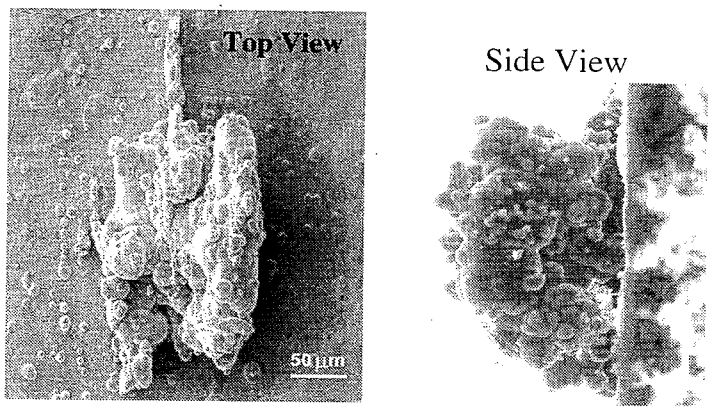

Figure 2.4: SEM micrographs of the epoxy replica of a severe corrosion pit in 2024-T3 aluminum alloy: (a) plan (bottom) and (b) elevation (side) view relative to the original pit [5].

2.2.2 Fatigue

Fatigue in a structure occurs as a result of cyclic stress (tensile and compressive) loadings. Fatigue cracking in the presence of corrosion is a principal degradation mechanism for material damage of structural components while in service. The influence of pitting corrosion on fatigue life was recognized early this century through the work of Haigh [7], Moore [8], and Gough and Sopwith [9].

The next sections will introduce the driving force for fatigue crack growth (FCG) and present two crack propagation methodologies. These methodologies differ in that one accounts for environmental factors while the other does not. Because of the known influence of pitting corrosion on fatigue life, it is important to consider environmental effects in order to make accurate fatigue life predictions. In addition, since corrosion pits transition into fatigue cracks, the criteria for this process is also discussed.

2.2.2.1 Driving Force for Fatigue Crack Growth

The stress intensity range, ΔK, is the driving force for FCG. It characterizes the magnitude of the stresses in the vicinity of the crack tip and is a function of crack length a, applied stress $\Delta\sigma$, and geometry β [4]. For cyclic loading, the SIF range ΔK, or K_{max}-K_{min}, is used to express the crack driving force.

$$\Delta K = \beta \Delta \sigma \sqrt{a} \tag{2.1}$$

The SIF is used for a crack opening condition of Mode I (tension) where linear elastic fracture mechanics (LEFM) assumptions are satisfied. For other loading conditions, such as Mode II (sliding), Mode III (tearing), and mixed mode loading, the SIF is not used. Rather, using the strain density factor range (ΔS) is suggested [12].

2.2.2.2 Fatigue Crack Growth Rate (FCGR)

Fatigue cracks grow as a result of cyclic loading. Over a number of cycles (ΔN) the crack length increases by Δa and the rate of growth may be expressed in the form below.

$$\frac{da}{dN} \approx \frac{\Delta a}{\Delta N} \tag{2.2}$$

A crack propagation methodology based on LEFM was introduced by Paris and Erdogan. This methodology uses a power-law representation of the relationship between crack growth rate and driving force.

$$\frac{da}{dN} = C(\Delta K)^m \tag{2.3}$$

where:

C = constant
m = slope
ΔK = crack driving force

The constant C and slope m are evaluated experimentally by using a log (ΔK) – log (da/dN) plot [13]. However, the power-law relationship is essentially empirical and cannot explicitly account for the influence of environmental factors, as noted in a critical review by Wei [14].

In order to account for environmental factors, corrosion fatigue crack growth (CFCG) in a corrosive environment has been extensively studied. Ideally, it is desirable to characterize the CF of a material to represent the fatigue life (N_f) or fatigue crack growth rate (FCGR) using mechanical, environmental, metallurgical, and geometrical variables. A summary of these variables is shown in Table 2.1. A power-law expression of the following form was developed to account for these variables [10].

$$\frac{da}{dN} = C_F \left(\Delta K - \Delta K_{th}\right)^{n_c} \tag{2.4}$$

where:

C_F = crack growth rate coefficient

ΔK_{th} = fatigue threshold

n_c = power law exponent

For these estimates, it is assumed that the initiating defect (a constituent particle or severe corrosion pit) is hemispherical in shape, and equivalent to a semi-circular crack with the same aspect ratio. The power-law relationship is then used to construct S-N curves which indicate the severe reduction in fatigue life that is associated with defects [10]. A reduction in fatigue life occurs as the size of the defect increases, or as the load frequency decreases. A decrease in loading frequency corresponds to an increase in time per loading cycle during which corrosion can occur, thereby producing larger corrosion pits [1].

To predict the number of cycles until failure, Equation 2.1 is substituted into Equation 2.4 and the resulting integration yields

$$N_F = \frac{2}{(n_c - 2)C_F \beta^2 \Delta\sigma^2 (\Delta K_i - \Delta K_{th})^{(n_c-2)}} \left[1 + \frac{(n_c - 2)\Delta K_{th}}{(n_c - 1)(\Delta K_i - \Delta K_{th})}\right] \tag{2.5}$$

where ΔK_i corresponds to the radius a_o of the initial pit. Previous research on the 2024-T3 aluminum alloy gave $n_c = 3.55$, $C_F = 1.3 \times 10^{-11}$ and 3.95×10^{-11} ($mcyc^{-1}$) $(MPa\sqrt{m})^{-3.5}$, and $\Delta K_{th} = 0.95$ and 0.5 ($MPa\sqrt{m}$) for air and 0.5 M NaCl solution, respectively. For a semi-circular crack, $\beta = 2.2/\sqrt{\pi}$ [1]. A graph of the fatigue life for 2024-T3 aluminum alloy is shown in Figure 2.5.

However, in order to make accurate fatigue life predictions, it is necessary to evaluate whether modeling the initial defect as a semi-circular crack is realistic. Therefore, an observation of actual damage is needed, which is performed in the current research. Until then, for geometries and loadings that are more complex, numerical integration using a specialized computational program such as AFGROW is necessary [15]. AFGROW is developed for FCG analysis and life prediction, and is able to accommodate varying specimen geometries, components, and cracks as well as constant and variable amplitude loading.

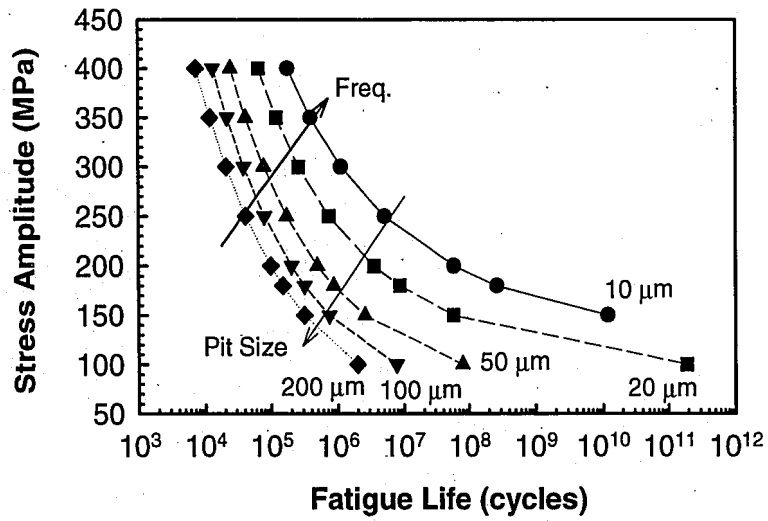

Figure 2.5: Estimated reduction in fatigue life given an increase in initiating pit size for the 2024-T3 aluminum alloy using a fracture mechanics approach [3].

Table 2.1: Significant Variables that Influence Corrosion Fatigue.

Mechanical Variables

- Maximum stress or stress intensity range, σ_{max} or K_{max}
- Cyclic Stress or stress intensity range, $\Delta\sigma$ or ΔK
- Stress ratio, or load ratio, R
- Cyclic load frequency, f
- Constant amplitude or variable amplitude loading
- State of stress
- Residual Stress

Geometrical Variables

- Crack size and dimensions with respect to component
- Crack geometry
- Stress concentrations

Metallurgical Variables

- Alloy composition
- Distribution of alloying elements and impurities
- Microstructure and crystal structure
- Heat treatment
- Mechanical working
- Preferred orientation of grains and grain boundaries
- Mechanical properties (strength, fracture toughness, etc.)

Environmental Variables

- Temperature, T
- Type of environment – gaseous, liquid, etc.
- pH
- Coatings, inhibitors, etc.

2.2.2.3 Transition from Pitting to Fatigue Cracking

The damage evolution process in aluminum alloys is dominated by localized pitting corrosion in the early stages, followed by FCG in the later states. Fatigue cracks may begin at sites of particle induced corrosion pits that are of a critical depth. Once a crack nucleates, it progresses as a semi-circular surface crack and transitions to a through-thickness crack, which can lead to a catastrophic fatigue failure unless otherwise detected and repaired [2].

The process of a pit transitioning into a fatigue crack is important in the estimation of CF life [16, 17]. It was found that the pit-to-crack transition size depends upon the cyclic load frequency. At lower frequencies, more time is allowed for corrosion pits to grow, which increases the pit-to-crack transition size. Higher frequencies reduce the time corrosion pits have to grow, which may be considered a pure fatigue problem. A nearly pure fatigue problem acts to eliminate corrosive effects so that the transition time to fatigue cracking is reduced. This frequency dependence reflects competition between pitting corrosion and fatigue [1]. At some point, there is a transition to pure fatigue where FCG outpaces pit growth.

Two transition criteria have been proposed and validated both experimentally and statistically for the transition from pitting to FCG.

$$\Delta K \geq \Delta K_{th} \tag{2.6}$$

$$\left(\frac{da}{dt}\right)_{crack} \geq \left(\frac{da}{dt}\right)_{pit} \tag{2.7}$$

The first transition criteria of Equation 2.6 states that the SIF of the crack must reach or

exceed the threshold SIF in order for FCG to occur [5]. The transition SIF for a semi-circular crack may also be given by the expression below [1].

$$\Delta K_{tr} = \left[\frac{\pi (1.12 k_t \Delta\sigma)^4 C_P \beta_{tr}^{\ 2}}{2 \quad C_F \Phi_{tr}^{\ 4}} \right]^{\frac{1}{n+4}} \left(\frac{1}{f} \right)^{\frac{1}{n+4}} \tag{2.8}$$

where:

k_t = stress concentration factor of the fastener hole

C_P = pit growth rate coefficient

β_{tr} = aspect ratio

Φ_{tr} = shape factor (elliptical integral)

f = frequency

Criteria 2 of Equation 2.7 states that fatigue cracking will occur when the crack growth rate is equal to or faster than the rate of pit growth.

2.3 Mechanistically Based Probability Model

Material degradation through localized corrosion and CFC reduce structural integrity of an engineered structure, therefore a validated method for the prediction of damage accumulation is critical for structural integrity assessments. A mechanistically based probability model enables predictions beyond the range of typical data to be made, and in doing so provides a quantifiable basis for risk assessment [18].

A mechanistic model of pitting corrosion and CF and the related probabilistic aspects of their evolution and distribution was modified by Harlow *et.al.* [18]. This model is based upon a single dominant flaw in the material and assumes that a hemispherical corrosion pit transitions to a surface crack, and later transitions to a through-thickness crack. The model was evaluated in terms of statistical data from a

preliminary teardown inspection performed on a lower wingskin (constructed from 2024-T3 aluminum alloy) of a B707 aircraft. The aircraft was approximately 24 years old and had acquired 57,382 flight hours and 22,533 flight cycles during its time in service [19]. The revised model includes the stress concentration effect of a fastener hole and accounts for through-thickness crack growth [1].

2.3.1 Pitting Corrosion Model

Corrosion pits initially predominate in the damage evolution process and they are assumed to be hemispherical in shape and grow at a constant volumetric rate. The expression for a pit depth a up to the transition size a_{tr} at which a crack initiates is modeled by the following equation [18].

$$a = \left[\left(\frac{3MI_P}{2\pi nF\rho} \right) t + a_o^{\,3} \right]^{\frac{1}{3}} \qquad a \le a_{tr} \qquad (2.9)$$

where:

$$I_P = I_{P_o} \exp\left(\frac{-\Delta H}{RT} \right) \qquad (2.10)$$

M = molecular weight (27)
n = valence (3)
F = Faraday's constant (96,514 C/mol)
ρ = density (2,700 kg/m^3)
I_{P_o} = pitting current (random variable)
ΔH = activation enthalpy (40 kJ/mol)
R = universal gas constant (8.314 J/mol-K)
T = 293 K (average absolute temperature while the aircraft is on the ground)
t = time required for a pit to develop to a depth of a
a_o = initial pit radius (random variable)

2.3.2 Corrosion Fatigue Model

The mechanistically based probability model for corrosion fatigue is not available. As such, it is assumed to be the standard power law similar to Equation 2.3.

$$\frac{da}{dN} = C_c \Delta K^{n_c} \tag{2.11}$$

The crack growth exponent n_c represents the functional dependence of the crack growth rate on the driving force ΔK, and it is taken to be deterministic. The coefficient C_c is assumed to be a random variable (rv) that characterizes the variability in material, microstructural, and environmental properties. The number of cycles in this model is expressed in terms of time by $N = ft$, where the frequency $f = 4$ cycles per day, which represents an aircraft used for intermediate flight lengths [18].

The crack driving force ΔK for a semi-circular crack in a circular fastener hole must be modified for a surface crack or a through-thickness crack. For a surface crack, the expression for ΔK is given below.

$$\Delta K_{sc} = \frac{2.2}{\sqrt{\pi}} k_t \Delta\sigma \sqrt{a} \tag{2.12}$$

For an open circular hole, the stress concentration factor k_t is 2.8. When the crack is a through-thickness crack, ΔK is assumed to be equal to the following equation.

$$\Delta K_{tc} = F_{tc}\left(\frac{a}{r_o}\right)\Delta\sigma\sqrt{\pi a} \tag{2.13}$$

F_{tc} is a correction factor for an infinite plate under uniaxial tension containing a circular hole with a single through crack emanating from the hole perpendicular to the loading

axis. It is a function of the crack length a and the radius of the circular hole r_o which is taken to be 3mm. Numerical values for F_{tc} can be fit empirically, to within graphical resolution, by the expression below.

$$F_{tc}\left(\frac{a}{r_o}\right)=\frac{0.865}{\left(\frac{a}{r_o}\right)+0.324}+0.681 \tag{2.14}$$

A transition from pitting corrosion to fatigue crack growth occurs when the criteria in Equations 2.6 and 2.7 are met. The pit size at transition can be found by the experssion below, which is obtained by replacing a by a_{tr} and t by t_{tr} in Equation 2.9.

$$a_{tr}=\left\{\left[\frac{3MI_P}{2\pi nF\rho}\right]t_{tr}+a_o^{\,3}\right\}^{\frac{1}{3}} \tag{2.15}$$

where:

a_{tr} = pit size at transition

t_{tr} = time at transition

A critical pit (a_{th}, t_{th}) where pit size is sufficiently large for FCG to begin is obtained by using the first transition criteria of Equation 2.6, setting $\Delta K = \Delta K_{th}$, and solving Equation 2.1 for a_{th} and Equation 2.15 for t_{th} [1].

$$a_{th}=\pi\left(\frac{\Delta K_{th}}{2.2\Delta\sigma}\right)^2 \tag{2.16}$$

$$t_{th}=\frac{2\pi nF\rho}{3MI_P}\left(a_{th}^{\,3}-a_o^{\,3}\right) \tag{2.17}$$

The crack length during the transition time from a surface crack to a through-thickness crack ($t_{tr} \le t < t_{tc}$) is driven by ΔK_{sc} of Equation 2.12 and may be found from the following relationship.

$$a = \left[a_{tr}^{\ b} - bfC_c \left(\frac{2.2k_t \Delta\sigma}{\sqrt{\pi}} \right)^{n_c} (t - t_{tr}) \right]^{\frac{1}{b}} \tag{2.18}$$

where:

$$b = \frac{2 - n_c}{2} \text{ and } n_c \neq 2$$

When $t \ge t_{tc}$, a is implicitly obtained through the numerical solution of the equation presented below. In this case, the crack driving force is that for a through-thickness crack or ΔK_{tc} [18].

$$t = t_{tc} + \frac{1}{fC_c \left(\Delta\sigma\sqrt{\pi} \right)^{n_c}} \int_{a_{tc}}^{a} \frac{da}{\left[F_{tc}(a/r_o)\sqrt{a} \right]^{n_c}} \tag{2.19}$$

In the models, the rv's ($I_{Po}, a_o, C_c, \Delta K_{th}$) capture the statistical variability and are chosen to be mechanistically and statistically independent of time. Scatter in material properties, environmental sensitivity, and resistance to FCG is reflected in C_c. Material and manufacturing quality are represented by a_o and ΔK_{th}. Scatter associated with the electrochemical reaction for pit growth is depicted by I_{Po}. The three-parameter Weibull cumulative distribution function (CDF) given below is used to adequately characterize each rv [18].

$$F(x) = 1 - \exp\left\{ -\left[\frac{(x - \gamma)}{\beta} \right]^{\alpha} \right\}, \quad x \ge \gamma \tag{2.20}$$

The shape parameter is given by α, the characteristic of the distribution close to the mean value is represented by β, and γ is the minimum value.

2.4 Preliminary Inspection of B707 Wingskin Fastener Holes

The wing panel inspections were a part of the United States Air Force J-STARS program to convert retired B707 aircraft for this service. The B707-123 aircraft (designated CZ-180) was in commercial service for about 30 years and had accumulated 78,416 flight hours and 36,359 flight cycles. This aircraft had the highest time of service of those in the inventory, and many of its wing panels have been distributed to various organizations for further inspection and to train non-destructive evaluation (NDE) personnel [18]. The B707-321B aircraft (designated CZ-184) was in service for 24 years and accumulated 57,382 flight hours and 22,533 flight cycles, thereby having the highest time for the 300 series aircraft in the inventory [19].

It was reported in the J-STARS report that the CZ-184 aircraft showed evidence of greater corrosion damage through visual examination with a 20X magnifying lens of the lower wing panels and associated stiffeners. The B707-321B has larger wings than the B707-123, and for this inspection a larger area of the wing and more holes were examined on the CZ-184. For the inspected sections, a total of 350 and 494 multiple-hole-wall cracks (MHWCs) were reported for the CZ-180 and CZ-184 aircraft wingskins, respectively. In the stiffeners, the total MHWCs reported were 583 and 1,617 for CZ-180 and CZ-184, respectively [18].

The fastener regions of the remaining lower left wing panel sections from the CZ-184 aircraft were salvaged and made available to Lehigh University by the Air Vehicles Directorate of the Air Force Research Laboratory for further investigation and archival purposes. Preliminary examinations by optical microscopy (at 50X to 300X) were carried out with a Hi-Scope™ video imaging system, and focused on fastener holes where damage had been reported by the initial J-STARS teardown and inspection.

Using the Hi-Scope™ system, 110 holes from panel B2-2 along stiffener 4 (S-4) were observed and the findings were compared to those in the initial J-STARS report. Figure 2.6 shows the panel and stiffener that were inspected. The numbered holes in the figure are those in which damage was observed by the J-STARS analysis. Thirty-two additional holes that are circumscribed with a square were found to have damage by using the Hi-Scope™, and these holes were not included in the J-STARS report. Only hole #33 was reported to have damage, but none was observed [18]. Figure 2.7 is a comparison of the probability of occurrence (PoO) for all MHWC lengths reported in J-STARS compared to those measured at Lehigh University with the Hi-Scope™.

Selected fastener holes were sectioned and examined using SEM in an attempt to better understand the processes of damage evolution. Figure 2.8 shows multiple damage as extensive corrosion in the high stress region on the wall of hole #54 in panel B2-2-2. This hole was observed in the as-received condition with general and localized corrosion damage, as well as elongated damage transverse to the direction of the wing bending stresses. The shorter damage appears to be shallow with a rounded bottom, whereas the longer damage may be associated with cracking [18]. From the two-dimensional surface

image, the actual geometry of the damage and presence of fatigue cracking is not known, which necessitates serial sectioning of damage.

Hole #77 in panel B3-2-5 was sectioned to better understand the processes of damage evolution. Figure 2.9 is a 40° tilted SEM image of a larger, elongated type of damage that shows both corrosion and fatigue cracking, or a crack that has been corroded near the surface. Figure 2.10 is a section of a shallow feature, which suggests that these shallow features are small cracks that have been corroded away entirely [20].

In order to evaluate the extent of damage in fastener holes, several highly damaged holes were examined carefully by optical microscopy. Hole #107 and hole #103 of panel B3-2-2 are shown respectively in Figure 2.11 and Figure 2.12 to highlight the magnitude of MWHCs. The longest crack measured was 4.78 mm in a skin section of thickness 9.65 mm, or about 50% of the thickness. For a bore thickness of 6.22 mm, the crack is approximately 75% of this thickness. Furthermore, it can be seen that the dominant crack resulted from the coalescence, or link-up, of several other cracks [18].

These preliminary metallographic findings support the postulated damage evolution process and imply that further metallographic analysis is needed. A detailed analysis of the damage in the holes will provide geometrical information and lend insight into the actual damage process to improve existing models.

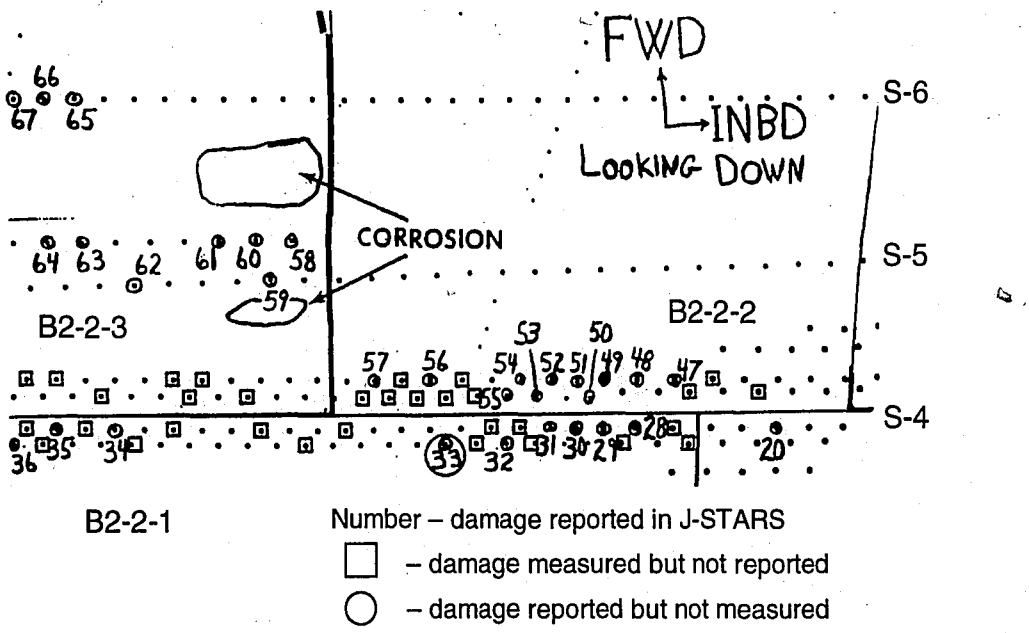

Figure 2.6: A portion of Section 2 along Stiffener 4 from the CZ-184 aircraft for which microscopy and statistical analyses are made [18].

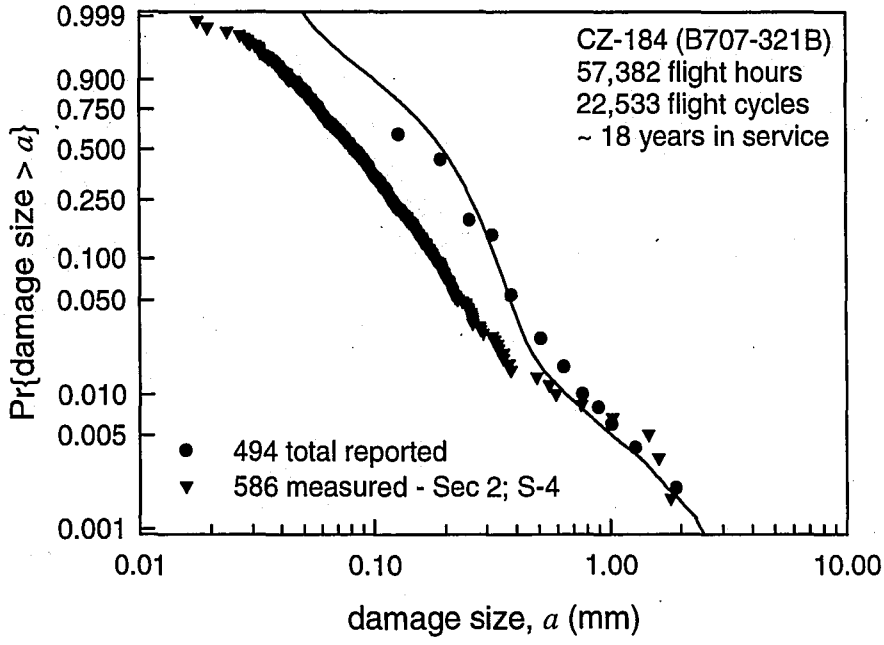

Figure 2.7: Comparison of the PoO for all MHWC lengths reported by J-STARS and all of those measured using video imaging microscopy for 110 holes from Section 2 along Stiffener 4 from the CZ-184 aircraft [18].

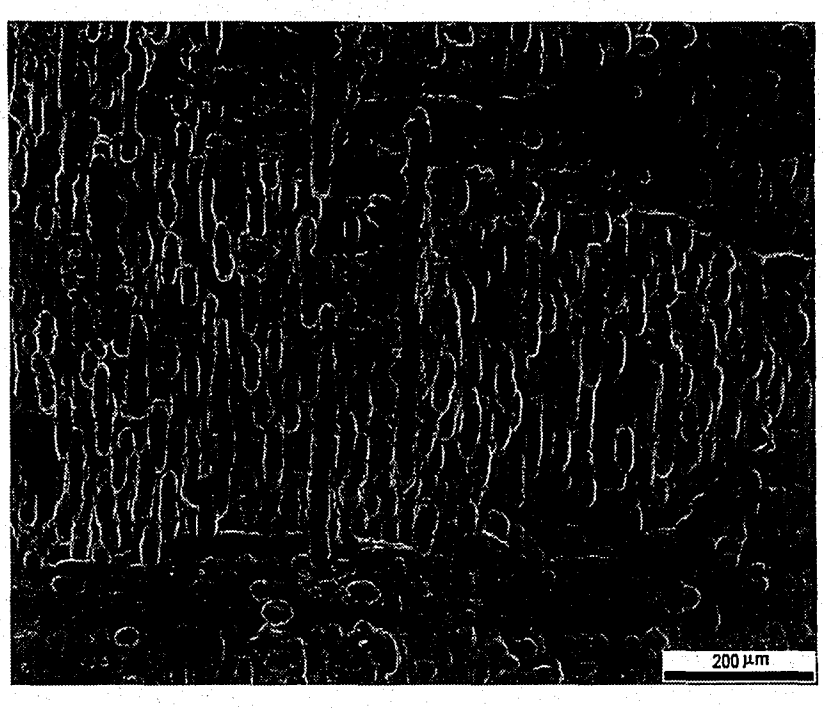

Figure 2.8: SEM micrograph of corrosion-related distributed damage at hole #54 in panel B2-2-2 of the CZ-184 aircraft [18].

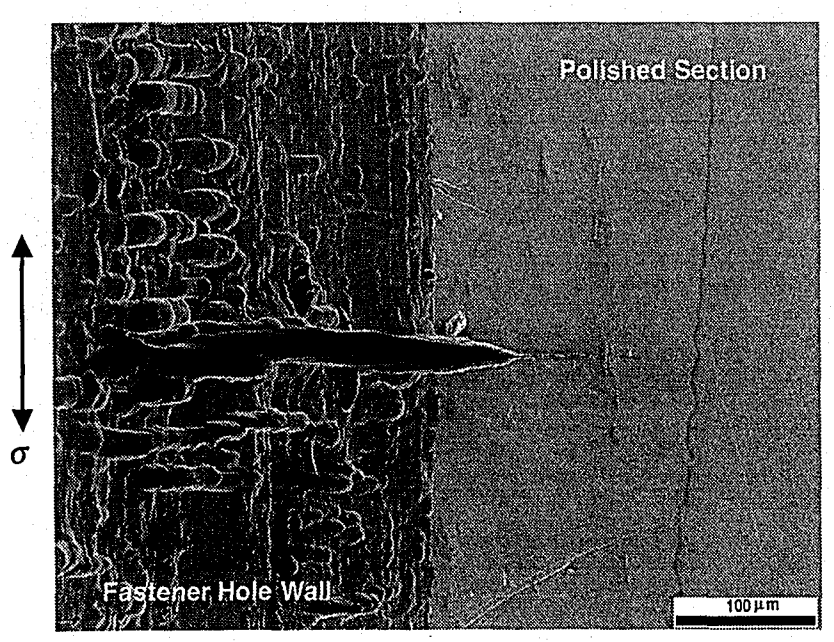

Figure 2.9: SEM micrograph of a section through an elongated damage at hole #77 in wing panel B3-2-5 of the CZ-184 aircraft showing corrosion attack of the fatigue crack [18].

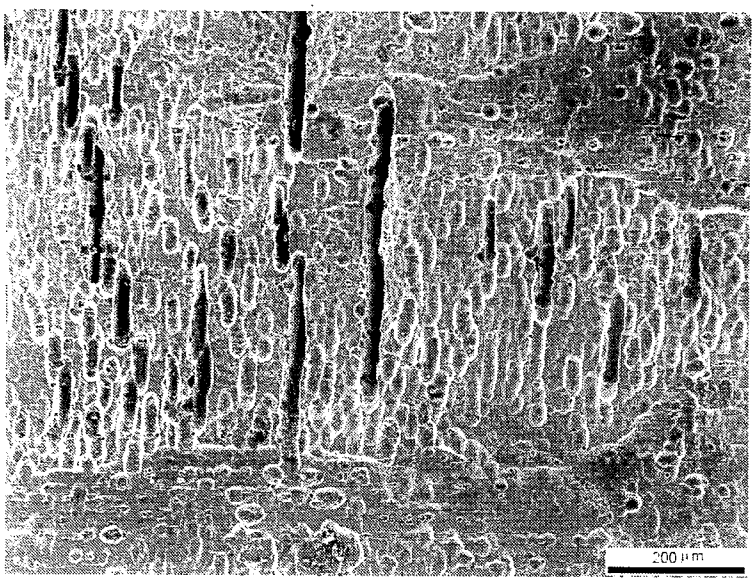

Figure 2.8: SEM micrograph of corrosion-related distributed damage at hole #54 in panel B2-2-2 of the CZ-184 aircraft [18].

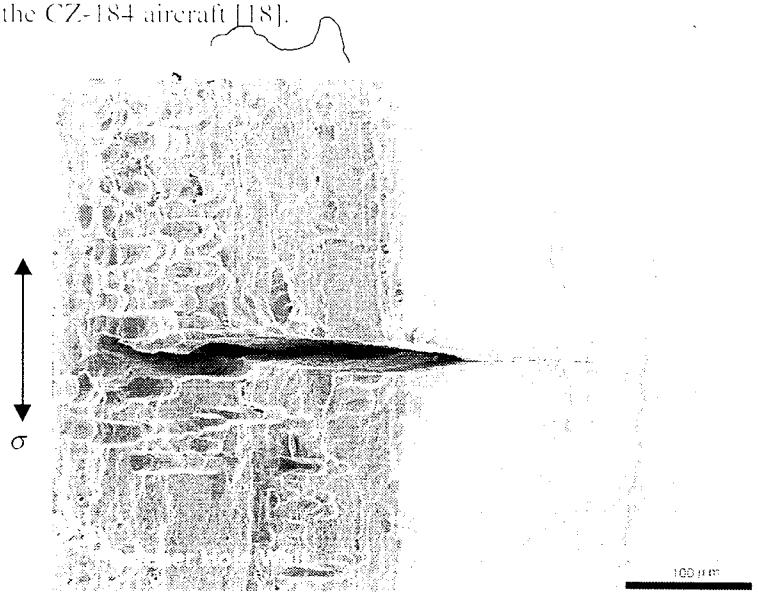

Figure 2.9: SEM micrograph of a section through an elongated damage at hole #77 in wing panel B3-2-5 of the CZ-184 aircraft showing corrosion attack of the fatigue crack [18].

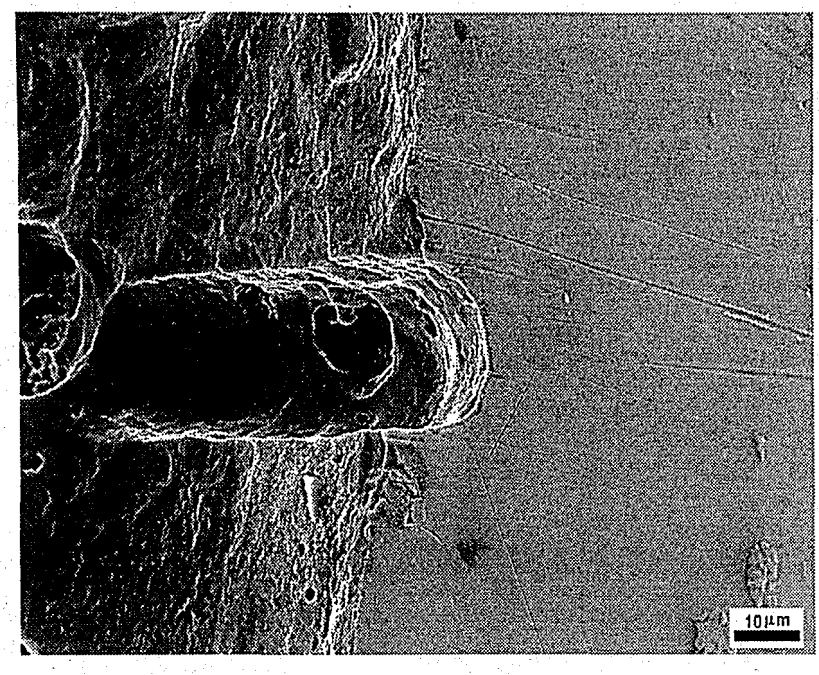

Figure 2.10: SEM micrograph of a through section of a shallow damage at hole #77 in wing panel B3-2-5 of the CZ-184 aircraft suggesting that the crack was dissolved by corrosion [18].

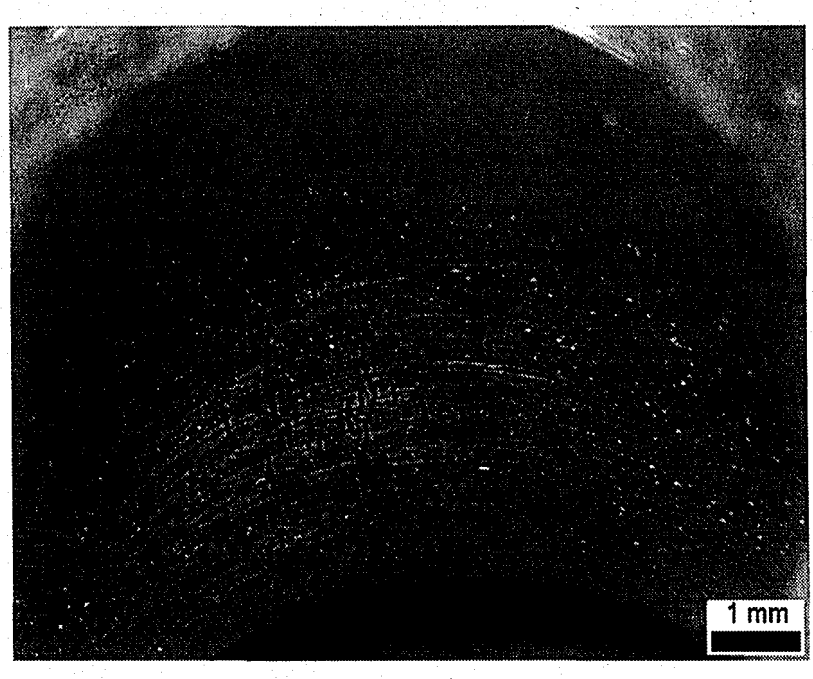

Figure 2.11: Optical micrograph of a highly stressed region of hole #107 in wing panel B3-2-2 of the CZ-184 aircraft showing extensive corrosion fatigue cracking [18].

Figure 2.10: SEM micrograph of a through section of a shallow damage at hole #77 in wing panel B3-2-5 of the CZ-184 aircraft suggesting that the crack was dissolved by corrosion [18].

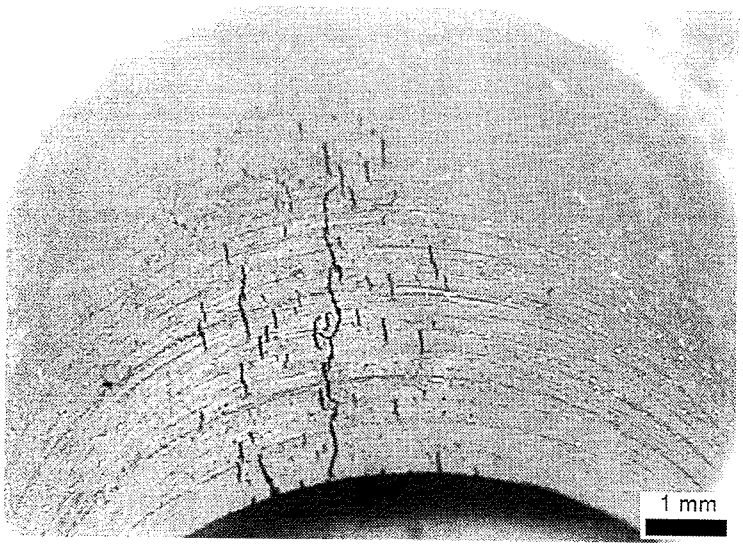

Figure 2.11: Optical micrograph of a highly stressed region of hole #107 in wing panel B3-2-2 of the CZ-184 aircraft showing extensive corrosion fatigue cracking [18].

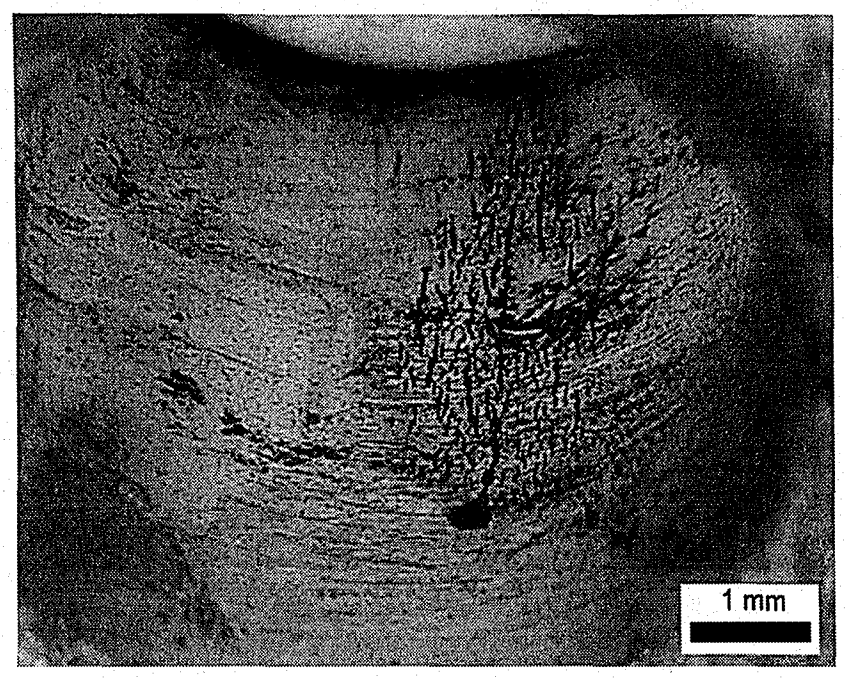

Figure 2.12: Optical micrograph of a highly stressed region of hole #103 in wing panel B3-2-2 of the CZ-184 aircraft showing extensive corrosion fatigue cracking [18].

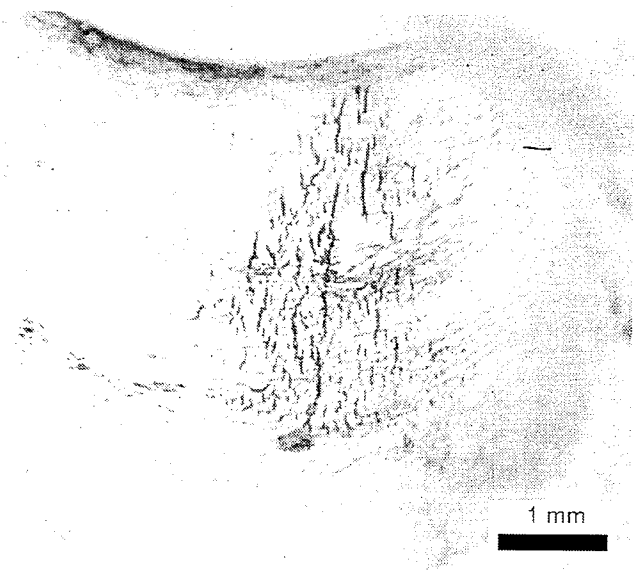

Figure 2.12: Optical micrograph of a highly stressed region of hole #103 in wing panel B3-2-2 of the CZ-184 aircraft showing extensive corrosion fatigue cracking [18].

CHAPTER 3 – EXPERIMENTAL STUDY

3.1 Introduction

Previous investigations carried out on the B707 wingskin demonstrated the need for a more detailed analysis of the fastener holes. Earlier work acknowledged that CF exists in the form of shallow and elongated surface damage, but the actual character of the damage was not determined. Shallow features appeared to be small cracks that had been corroded away, while the elongated damage was associated with fatigue cracking. The model assumed a single dominant flaw in the material, but is this realistic regarding the multiple damage that was observed? Often the dominant flaw was a crack that formed from several other cracks linking together. Without characterizing the actual damage in the fastener holes to determine what exists below the surface, the suitability of the model is in question. As such, further metallographic work in the form of serial sectioning, optical microscopy, and SEM is needed to accurately characterize the damage. The information gathered will provide basis for the development of a model that better represents the damage evolution process.

This chapter provides a detailed description of the experimental techniques used to perform serial sectioning and methods of observation.

3.2 Material

The material used in this research is a 5mm to 12mm thick lower wingskin panel of a B707 aircraft constructed from 2024-T3 aluminum alloy. 2024-T3 is widely used in structural components because of its attractive properties, especially in the clad form

(Alclad 2024-T3). The chemical composition and mechanical properties of this alloy are listed in Table 3.1. The wing panels of the B707 are clad with a thin layer of pure aluminum, but the fastener holes are bare. This increases the susceptibility to corrosion and the formation of multiple crack origin sites in fastener holes when exposed to a deleterious environment.

The wing panels were acid cleaned for a light etch, and a dye penetrant was used to highlight the cracks. These surface preparations were done at the preliminary inspection stage, and when the panels were received by Lehigh University, no further chemical procedures were performed on the material.

Table 3.1: (a) Chemical Composition and (b) Mechanical Properties of 2024-T3 Aluminum Alloy.

(a) Chemical Composition

Weight Percent								
Cu	Mg	Mn	Si	Fe	Zn	Ti	Cr	Al
3.8-4.9	1.2-1.8	0.3-0.9	0.5	0.5	0.25	0.15	0.1	balance

(b) Mechanical Properties[1]

Tensile Strength	483 MPa (70 ksi)
0.2% Offset Yield Strength	345 MPa (50 ksi)
Elongation	17%
Modulus of Elasticity	72.4 GPa (10.5 x 106 ksi)
Poisson's Ratio	0.33

[1] ASM Metals Handbook, Properties of Non-Ferrous Alloys, 1990.

3.3 Experimental Approach

In order to perform a detailed analysis of the damage, a method that allows for sufficient observation of the actual three-dimensional shape of CFC is needed. Three methods were considered for characterizing the damage in selected fastener holes: epoxy replication, non-destructive inspection (NDI), and serial sectioning.

Epoxy replication entails injecting a liquid epoxy into the desired area of interest and allowing it to penetrate into voids in the material, such as corrosion pits and fatigue cracks. After the epoxy hardens, the surrounding material is then chemically removed, leaving behind an epoxy replica that will show the depth and features of the damage [4]. For this research, epoxy replication was not used for two reasons. One, complete destruction of the material is not desirable because further investigations cannot be made on that specimen if needed. The second reason is that the epoxy may not fully penetrate into the damaged area. Deep cracks may be very fine, especially near the crack tip, and if the epoxy does not penetrate completely into these cracks, the model will not truly reflect the three-dimensional shape of CFC.

NDI techniques were employed on a fastener hole with the help of Jerrold Green and Richard Brazill at ALCOA, in Alcoa Center, Pennsylvania, USA. The specimen was placed in a medium of water, and ultrasonic waves traveled through the water to the fastener hole, perpendicular to the direction of cracking. At a discontinuity in the material, such as a crack, the waves bounce off the discontinuity, thereby measuring its depth. For the fastener holes, NDI acknowledged that damage was present, but resolution of the actual damage was inadequate. Since many fastener holes have multiple damage

sites, any smaller "hidden" cracks that are behind the first crack that NDI detects will not appear on the NDI output. In addition, the sample needed to be cut, placed in an acrylic mount, and polished so that the cracks to be inspected were at least 0.05" and no farther than 0.075" from the edge of the sample. The orientation used during NDI is shown in Figure 3.1. NDI showed that damage existed in the fastener holes, but it was ineffective at accurately characterizing the underlying shape for multiple damage sites.

Serial sectioning was the third method considered and this proved to be the most effective way to look at the three-dimensional shape and character of CF damage for this work, as seen from an earlier section in Figure 2.9 and Figure 2.10. It entails removing material at several sections along the length of a crack so that the depth can be measured to create a profile of the crack. Serial sectioning allows for measurements to be made of multiple cracks that link-up, which will assist in determining whether a linked-up crack can be accurately modeled as a single dominant flaw in the mechanistically based probability model.

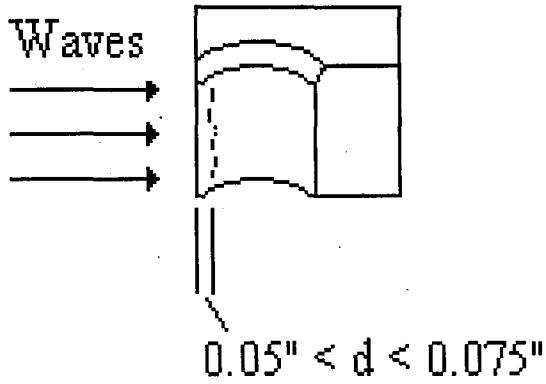

Figure 3.1: The correct fastener hole orientation used during NDI showing that the waves travel perpendicular to the cracks.

3.3.1 Serial Sectioning

Serial sectioning is the process used to remove material at several points along the length of a crack so that its depth can be observed. By obtaining several depth measurements along the length of a crack, its profile can be generated to illustrate its actual shape. A selected fastener hole was cut in half, and only one half was considered during the serial sectioning.

It was necessary to first devise a fixture for the fastener hole that could be used repeatedly and often in a time efficient manner. A common mounting approach of epoxy or bakelite would have been inefficient for this serial sectioning. For example, to obtain five measurements along the length of a crack, the mount would have to be poured and allowed 8-24 hours to set before it could be ground and polished. Then the sample would have to be broken out of the mount for SEM observations. This would have been necessary for each section, which was too time consuming for the desired frequency of sections. Instead, a clamp fixture was devised that secured the fastener hole sample between two aluminum bar clamps which were held in place by two screws. An illustration of the clamp fixture can be seen in Figure 3.2. The fastener hole and clamp were assembled on a flat surface to ensure that the edge of the fastener hole was flush with the edge of the clamp.

Before grinding, it was necessary to know how far into the crack the sections were. Images taken previously with the Hi-Scope™ were imported into Adobe Photoshop, which was used to measure the lengths of cracks to be sectioned. A traveling microscope was used to measure the diameter of the fastener hole (0.25"), and the same

measurement was performed on the Photoshop image, thus serving as a calibration factor for future Photoshop measurements. Crack lengths were then measured, and the distances into the crack needed to obtain 4-5 section measurements were calculated.

Once the specimen was secured in the clamp and the sectioning distances known, the entire assembly was ground to the first section along a chosen crack. The fixture was placed on a rotating wheel and silicon carbide (SiC) grinding papers of 120, 240, 320, 400, and 600 grit were used successively to remove the desired amount of material. Calipers were used before, during, and after the grinding process to ensure that the correct amount of material was being removed. For instance, to remove approximately 0.2mm of material, the fixture was ground using 120 grit for approximately 5 sec., 240 grit for about 10 sec., and 320, 400, and 600 grit until a change in the direction of grinding marks could be observed on the fixture (usually less than 5 sec. each). SiC papers of 8μm and 3μm were then used for approximately 5-10 sec. each to remove any scratches which may have occurred on the specimen while grinding. The correct specimen orientation during grinding can be seen in Figure 3.3. These orientations reduce the amount of grinding and corrosion products that could accumulate in the cracks during the process.

After the specimen was ground to a sufficient distance, the entire fixture was flushed with water and swabbed with a cotton ball to assist in removing any grinding debris from the specimen without inducing scratches. It was then submerged in a beaker (250mL capacity) of ethanol and placed in the ultrasonic cleaner for 3-5 minutes. Following the ultrasonic cleansing, the fixture was flushed with ethanol and dried with an

air dryer to minimize contamination. The fixture was then placed on an optical microscope to observe the crack at the section at 50X, 100X, and 200X. The procedures described in this paragraph are carried out after the final grinding step (3μm) and after each polishing stage.

Polishing the fastener hole was carried out manually in three phases. The first polish was with 1μm alumina powder (Al_2O_3), which was scooped onto a glass plate covered with a polishing nap. Water was then added to make a slurry, and the fixture was rotated firmly for 2 minutes, after which it was rinsed, ultrasonically cleansed, and observed under the microscope, as described in the above paragraph. Under the microscope, the grinding marks should become less obvious and white particles ought to be observed, otherwise this step will need to be repeated. The second polish used a 0.3μm alumina suspension applied to a wheel and rotated manually for 2 minutes. Since the 0.3μm alumina particles are small in size, it is necessary to rinse the fixture well with water and a cotton ball before proceeding to the ultrasonic cleansing. In some cases, it was necessary to repeat this step if when observed under the microscope, there appeared to be no changes from the 1μm polishing step. The final polish used Masterprep on a nap cloth for 1 minute. Initially, silica oxide was used for the final polish, but it tended to dry quickly as a glass-like film on the fastener hole surface and overcharged when placed in the SEM. Similarly, Masterprep must also be washed quickly from the specimen (the fastener hole bore surface especially) in order to prevent a buildup on the surface.

The process of grinding and polishing was repeated for every section along the crack.

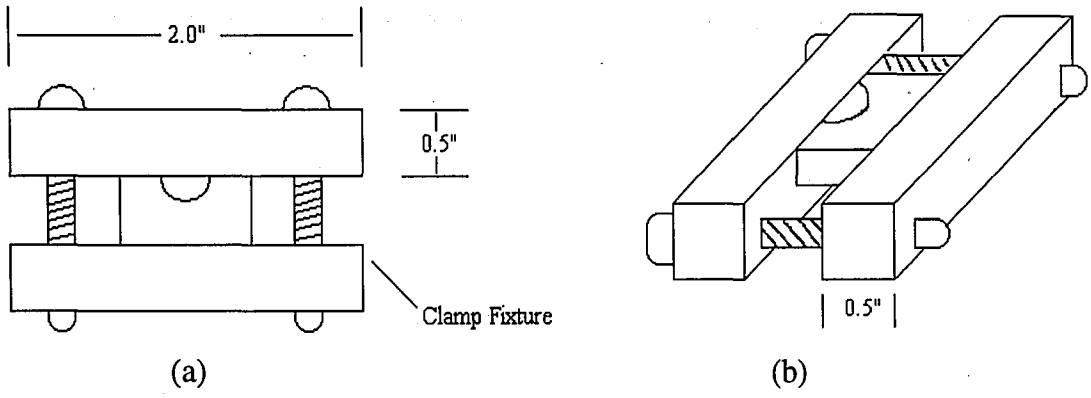

Figure 3.2: Schematic diagram of the clamp fixture used for serial sectioning.

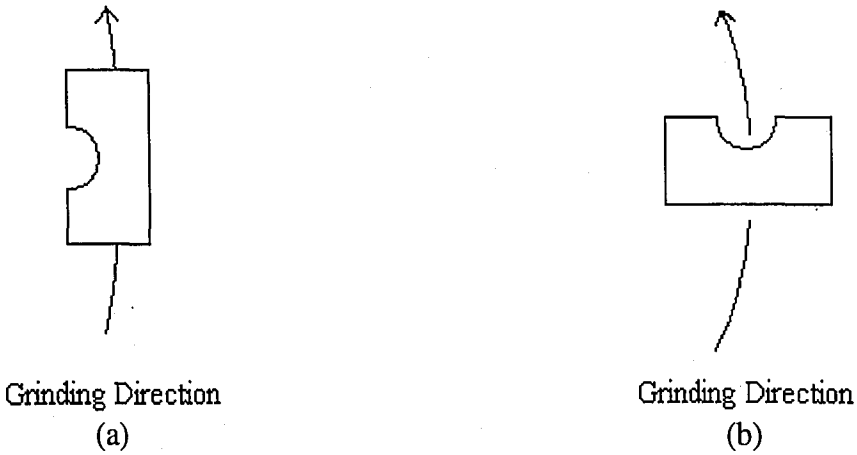

Figure 3.3: Schematic diagram of the correct specimen orientation during grinding for (a) 120, 320, 600, and 3μm grit, (b) 240, 400, and 8μm grit.

3.3.2 Optical Microscopy

Optical microscopes were used at three stages of the serial sectioning process. As mentioned above, an optical microscope was used at the end of grinding and during polishing to monitor the quality of the polish and observe the crack at the section. An Olympus Vanox microscope was used after the final polish to obtain an optical photo of the sectioned crack at 200X. The optical photos were not as high in quality as the SEM photos that are taken later. In addition, the fastener hole needed to remain in the fixture, so three-dimensional or angled photos could not be taken optically. A Nikon microscope with a digitizing pad was used to measure the depth of corrosion and cracking at the section so that crack profiles could be created.

3.4 Scanning Electron Microscopy

The JEOL 6300F scanning electron microscope was used to obtain a higher quality image of the crack at a particular section. Micrographs were taken at a working distance of 16mm and at a voltage of 15kV. The SEM has good resolution, which allows for a more detailed observation of the fastener hole surface where the extent of corrosion and CF damage is readily seen. In addition, the specimen can be tilted in the SEM so that a three-dimensional image may be captured. Knowing the crack depth and its shape at several sections along the crack allows the crack to be characterized and its actual shape can be profiled. With the assistance of SEM to observe the actual damage, stronger inferences may be drawn on the processes of damage evolution in the fastener holes.

This information will form the basis for improvements to the existing mechanistically based probability model.

3.4.1 Sample Preparation

After the fastener hole was ground and polished to the desired section, and optical microscopy was used to measure the crack depth and take a photo, the sample is prepared for the SEM. It is important to handle the fastener hole with caution because hand contact may cause contamination, or if the sample is dropped, it will most likely scratch. Both will affect the quality of the SEM micrographs because contamination and deep scratches are visible on the SEM. To reduce any contamination on the sample or corrosion and grinding products that remain in the crack, a two-step procedure is carried out to ready the sample for the SEM.

The clamp fixture is disassembled, and the cut fastener hole is placed with an aluminum SEM stub into a small beaker (100 mL capacity) of acetone. Enough acetone is added to cover the sample and stub, and the beaker is placed in the ultrasonic cleaner for 10-15 minutes. After this time elapsed, the sample and stub were removed from the acetone bath with tongs (to prevent contamination), flushed with acetone, and then placed in a beaker of ethanol to be cleaned for another 10-15 minutes. After some SEM micrographs showed contamination around the crack and corrosion products in the crack, more care was taken in preparing the samples. The fastener hole was swabbed with a cotton ball moistened with ethanol before being placed in the ethanol beaker to further reduce contamination and crack debris. Following the ultrasonic cleaning, the sample and stub were dried with a blow dryer and the cut fastener hole was fixed onto the stub

using carbon tape. Since carbon tape was used as an adhesive, it was not necessary for the sample to be placed in a desiccator or to sit for 24 hours before being observed in the SEM. The two-step procedure was then effective in preparing a good SEM sample.

3.4.2 Observations

Examining the images acquired by the SEM provided information about the crack shape and depth at a particular section. A tilted three-dimensional image showed where the section was located along a crack as well as the crack depth. The SEM was also used to look at the fastener hole surface where multiple shallow and elongated damage features exist. These features are not as noticeable when observed under an optical microscope, and cannot be seen with the naked eye. The observations made wth the SEM allow the crack to be characterized and a crack profile drawn. This provides information about the damage evolution process, and further insight therefore about how to improve the mechanistically based probability model.

CHAPTER 4 – EXPERIMENTAL RESULTS AND DISCUSSION

4.1 Serial Sectioning

Serial sectioning was performed along two fastener holes of 2024-T3 aluminum alloy from a B707-321B aircraft designated as CZ-184 to characterize the CF damage in the holes. The holes were cut in half, and only one half containing damage was analyzed. Hole #32 from panel B3-2-6 and hole #107 from panel B3-2-2 were sectioned because optical microscopy showed that they had extensive damage. The hole surfaces prior to sectioning are seen in Figure 4.1 and Figure 4.2, and the cracks that will be sectioned are also labeled in these figures. Several sections were made along a selected crack, followed by optical microscopy and SEM analysis, which provided information on the crack shape and depth. Serial sectioning and analysis were performed on a single, isolated crack in the fastener holes and also on several (multiple) cracks that linked-up to form one crack. The crack measurements can be seen in Appendix A for the cracks that were sectioned.

It was necessary to determine the actual shape of a single, dominant crack in order to see whether it is semi-circular in shape as modeled, or not. For multiple cracks that link-up to form one crack, the analysis will reveal whether it can be modeled as one crack, or if the character differs to the extent where modeling refinements are necessary. While serial sectioning was moderately time-consuming and required care in executing the procedure, it was the best method for determining crack geometry in order to examine the actual processes of damage evolution and to guide refinement of the mechanistically based probability model.

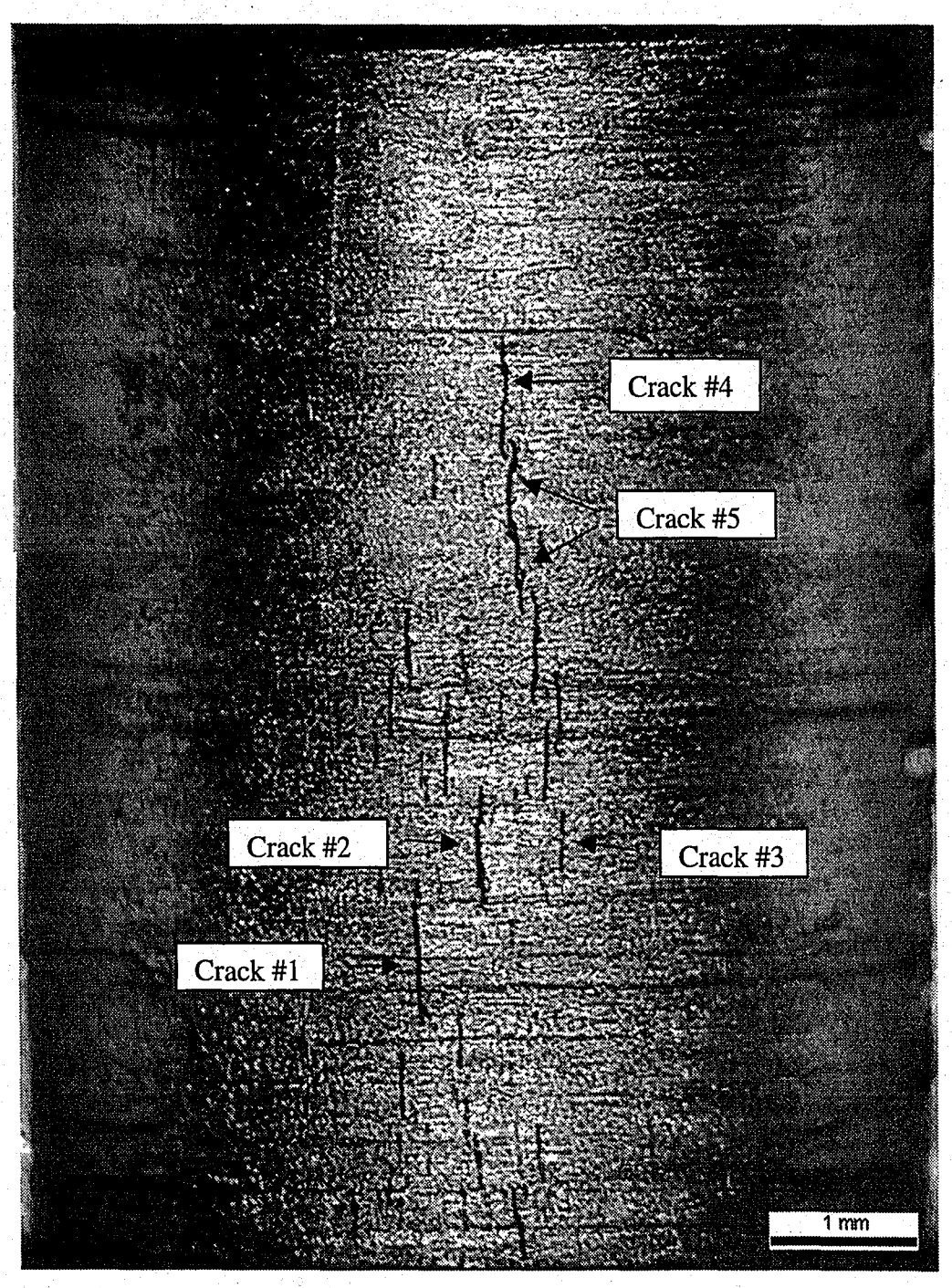

Figure 4.1: 50X Optical micrograph of hole #32 on panel B3-2-6 prior to serial sectioning.

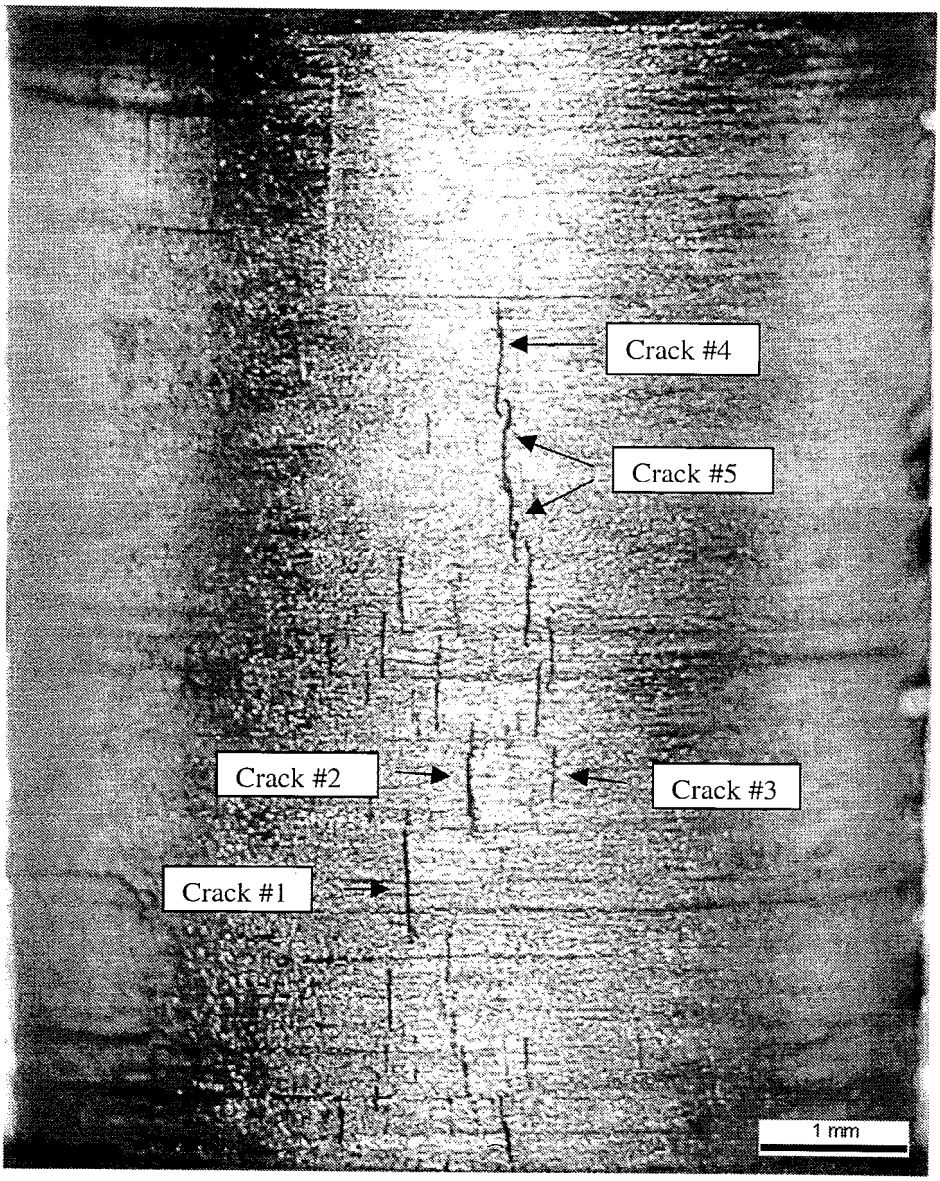

Figure 4.1: 50X Optical micrograph of hole #32 on panel B3-2-6 prior to serial sectioning.

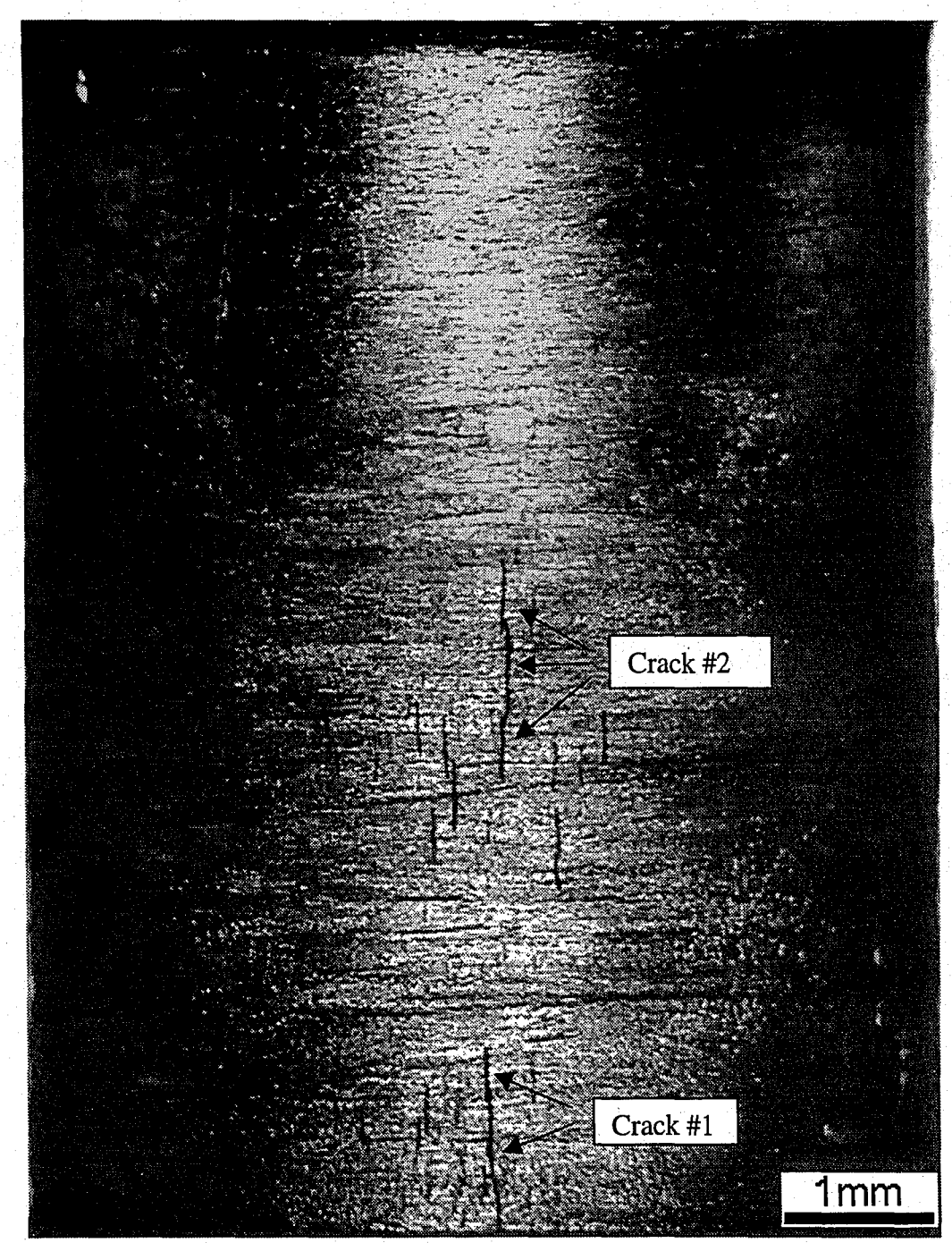

Figure 4.2: 50X Optical micrograph of hole #107 on panel B3-2-2 prior to serial sectioning.

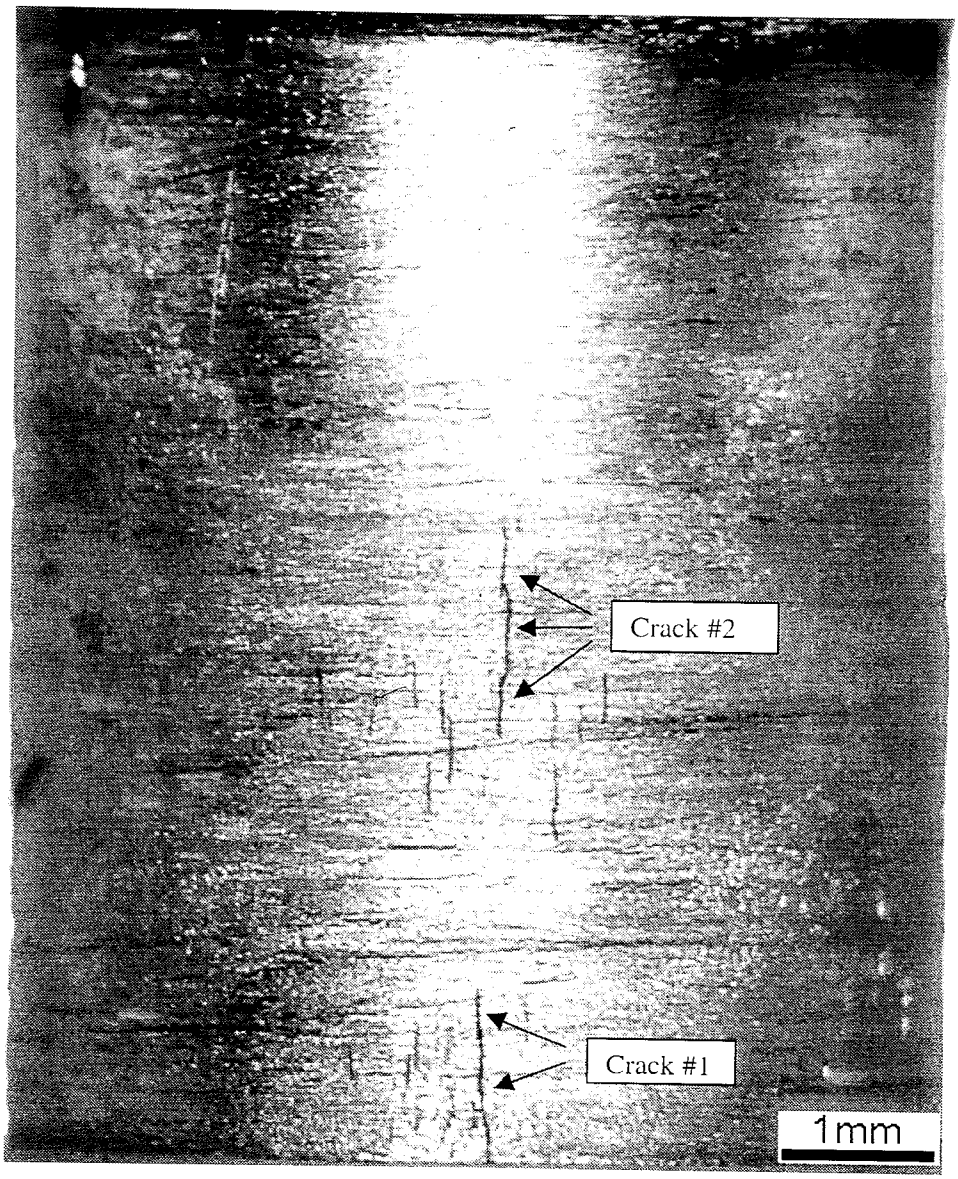

Figure 4.2: 50X Optical micrograph of hole #107 on panel B3-2-2 prior to serial sectioning.

4.2 Crack Characterization

The next sections discuss the results of serial sectioning for a single, isolated crack and multiple cracks that have linked-up to form one crack.

4.2.1 Single Cracks in Hole #32 of Panel B3-2-6

Two cracks on panel B3-2-6 in hole #32 were examined and found to be single, isolated damage sites where the cracks did not link-up. Crack #1 has a length of 0.95mm and a maximum depth of 0.38mm, and the crack measurements are given in Table A.1. From the profile given in Figure 4.3, it can be seen that this crack tends to be semi-elliptical in shape, rather than semi-circular. Crack #3 was the shortest and least deep single crack that was sectioned, and the measurements are seen in Table A.3. It was 0.45mm long with a maximum depth of 0.16mm, as seen from the profile in Figure 4.4. This crack is also semi-elliptical in shape, like the other single crack that was sectioned. These geometrical variations suggest that the mechanistically based probability model for a single dominant crack must be refined to include a semi-elliptical crack geometry. Measurements of crack depth for these two cracks were made using optical microscopy and a digitizing pad. The quality of the optical photos for these cracks was inadequate because scratches easily showed, and therefore they are not presented in this thesis. SEM was not used for the single cracks, but the later use of SEM proved to be useful in photographing interesting features associated with multiple cracks.

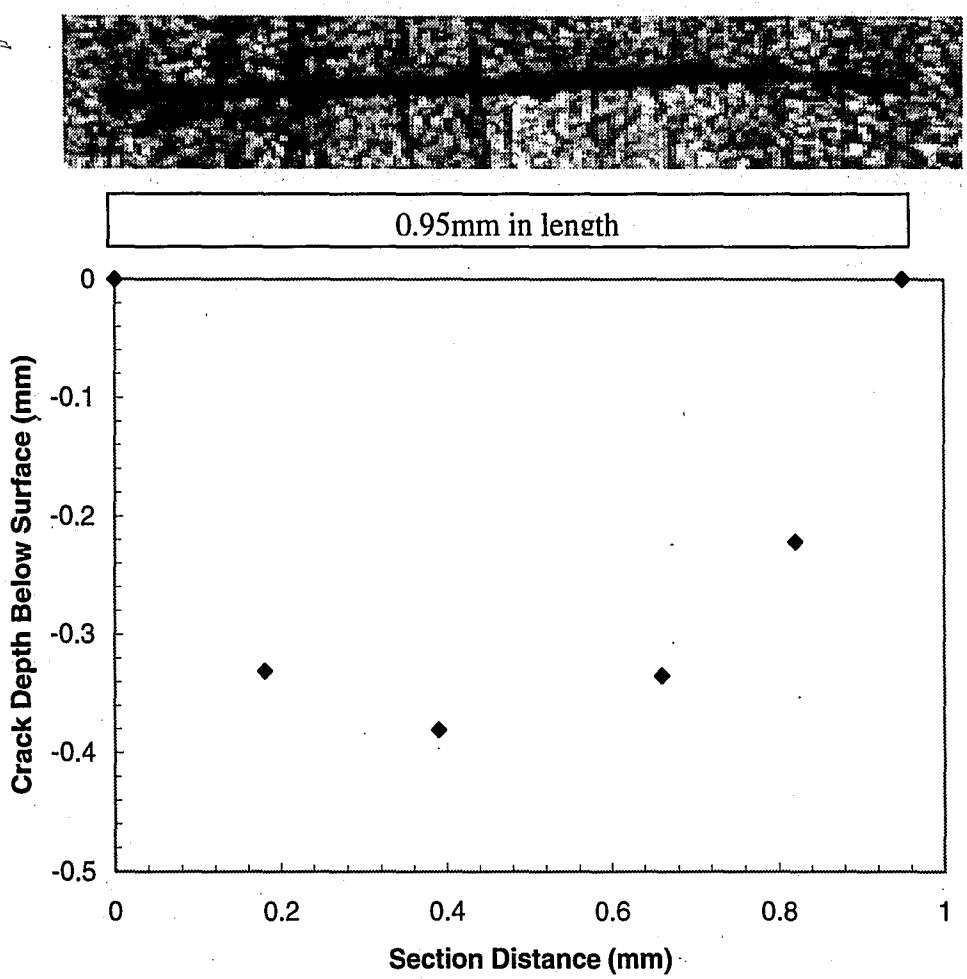

Figure 4.3: Optical micrograph for Crack #1 in hole #32 on panel B3-2-6 and its profile.

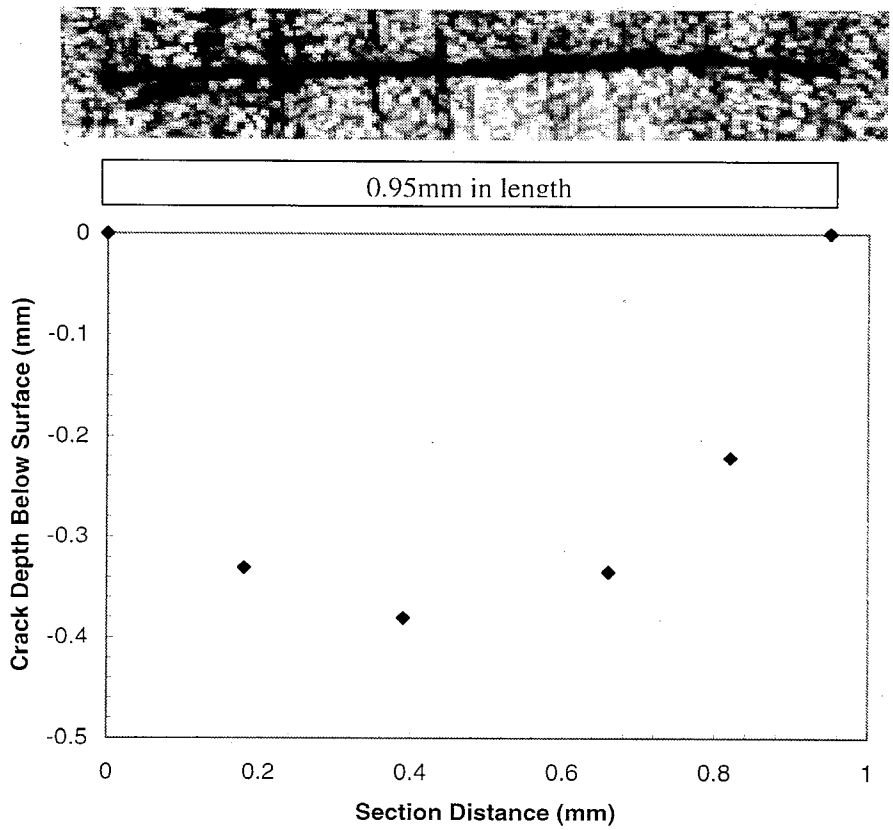

Figure 4.3: Optical micrograph for Crack #1 in hole #32 on panel B3-2-6 and its profile.

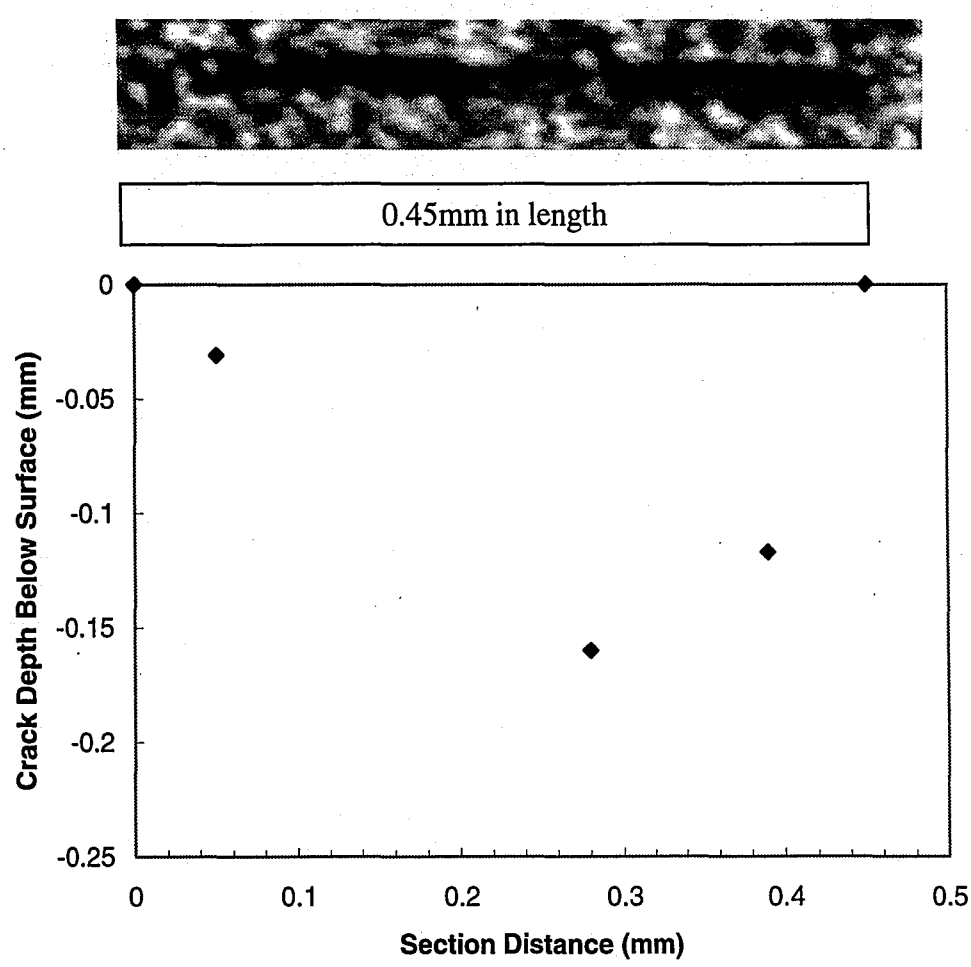

Figure 4.4: Optical micrograph for Crack #3 in hole #32 on panel B3-2-6 and its profile.

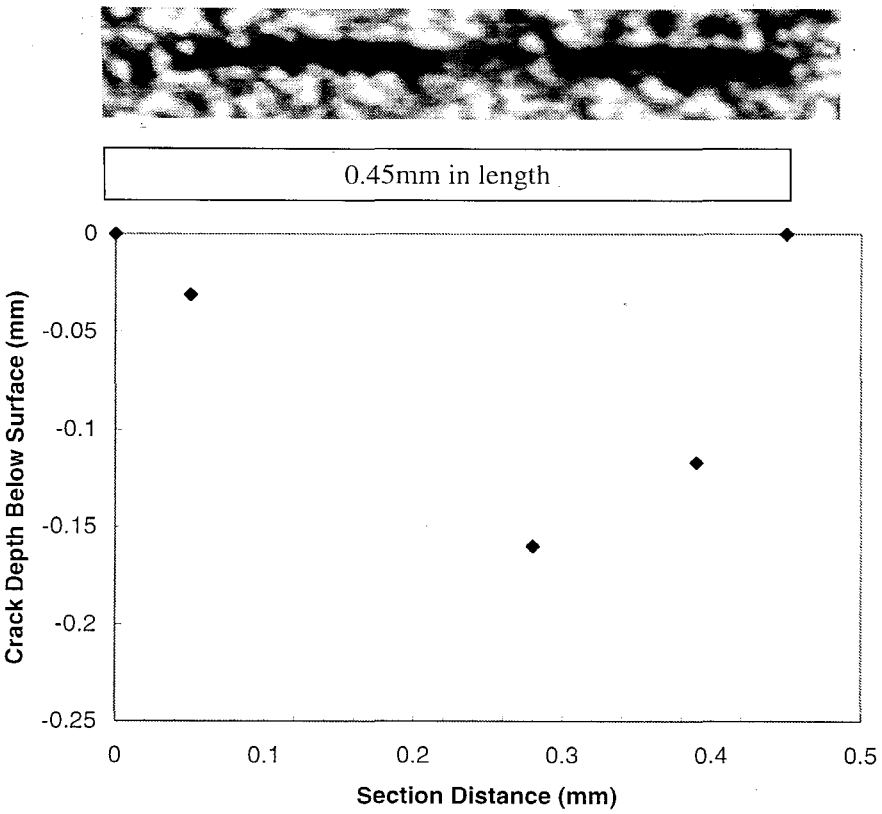

Figure 4.4: Optical micrograph for Crack #3 in hole #32 on panel B3-2-6 and its profile.

4.2.2 Multiple Cracks that Coalesce into One Crack (Link-Up)

Three cracks (#2, #4, and #5) in hole #32 of panel B3-2-6, and two cracks (#1 and #2) in hole #107 of panel B3-2-2 were found to be formed from multiple cracks linking-up to form one crack. The following sections discuss the results of serial sectioning on these multiple cracks.

4.2.2.1 Multiple Cracks in Hole #32 of Panel B3-2-6

On panel B3-2-6, Crack #2 has a length of 0.83mm and a maximum depth of 0.41mm, and is seen in Figure 4.5 with its corresponding profile. The crack measurements are in Table A.2. It appears in this figure that the crack linked up with shallow damage on both the right and left ends, as denoted by different markers on the profile. The metallographic analysis however, did not section through a region where the cracks linked-up to provide information on the individual crack depths during the link-up process. It is evident from the figure though, that link-up does occur and these multiple cracks must be accounted for in the mechanistically based probability model.

Crack #4 in hole #32 on panel B3-2-6 is 0.83mm in length with a maximum section depth of 0.37mm, and the measurements are presented in Table A.4. A distinct region where link-up occurs can be seen in Figure 4.6. It appears that another link-up occurs with shallow damage to the left of the crack. If the crack continued to propagate, eventually it would have linked together with Crack #5. It should be noted that there is error in the construction of a profile for this crack. Serial sectioning for Crack #4 did not begin at a point that included the entire shallow damage link-up region. Instead, sectioning began approximately 0.20mm into the shallow damage, which fails to provide

measurements on the depth of this link-up damage for the profile. Therefore, the actual crack length is about 1.03mm (0.83mm + 0.20mm) and there is error in the profile.

Figure 4.6 and Appendix B contain SEM micrographs that were performed at select sections along Crack #4. At Section 2, the SEM micrograph (Figure 4.6 and Figure B.1(a)) shows that crack branching occurs at an approximate depth of 0.1mm. This branching may be associated with the observed link-up of the shallow damage. Extensive grinding and corrosion product that accumulated in the crack mouth is also seen in the micrograph at this section. This resulted in more careful cleaning procedures to ensure that this product was removed from the crack. At Section 3, the maximum crack depth of 0.37mm occurred. In the SEM micrograph (Figure 4.6 and Figure B.1(b)), a corrosion pit is seen to the left of the crack, as well as unfortunate staining of the sample. This staining also led to the use of thorough SEM specimen preparation techniques so that staining could be avoided in the future.

The first crack that was analyzed to reveal the shape of a crack at the link-up section by obtaining measurements (see Table A.5) through this link-up region was Crack #5 on panel B3-2-6. From Figure 4.7, it can be seen that this crack consists of four cracks that link-up to form the 1.17mm length of Crack #5. The crack profile shows that the multiple cracks that coalesce to form this crack do not form one crack that is purely semi-circular, nor is it semi-elliptical in shape. The two linked-up cracks which are in the center and more elongated, initiated from two separate flaws, and grew independently until they linked-up to form a larger, dominant crack. A larger dominant crack is more of a structural concern than a shallow crack. The other cracks that links-up (farthest to the

left and right in Figure 4.7), are not as deep as the previous two cracks because they formed later than the other cracks, which coalesced sooner to become the dominant part of the crack. The mechanistically based probability model does not account for the initiation and propagation of multiple cracks that eventually link-up and grow as a dominant crack. This information will be used to make such refinements to the model .

SEM photos for Crack #5 were taken for Sections 4-8, and are located in both Figure 4.7 and Appendix C. The figures in Appendix C are enlarged and will therefore be referenced to throughout this section. The micrograph at Section 4 (Figure C.1(a)) show the existing crack from the previous sections on the right, and the link-up crack appears on the left. The SEM micrograph of Section 5 (Figure C.1(b)) shows the new, link-up crack to the left, the old crack of Sections 1-4 is in the middle (with a maximum section depth of 0.42mm here), and a corrosion pit is seen on the right. Section 6 was made where the link-up was almost complete, and the micrograph in Figure C.1(c) shows how the two cracks have nearly linked-up to form a single crack. At Section 7 in Figure C.1(d), the final link-up area can be seen as a new crack forms to the left. The last micrograph was taken at Section 8, as seen in Figure C.1(e) where the remnants of Crack #5 are seen to the right and a new crack (which if analyzed would have been Crack #6) forms to the left.

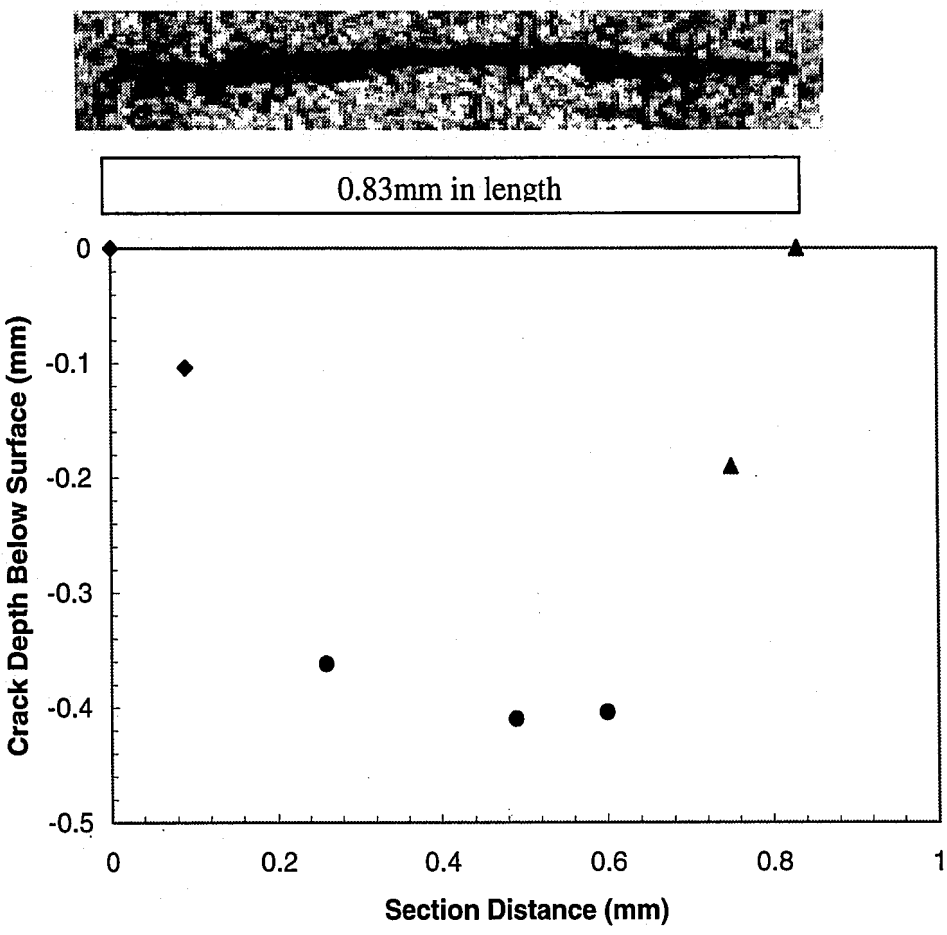

Figure 4.5: Optical micrograph for Crack #2 in hole #32 on panel B3-2-6 and its profile.

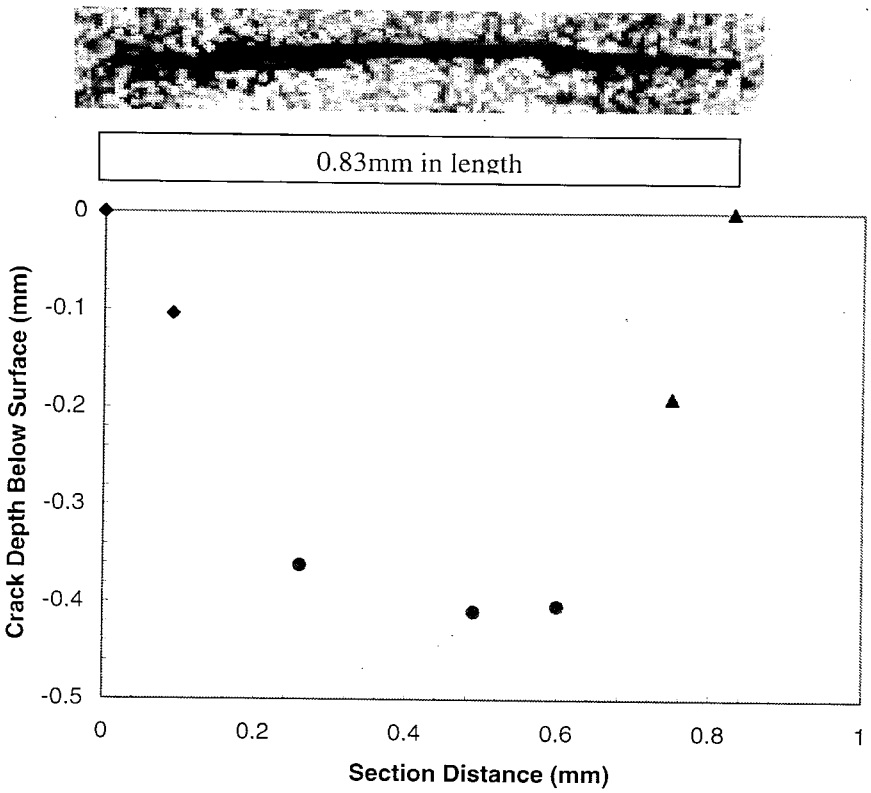

Figure 4.5: Optical micrograph for Crack #2 in hole #32 on panel B3-2-6 and its profile.

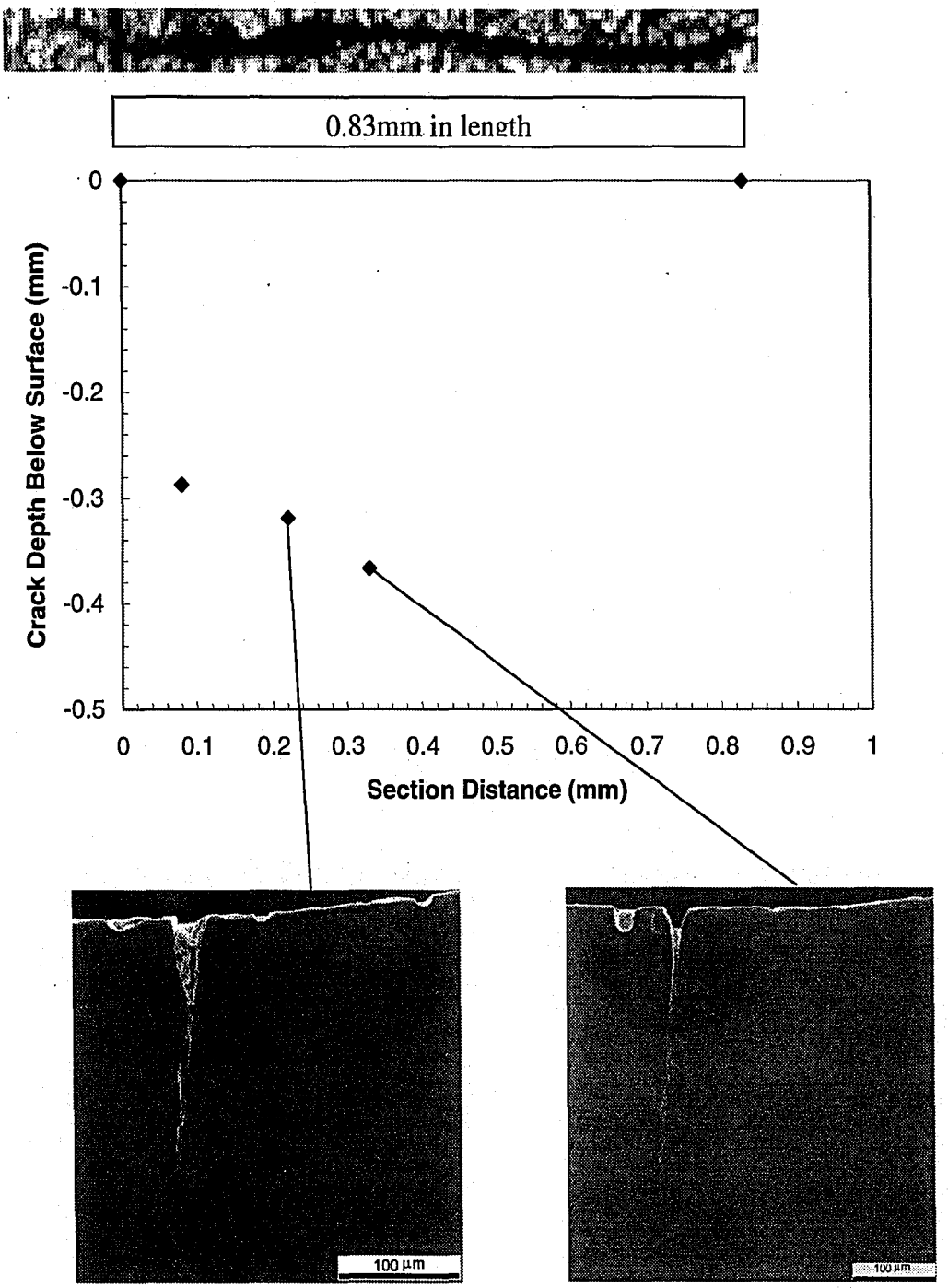

Figure 4.6: Profile with SEM micrographs for Crack #4 on panel B3-2-6.

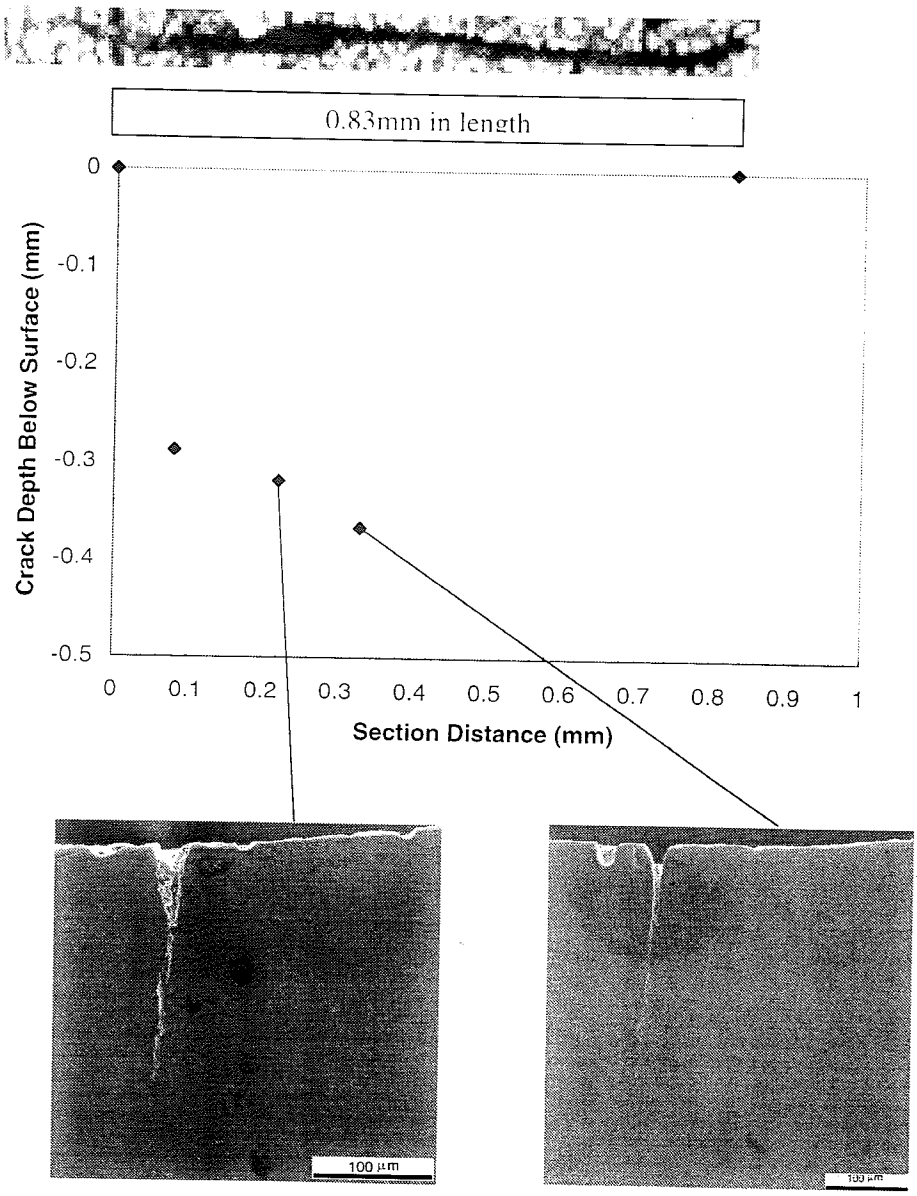

Figure 4.6: Profile with SEM micrographs for Crack #4 on panel B3-2-6.

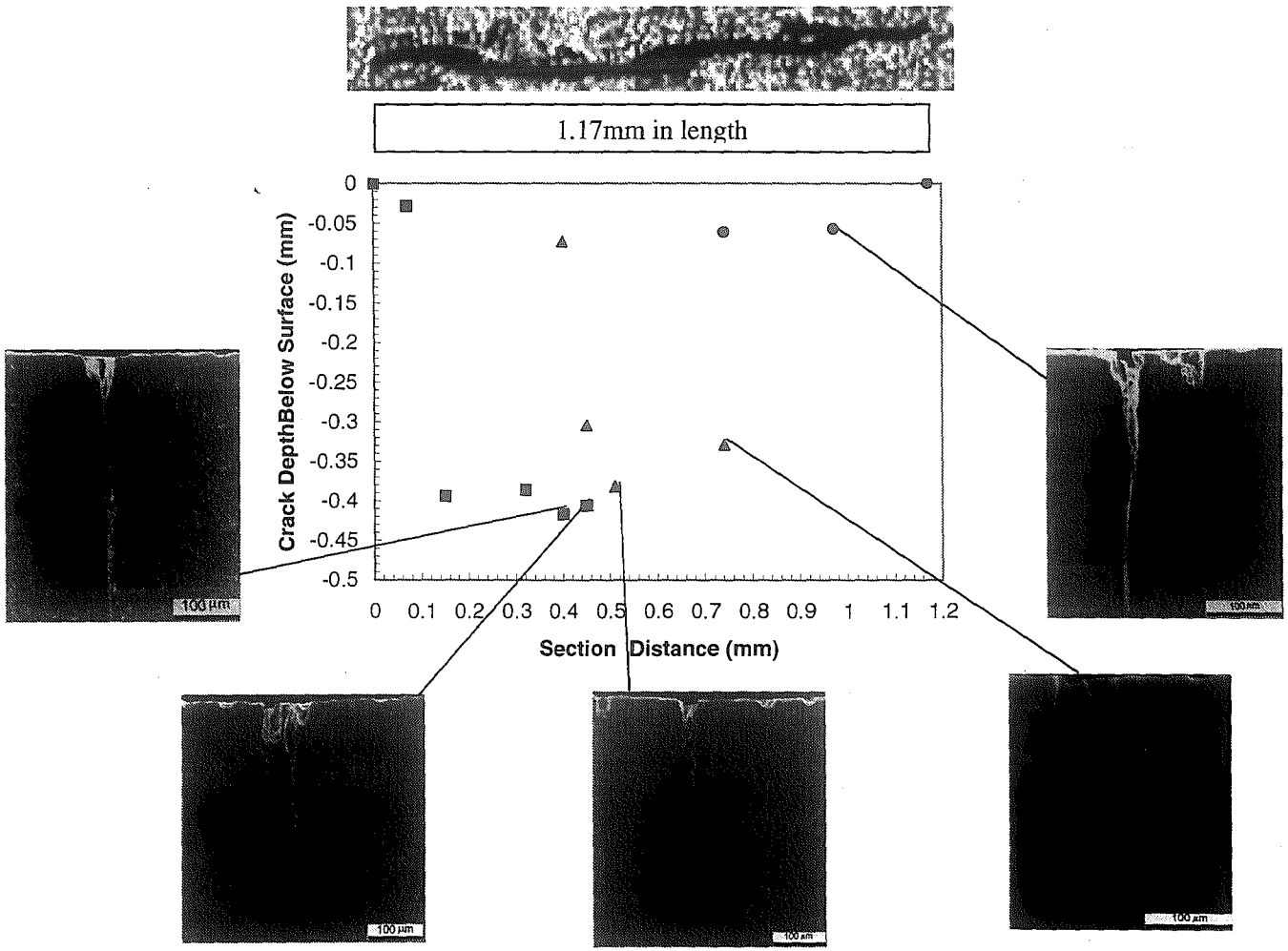

Figure 4.7: Profile with SEM micrographs for Crack #5 on panel B3-2-6.

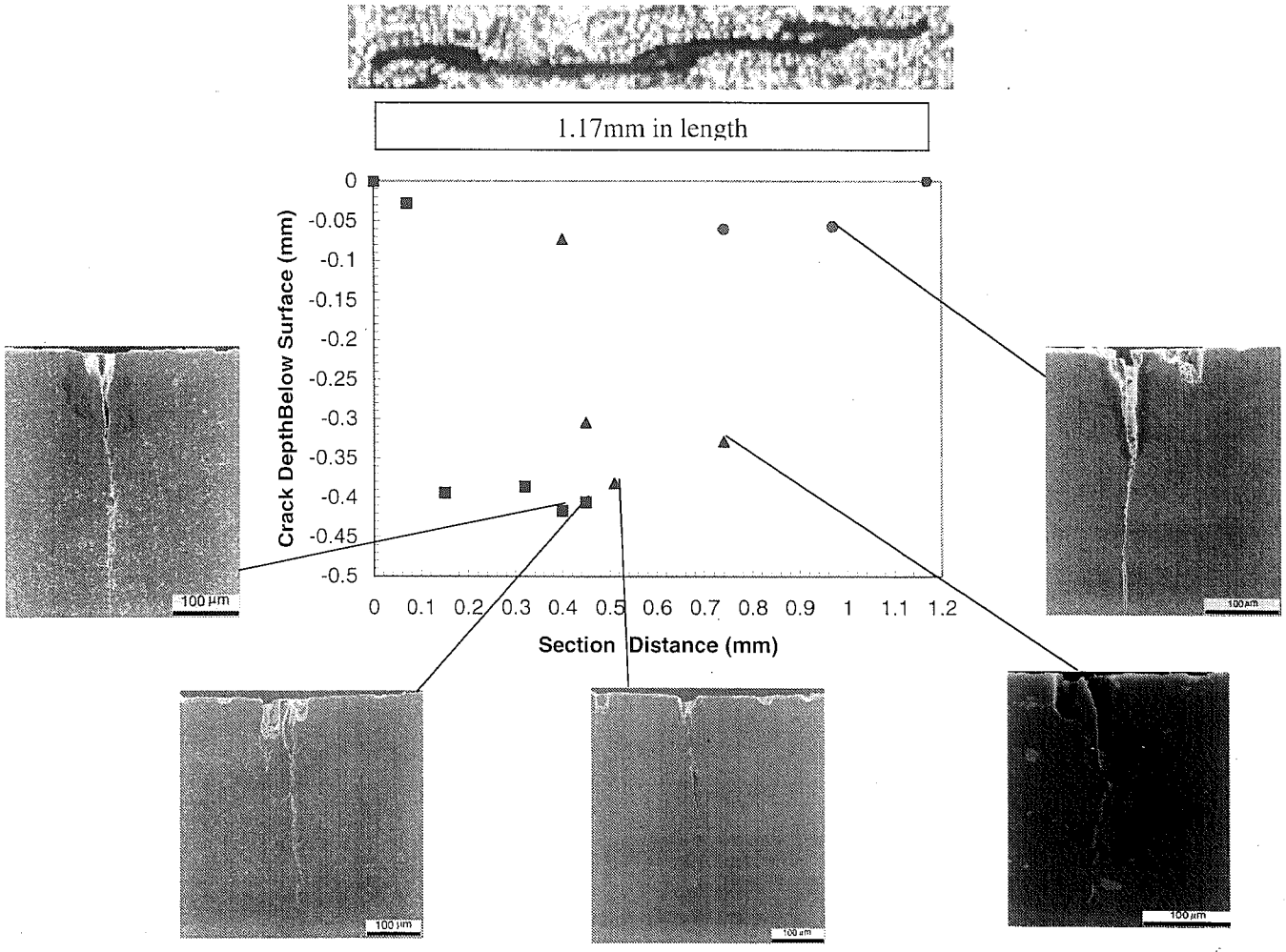

Figure 4.7: Profile with SEM micrographs for Crack #5 on panel B3-2-6.

4.2.2.2 Multiple Cracks in Hole #107 on Panel B3-2-2

In hole #107 on panel B3-2-2, two cracks were analyzed and each was formed from the link-up of multiple cracks. Crack #1 section measurements are presented in Table A.6. The profile for Crack #1 is seen in Figure 4.8, where it can be seen that two cracks, perhaps three have linked-up to form one crack. One link-up area is seen toward the right end of the crack in the figure, while another link-up region occurs approximately 1/3 of the distance into the crack, as will be determined from an SEM micrograph. There are two additional cracks toward the wingskin surface below Crack #1 which may have coalesced with this crack if growth had continued, and can be seen in a micrograph of this region in Figure 4.9. Crack #1 is 0.87mm in length, and the growth trends of the individual cracks are seen. If crack growth continued to occur, eventually a dominant crack would have formed from the link-up and propagated like a single crack. To model Crack #1 as a single, dominant crack that is semi-circular or semi-elliptical in shape however, may not be realistic since it is composed from three link-up cracks. As a result, refinements to the existing mechanistically based probability model should be considered.

SEM micrographs were taken at each section along Crack #1, which appear in Figure 4.8 and Appendix D. Appendix D shows enlarged SEM micrographs, and thus those micrographs will be referenced to during the discussion. The micrograph of the first section is particularly interesting because it shows a possible area of link-up with the crack on the left (Figure D.1(a)) if crack propagation continued. A three-dimensional tilted photo was also taken of this section, which shows the depths of damage at that

section as well as the remaining length of the crack (Figure D.1(b)). The micrograph of Section 2 shows a fine crack near the crack-tip of Crack #1, which is an indication that link-up is about to occur. The tilted, three-dimensional micrograph of this section shows that indeed, a link-up will occur with the crack that is located to the back and right of the present section (Figure D.2(b)). This confirms that Crack #1 on panel B3-2-2 is formed from three coalescing cracks. The maximum section depth was measured at Section 3, and the associated micrographs are seen in Figure D.3. Following the link-up, crack depth measurements continued, and no measurement reached the depth of the pre-linkup crack, as seen in the profile. A second link-up region is nearing, as seen in the micrographs of Section 4 in Figure D.4. Section 5 occurs after the link-up, and micrographs for this section and the remaining three sections are seen in Figures D.4 – D.8.

The final crack sectioned is designated Crack #2 in hole #107 on panel B3-2-2, and is 1.45mm in length with a maximum depth of 0.33mm. The crack measurements are presented in Table A.7. This crack has one distinct, complete link-up toward the left end, and another link-up region toward the right end as seen from the profile in Figure 4.10. The profile shows the growth trend of multiple cracks, and these findings further the need for refinements to the mechanistically based probability model to account for multiple crack growth and link-up.

An SEM micrograph of the sections taken of Crack #2 are shown in Figure 4.10 and Appendix E. Appendix E shows enlarged SEM micrographs, and thus those micrographs will be referenced to in this section. From the first section, five other cracks

in the material aside from Crack #2 were found to exist at this section, as seen in Figure E.1. Section 2 was interesting in that at a depth of approximately 0.13mm, the crack branches, and the left branch grows about 0.15mm deeper than the right branch, as seen in Figure E.2, and this is indicative of an upcoming link-up. Sections 3 and 4 occurred after the distinct link-up, and their micrographs can be seen in Figure E.3 and E.4. Section 5 captures the end of the pre-existing crack on the right (which is deepest at this section at 0.31mm), and the crack to which it is linking appears to the left in Figure E.5. Section 6 shows the post-linkup crack in Figure E.6, as well as a remnant of the old crack to the right, which indicates that a link-up has occurred. The micrographs for Sections 7 and 8 are also shown in this appendix as Figure E.7 and Figure E.8

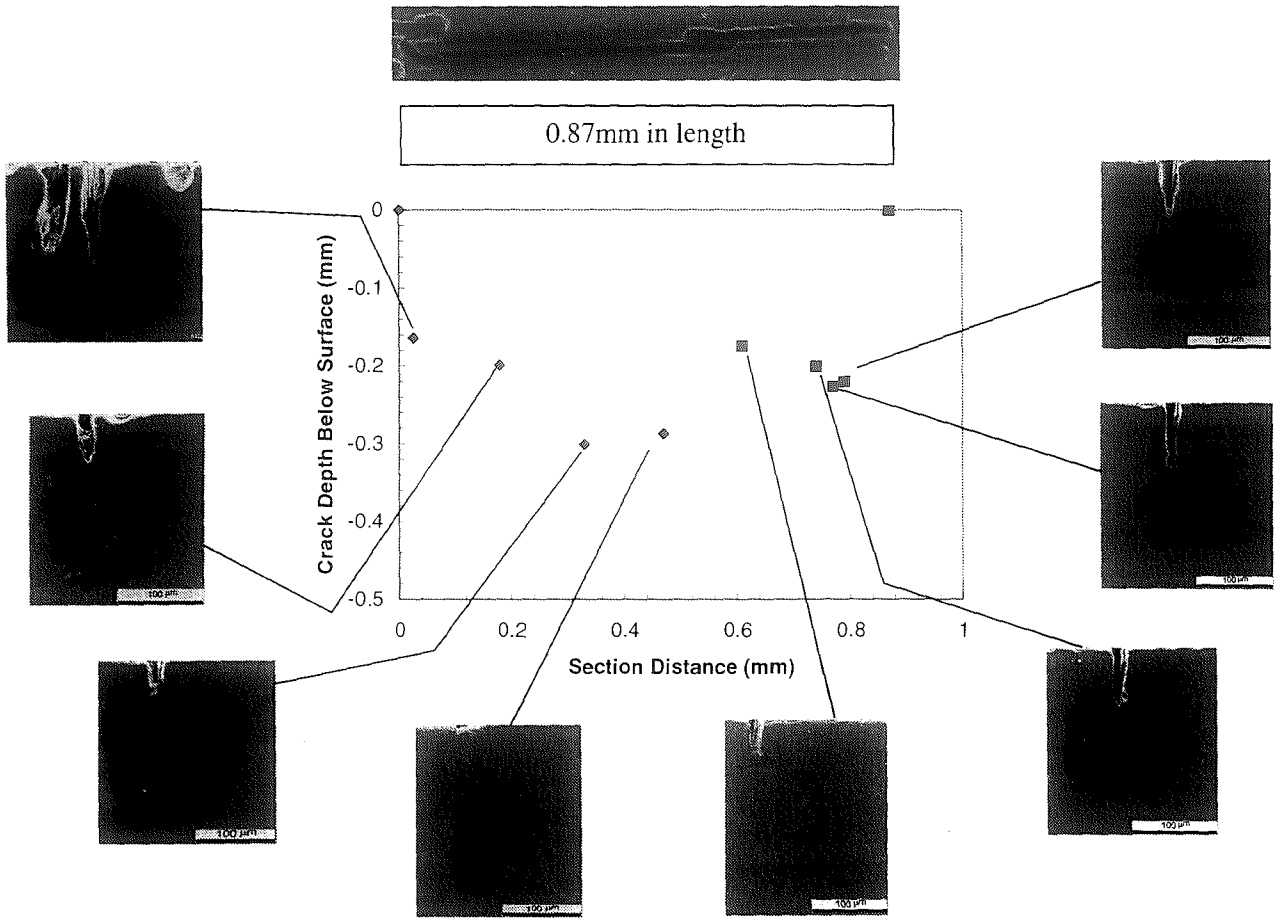

Figure 4.8: Profile with SEM micrographs for Crack #1 in hole #107 on panel B3-2-2.

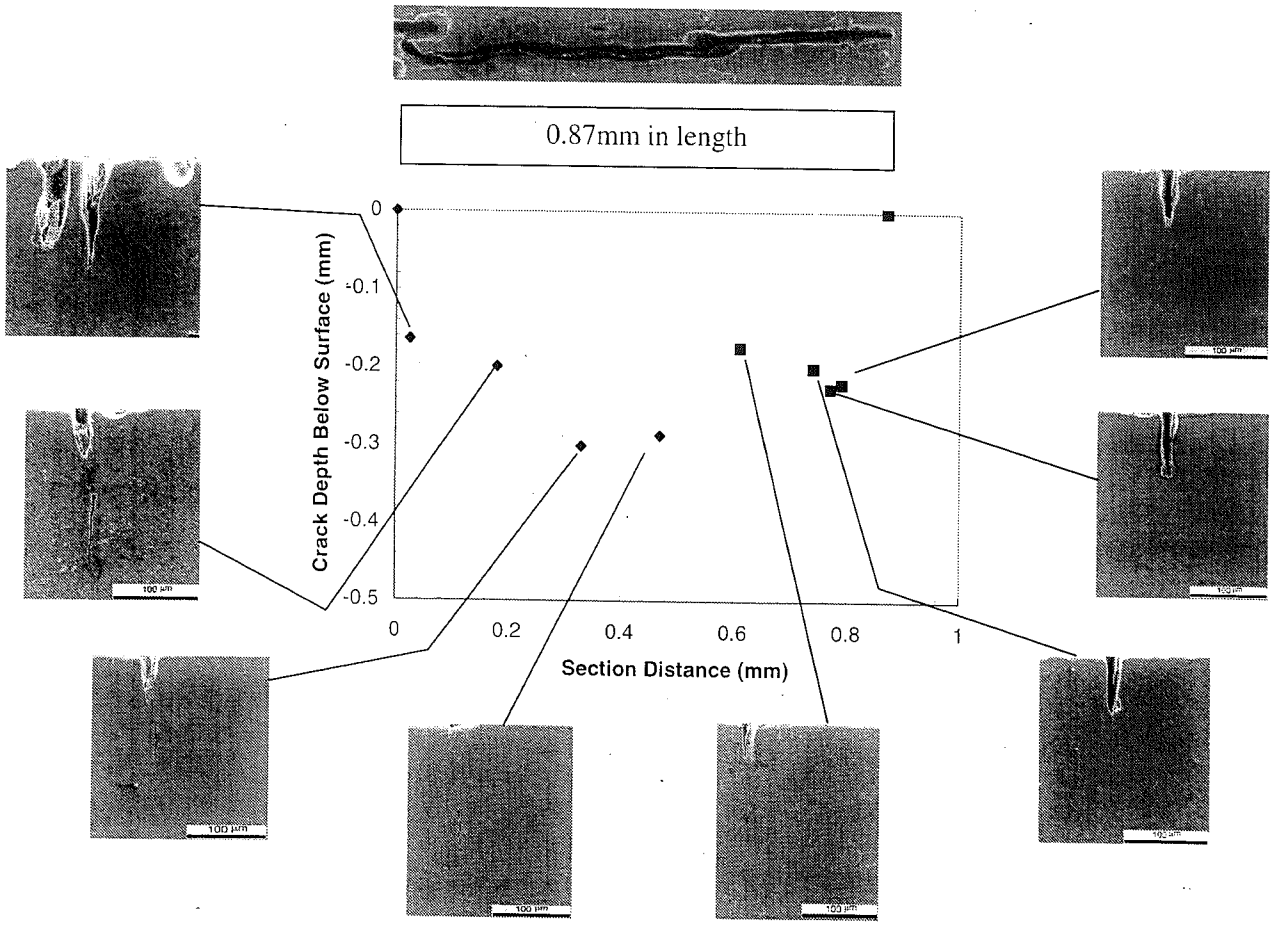

Figure 4.8: Profile with SEM micrographs for Crack #1 in hole #107 on panel B3-2-2.

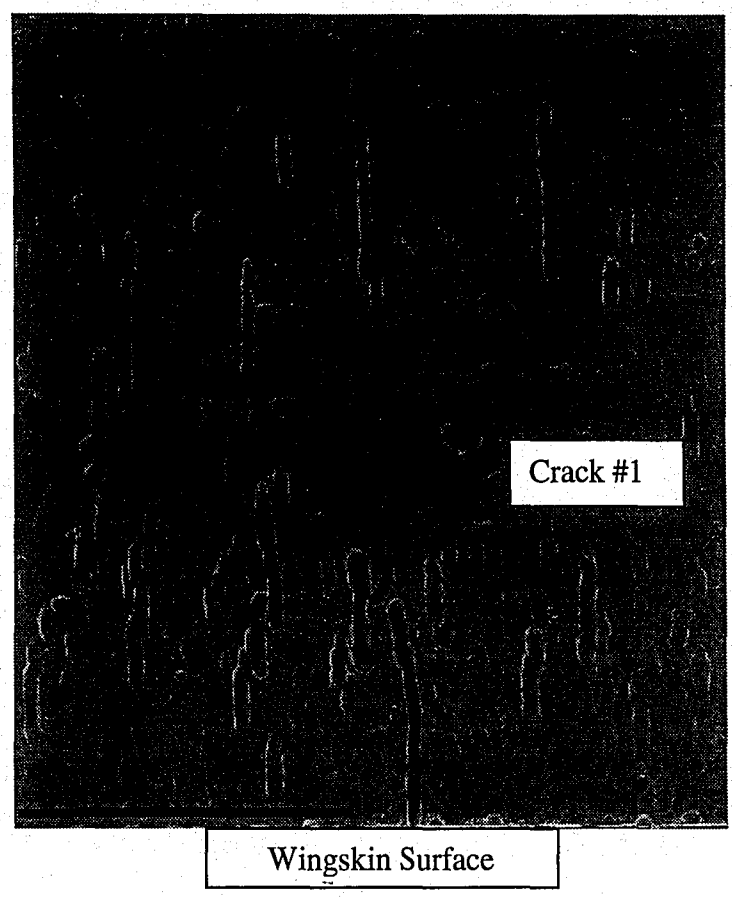

Figure 4.9: 50X SEM micrograph of the lower cracked region of hole #107 on panel B3-2-2. Notice how Crack #1 will link-up with damage near the wingskin surface if the crack continues to grow.

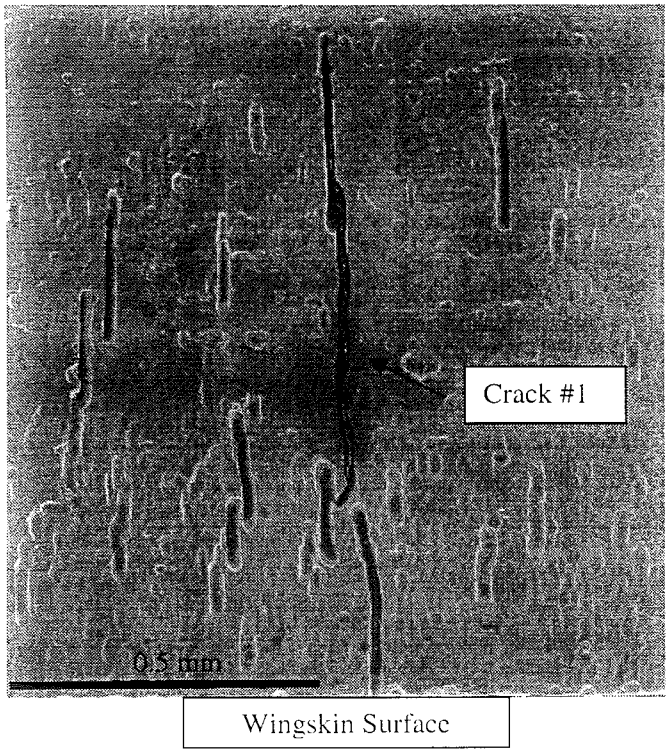

Figure 4.9: 50X SEM micrograph of the lower cracked region of hole #107 on panel B3-2-2. Notice how Crack #1 will link-up with damage near the wingskin surface if the crack continues to grow.

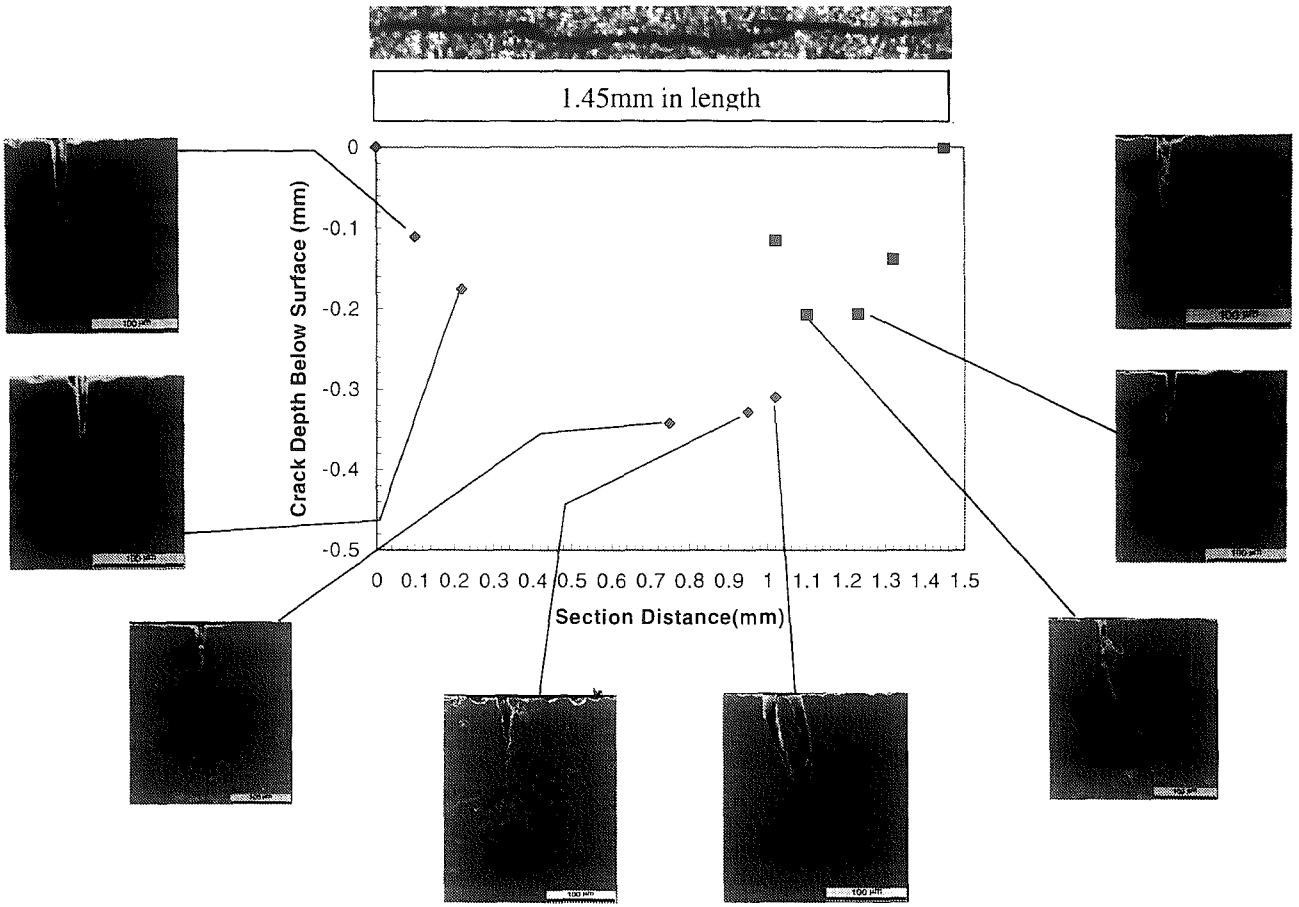

Figure 4.10: Profile with SEM micrographs for Crack #2 on panel B3-2-2.

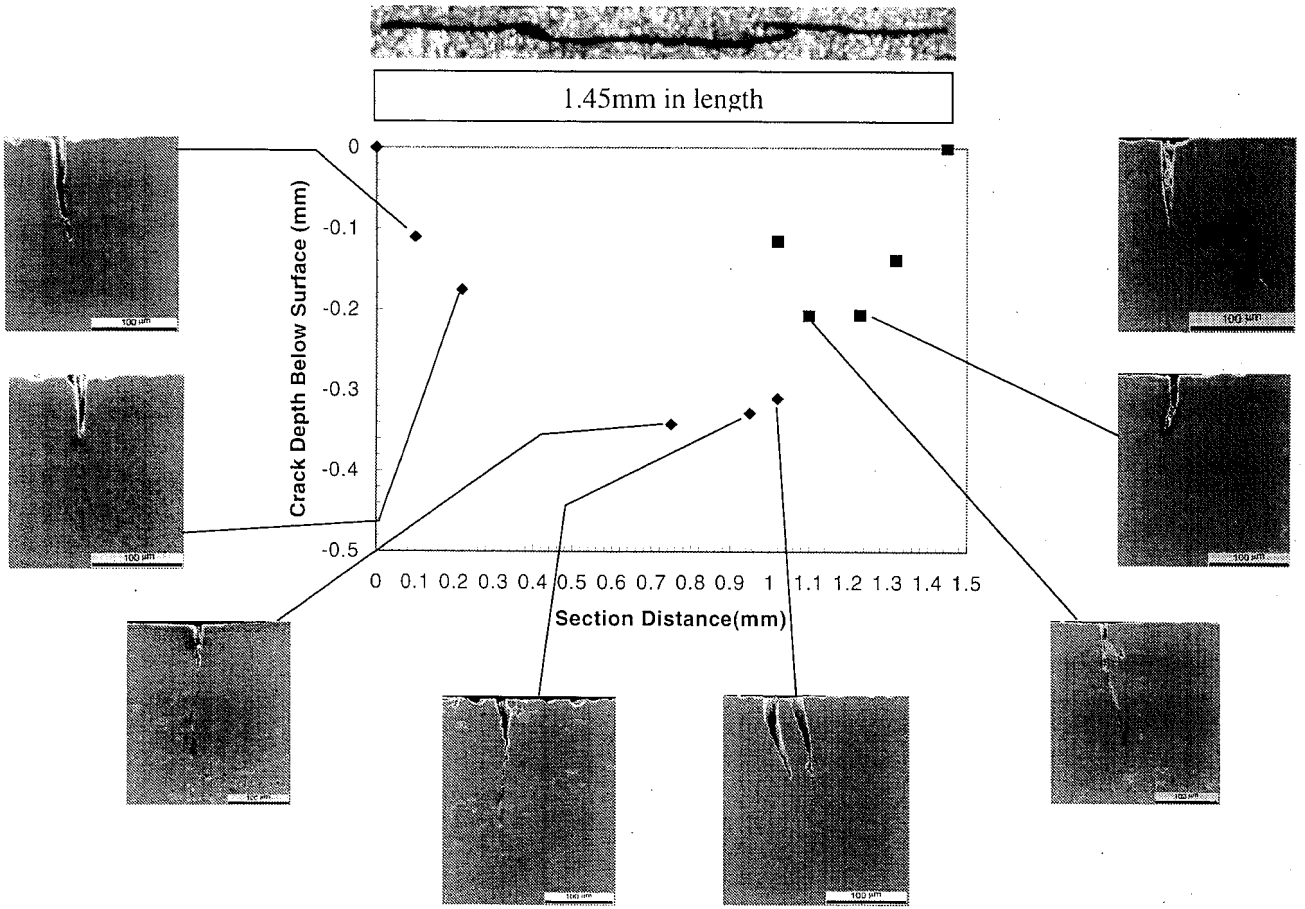

Figure 4.10: Profile with SEM micrographs for Crack #2 on panel B3-2-2.

4.3 Influence on Damage Evolution Processes and Modeling Implications

The results from serial sectioning showed that refinements to the existing mechanistically based probability model need to be made in order to accommodate multiple cracks. The character of multiple damage sites in the fastener holes differed from that of a single, isolated damage site and this needs to be taken into account for a realistic fatigue life model.

Serial sectioning allowed the processes of damage accumulation to be reconstructed as crack profiles as shown in Figures 4.3-4.8 and 4.10 in Chapter 4.2. In this section, a curve is fit to the crack profiles to illustrate how the cracks grow, thereby describing the cracks' influence on the damage evolution processes and modeling. A solid curve is drawn through the points that were measured during serial sectioning to illustrate the crack profile. Dashed curves indicate multiple cracks that have linked up with a dominant crack. It will be seen that the single, dominant cracks (Crack #1 and Crack #3 in hole #32 on panel B3-2-6) nucleated from one isolated damage site and are fairly semi-elliptical in shape, and would have continued to grow in this manner. Multiple cracks that linked-up to form one crack however, are different in character from the single cracks. The multiple cracks each have separate nucleation sites, and they grow independently until link-up occurs, and at a later time the linked-up cracks will grow as one dominant crack.

The constructed profiles for Crack #1 and Crack #3 in hole #32 on panel B3-2-6 are shown in Figures 4.11 and 4.12, respectively. These cracks originated from a single nucleation site and propagated as shown in the profile. Both are practically semi-

elliptical in shape, with the deepest section at a depth of about 40% of the crack length. It should be noted that there may be measurement error in the zero reference point for Crack #3. A pit located to the left of the crack may have served as the zero reference point, and this discrepancy is shown by a dashed curve in Figure 4.12. Neither of these cracks has encountered other damage sites, and are thereby isolated cracks that can be modeled as single dominant cracks, as done previously [1]. However, since the cracks are semi-elliptical in shape as opposed to semi-circular as used in the mechanistically based probability model, modifications to the model should be made to incorporate the geometrical variations.

The cracks grow as a semi-ellipse because of the stress distribution around the crack. Point A in Figure 4.13 corresponds to the surface where cracking occurs in the fastener holes. This figure shows that the stress concentration is three times higher around the surface of the hole (the crack mouth location), and decreases as the crack propagates into the surface. This results in a semi-elliptical growth profile as opposed to semi-circular where the stress distribution may be represented by the equation below [21].

$$\sigma_\theta = \frac{1}{2}\sigma\left(2+\frac{a^2}{r^2}+\frac{3a^4}{r^4}\right) \tag{4.1}$$

where:

σ_θ = stress distribution for the fastener hole and crack
σ = applied stress
a = fastener hole radius
r = radial distance

Serial sectioning of Crack #2 in hole #32 on panel B3-2-6 did not occur at a link-up region of this crack, however, the multiple damage sites and crack growth trends

are shown in Figure 4.14. The dominant crack profile is shown as a solid curve, and the dashed curves represent the smaller multiple cracks. It appears that the left and right link-up sites are shallow damage that linked with more severe elongated damage, joined, and propagated as a dominant crack. The longest damage was the earliest to nucleate from a flaw site since the crack is deepest (0.41mm) at a section in this region. The shallow damage sites formed later, grew independently for some time, and later linked-up with the elongated damage to grow as one crack, as shown in Figure 4.14. Possible refinements to the mechanistically based probability model based on this profile may include information on individual crack growth at the multiple sites during the early stages, and the transition to a dominant crack at the later stages.

The profile and crack growth trend for Crack #4 in hole #32 on panel B3-2-6 is shown in Figure 4.15. Recall that the profile of this crack contains error because serial sectioning did not begin at a point where the entire shallow damage region was included for analysis. Rather, serial sectioning began at approximately 0.20mm into the shallow damage region, so error bars have been added to the data points. It appears that the shallow damage, which unfortunately was not considered, transitions into more severe damage shortly before linking-up with the main crack. The main crack (solid curve) grew for some time before linking with the shallow damage (dashed curve) to form a dominant crack. If growth continued, eventually the main crack would have engulfed the shallow damage and continued to grow as the dominant crack, which may have later linked-up with Crack #5, as potentially seen in Figure 4.1.

The constructed profile and growth trend for Crack #5 in hole #32 on panel B3-2-6 is seen in Figure 4.16. There are four distinct damage sites that have linked-up to form this crack. The elongated damage in the center nucleated earlier than the damage on the left and right ends of the crack, which is in an earlier stage of growth. Each crack initially grew independently of each other, until the elongated damage linked up and grew as a dominant crack, as denoted by the deep, solid curve. The other damage is more shallow, suggesting that these cracks nucleated later. It can be seen that the shallow damage continues to grow independently of the dominant crack, but would have been overcome by the dominant crack if growth continued. The observations made from this crack further the need for model refinements that include the multiple crack damage processes. In addition, the multiple cracks and link-up cause Crack #5 to have lateral and longitudinal spacing which may influence the crack growth rate, and therefore may be considered as an area of future work that would influence the mechanistically based probability model.

For Crack #1 in hole #107 on panel B3-2-2, the profile and growth trends are shown in Figure 4.17. There are three separate crack nucleation sites which have linked-up to form one surface crack. At this point, each crack continues to grow somewhat independently, but their link-up growth is contributing to the formation of a dominant crack where they grow together. The solid curve represents the existing crack front, while the dashed curves illustrate the profile of the multiple cracks before becoming engulfed by the larger crack. It appears that the middle crack nucleated first since it is deepest (0.3mm), and the other cracks that form the link-up nucleated later, but at

approximately the same time since they are at about the same depth. The character of these multiple cracks suggests that changes to the mechanistically based probability model should include early stage crack growth behavior, where the cracks grow independently before a dominant crack forms. This behavior is depicted in Figure 4.17 because a single dominant crack has not yet formed from the link-up. It should be noted that if Crack #1 continued to grow, it would eventually link-up with the cracks toward the wingskin surface, as seen in Figure 4.9.

The final crack that was analyzed was Crack #2 in hole #107 on panel B3-2-2, and its profile with the crack growth trend is shown in Figure 4.18. Crack #2 is made up from three multiple cracks with distinct link-up sites that have formed a single dominant crack, as shown by the solid curve. The dashed curves represent the profile for the multiple cracks before becoming engulfed by the dominant crack. The middle crack nucleated earliest since it is deepest (0.34mm), and the left and right cracks that nucleated later have been engulfed by the dominant crack. Similarly to Crack #5 in hole #32 on panel B3-2-6, there is lateral and longitudinal spacing present with this crack. The findings from the analysis of this crack also suggest that refinements to the mechanistically based probability model should be made by investigating early stage crack growth.

With the abundance of multiple cracks that have linked-up to form one crack in the fastener holes, refinements should be made to the existing mechanistically based probability model to account for the multiple crack damage process. Early crack growth stages where the multiple cracks continue to grow independently should be considered as

a refinement to the model. In addition, it may be worthwhile to investigate when the multiple cracks are growing as a dominant crack in the later stages of growth, whether the early crack growth stages can be ignored and thus modeled as a single dominant crack.

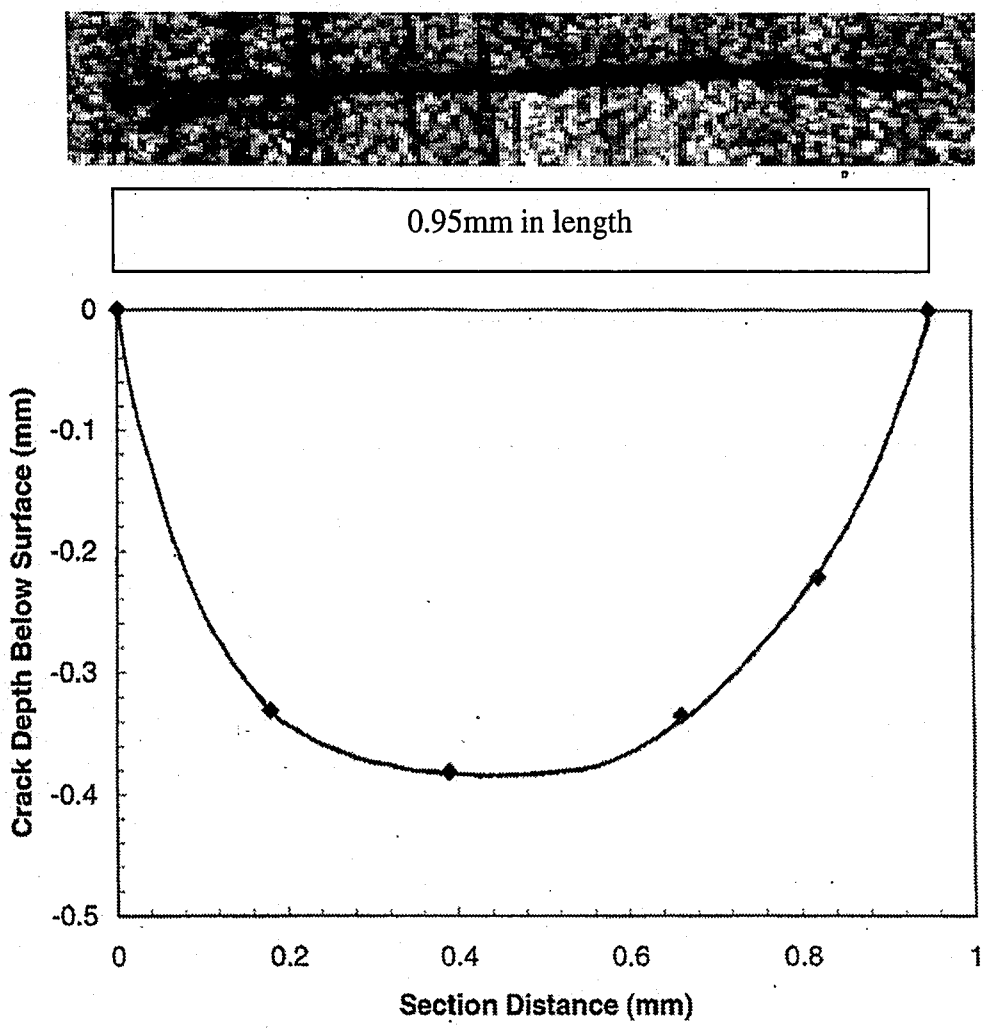

Figure 4.11: Constructed profile showing the growth trend of Crack #1 in hole #32 on panel B3-2-6. Crack #1 is a single, isolated crack.

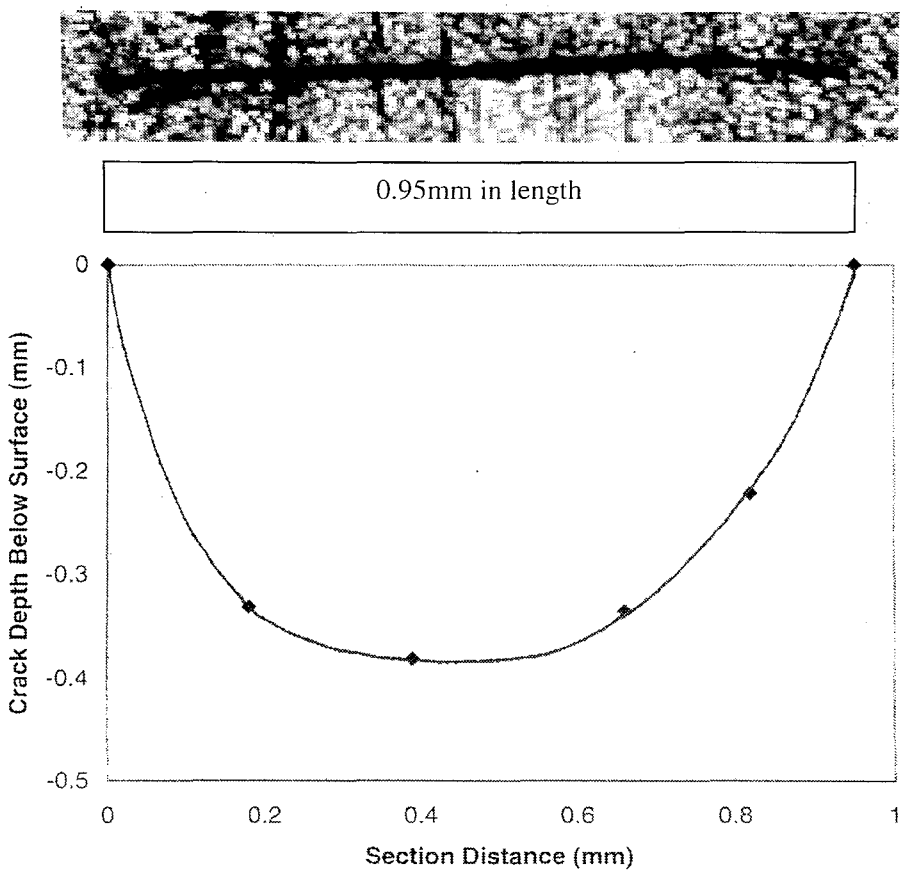

Figure 4.11: Constructed profile showing the growth trend of Crack #1 in hole #32 on panel B3-2-6. Crack #1 is a single, isolated crack.

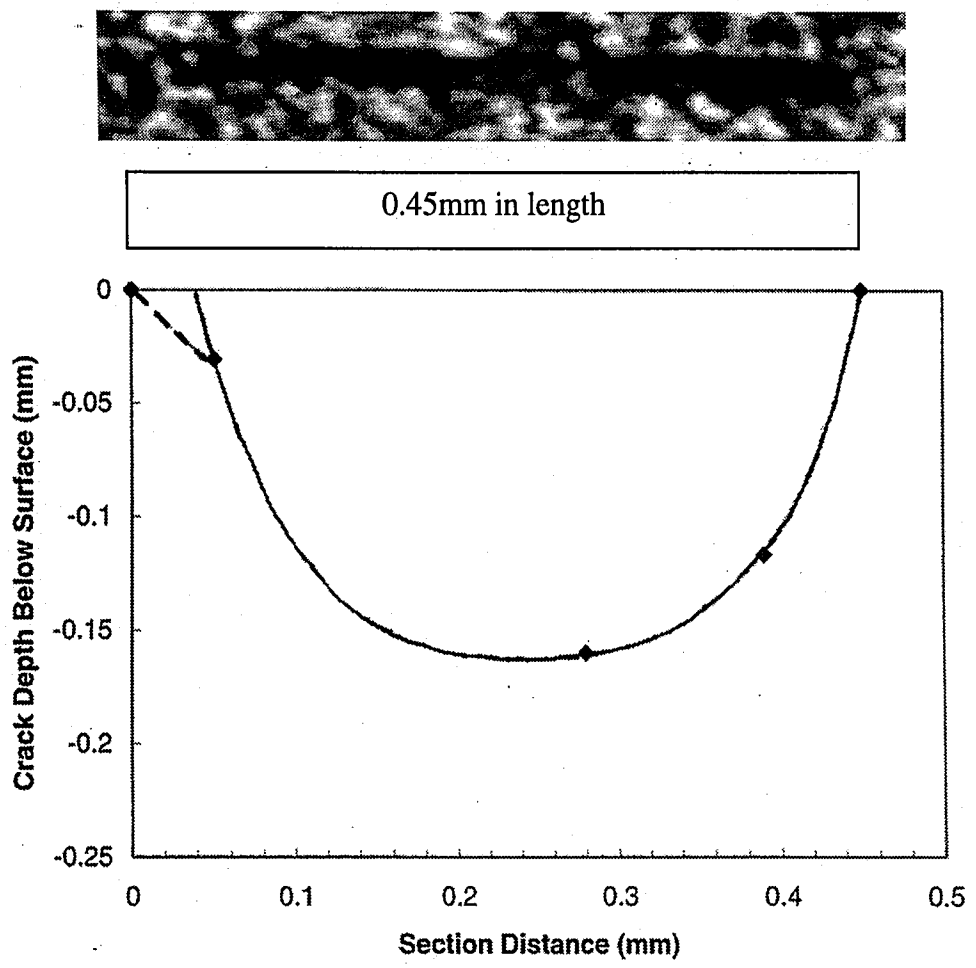

Figure 4.12: Constructed profile showing the growth trend for Crack #3 in hole #32 on panel B3-2-6. Crack #3 is a single, isolated crack.

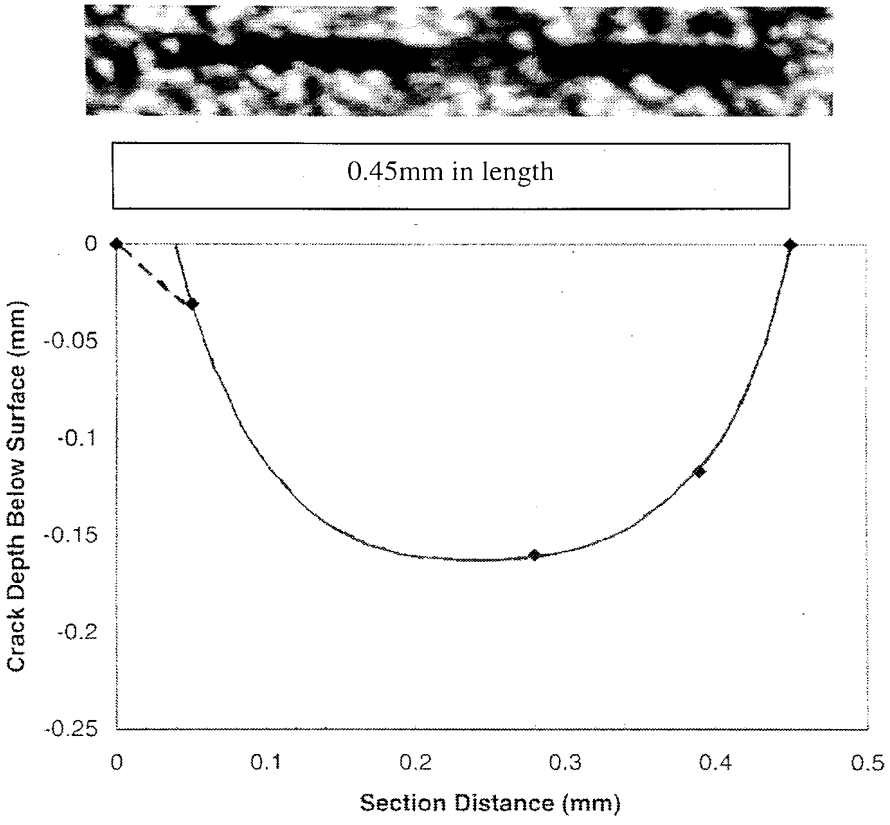

Figure 4.12: Constructed profile showing the growth trend for Crack #3 in hole #32 on panel B3-2-6. Crack #3 is a single, isolated crack.

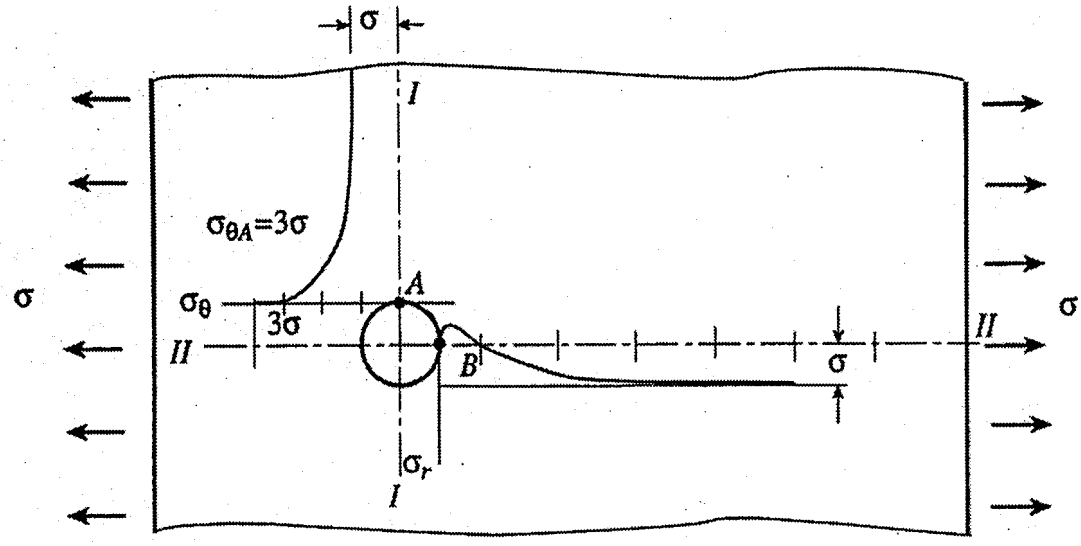

Figure 4.13: Stress distribution around a fastener hole. This behavior explains why the observed cracks have a semi-elliptical profile [21].

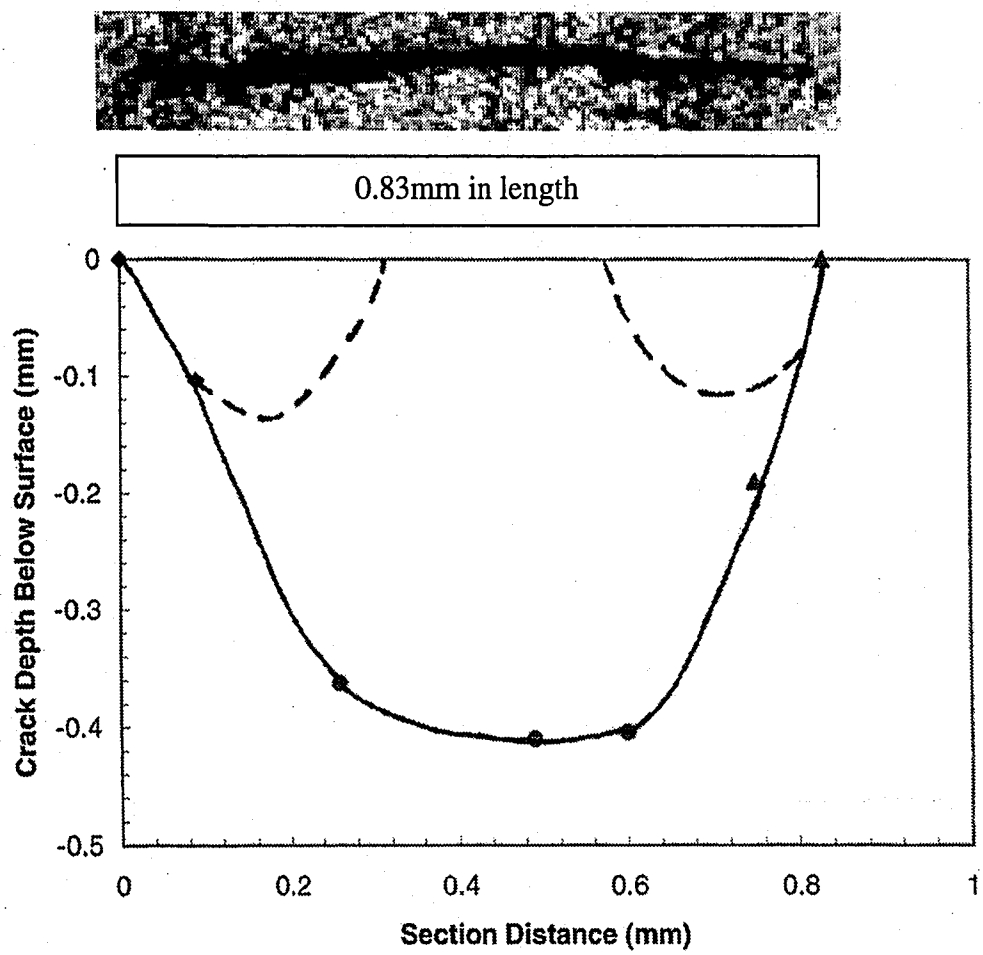

Figure 4.14: Constructed profile showing the growth trend for Crack #2 in hole #32 on panel B3-2-6. Crack #2 consists of multiple cracks.

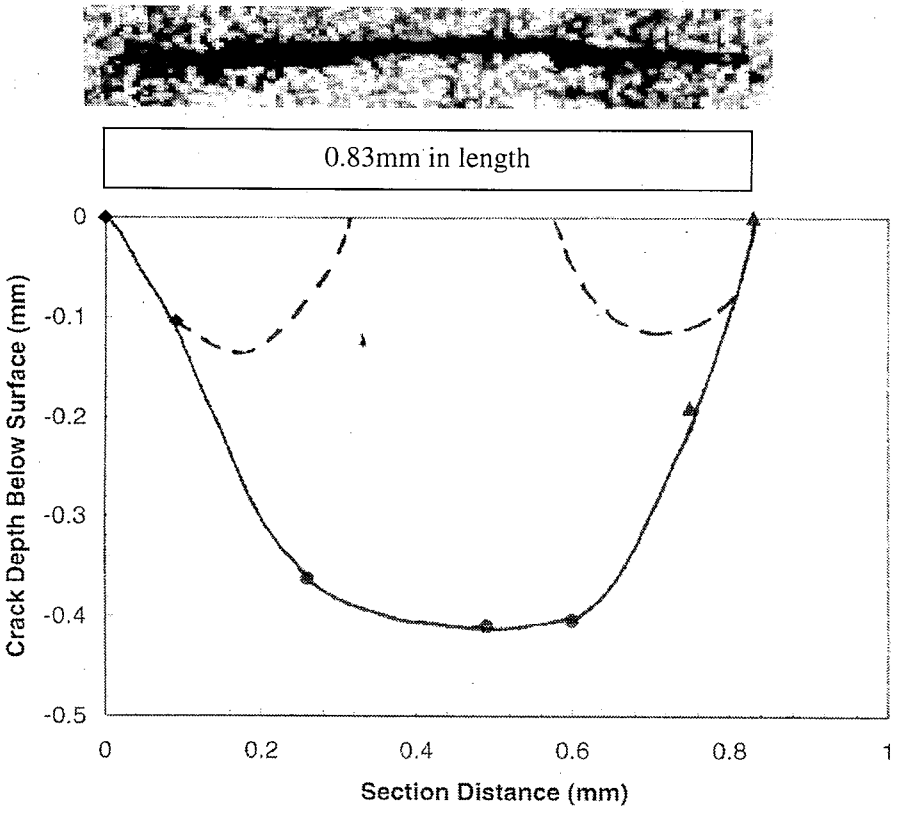

Figure 4.14: Constructed profile showing the growth trend for Crack #2 in hole #32 on panel B3-2-6. Crack #2 consists of multiple cracks.

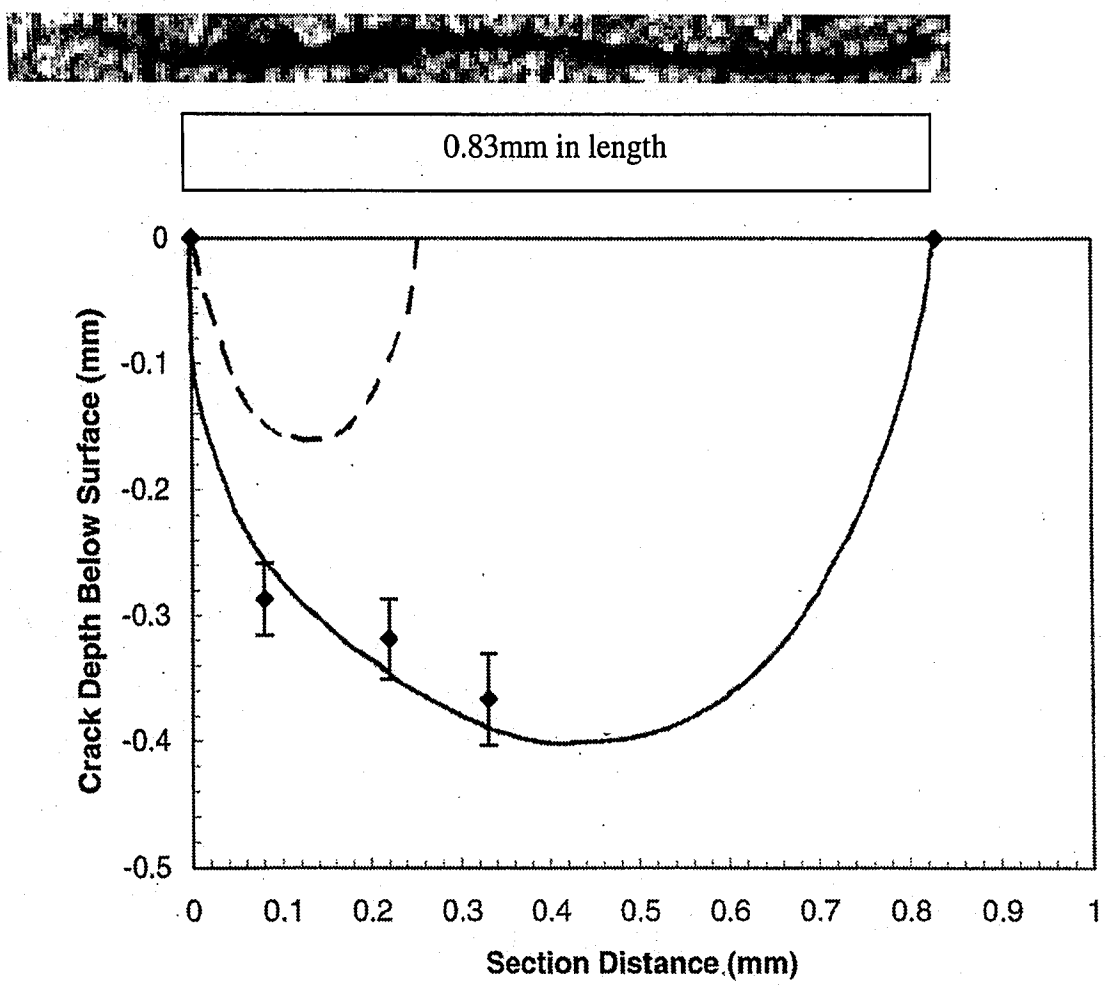

Figure 4.15: Constructed profile showing the growth trend for Crack #4 in hole #32 on panel B3-2-6. Error bars are as a result of measurement error. Crack #4 consists of multiple cracks.

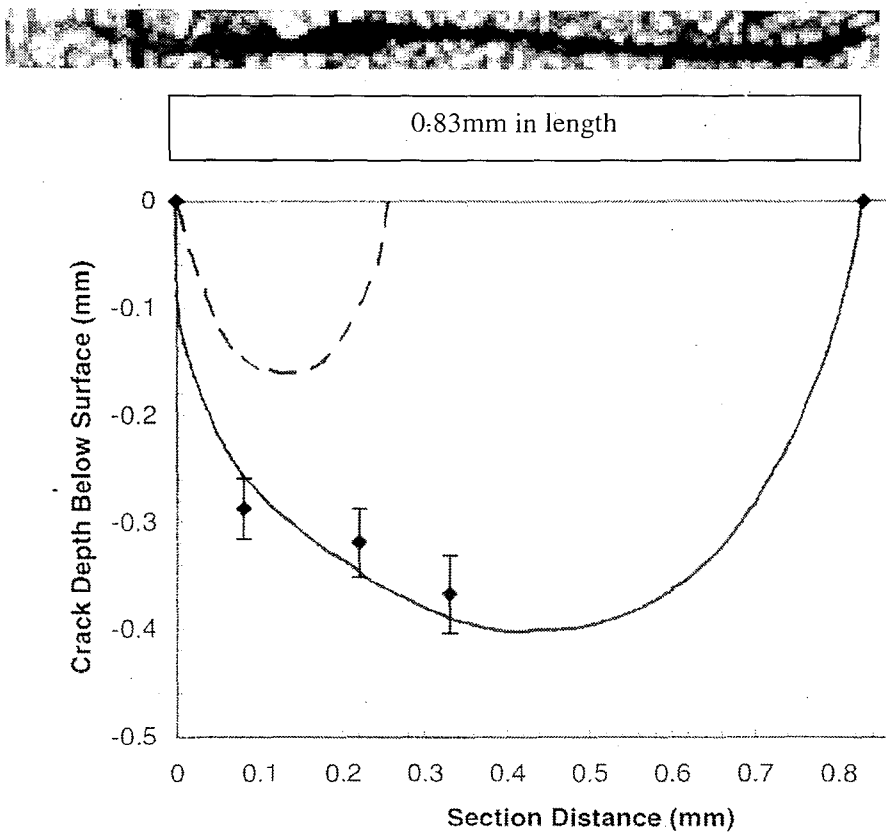

Figure 4.15: Constructed profile showing the growth trend for Crack #4 in hole #32 on panel B3-2-6. Error bars are as a result of measurement error. Crack #4 consists of multiple cracks.

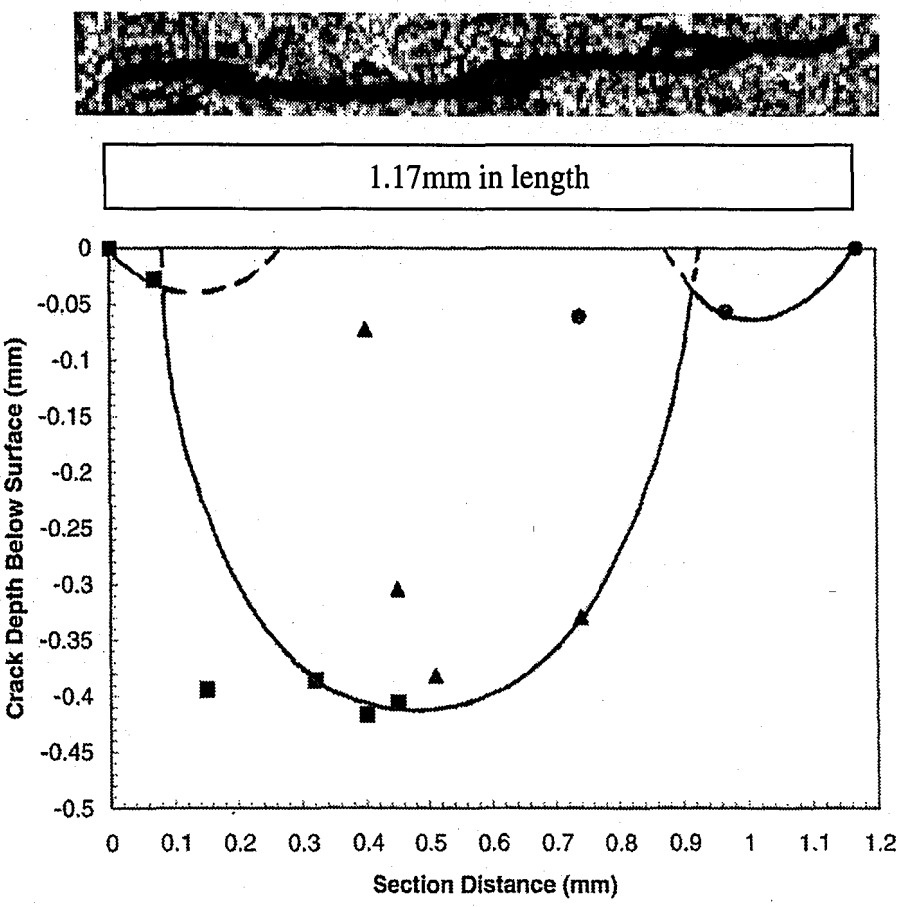

Figure 4.16: Constructed profile showing the growth trend for Crack #5 in hole #32 on panel B3-2-6. Crack #5 consists of multiple cracks.

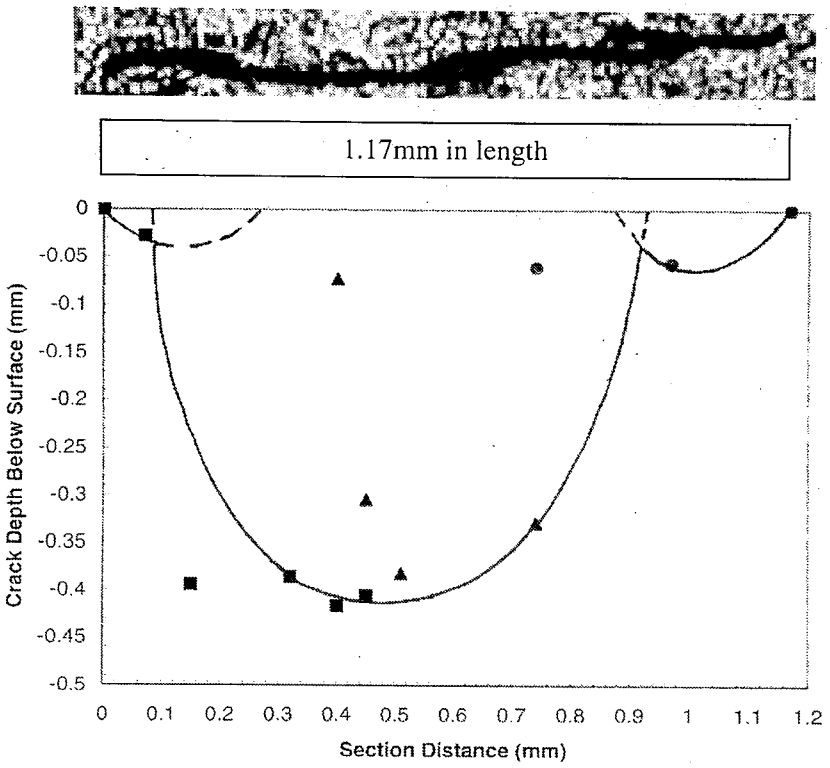

Figure 4.16: Constructed profile showing the growth trend for Crack #5 in hole #32 on panel B3-2-6. Crack #5 consists of multiple cracks.

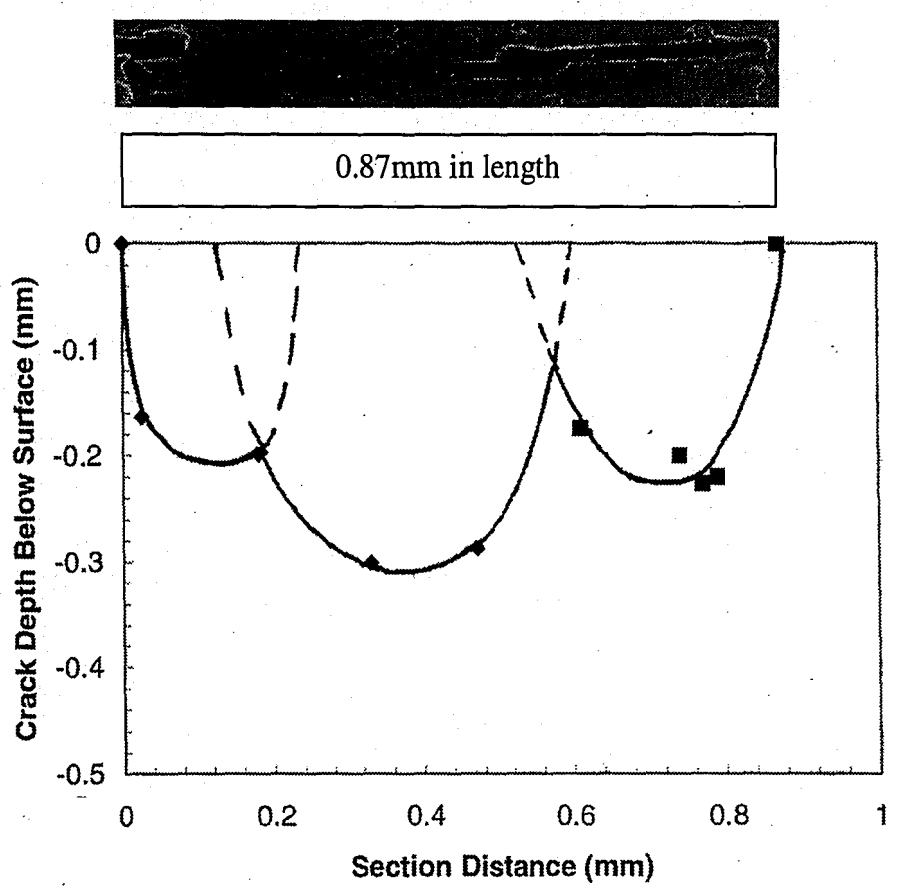

Figure 4.17: Constructed profile showing the growth trend of Crack #1 in hole #107 on panel B3-2-2. Crack #1 consists of multiple cracks.

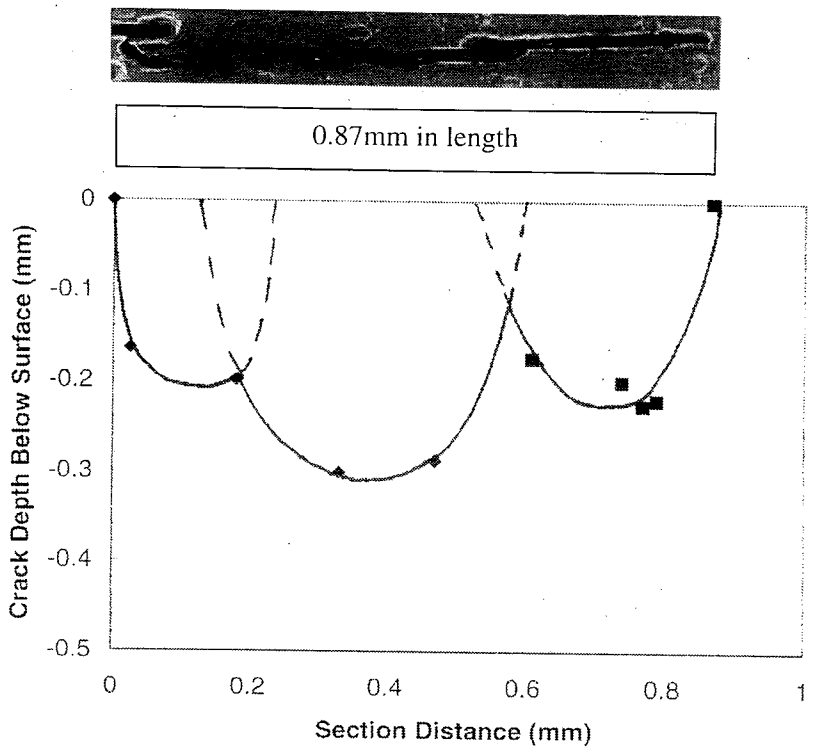

Figure 4.17: Constructed profile showing the growth trend of Crack #1 in hole #107 on panel B3-2-2. Crack #1 consists of multiple cracks.

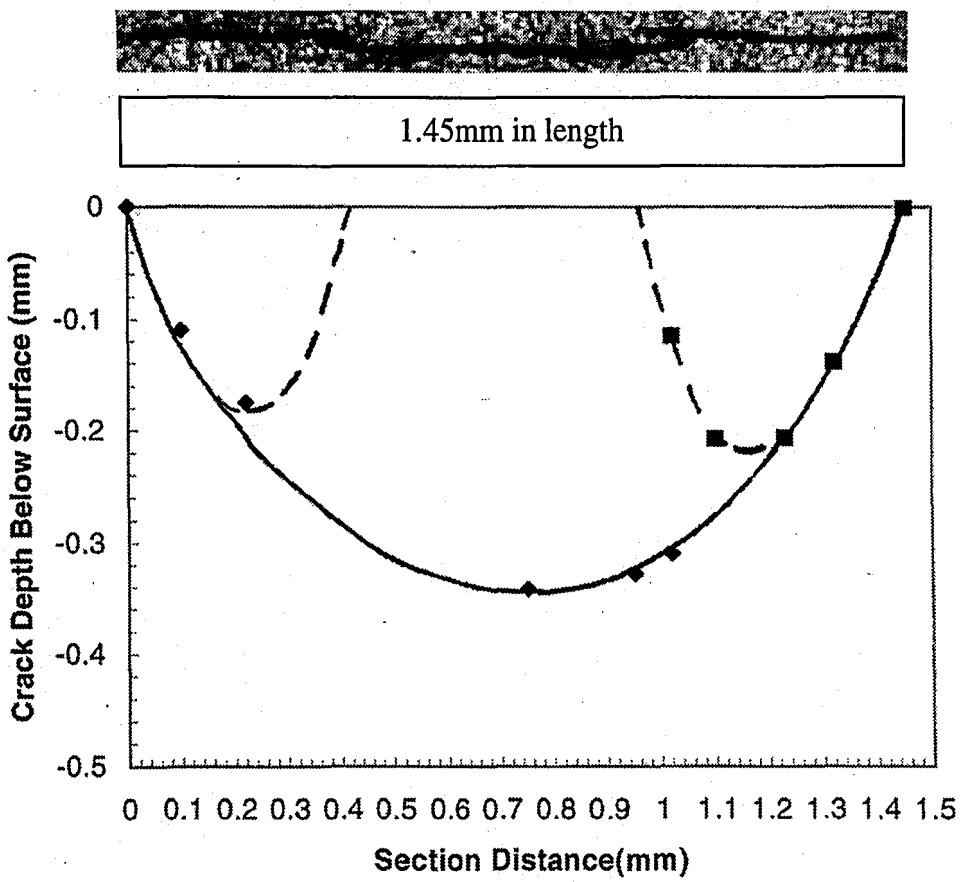

Figure 4.18: Constructed profile showing the growth trend for Crack #2 in hole #107 on panel B3-2-2. Crack #2 consists of multiple cracks.

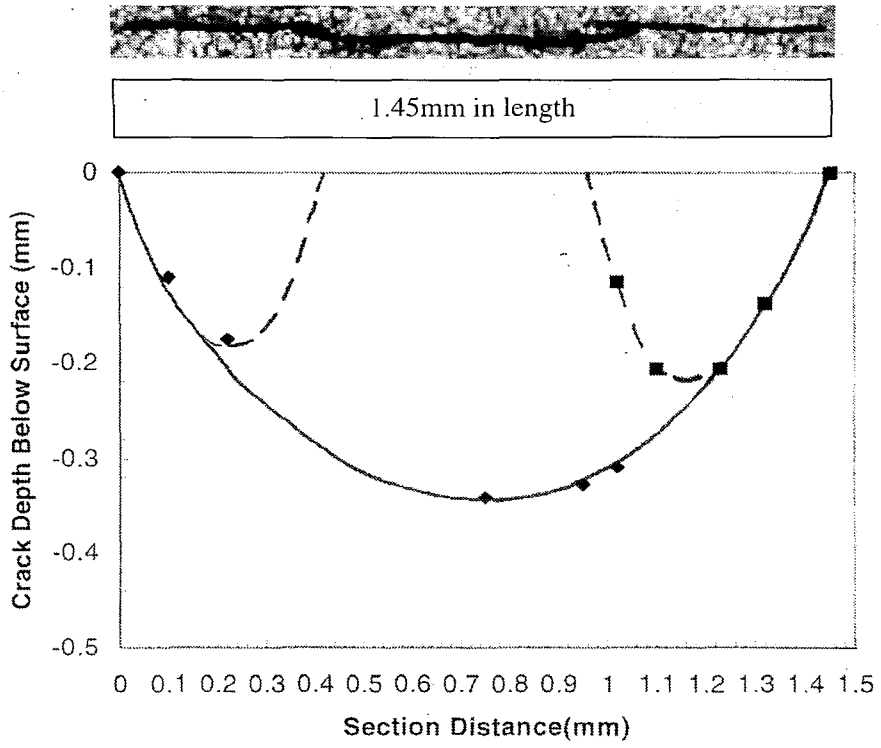

Figure 4.18: Constructed profile showing the growth trend for Crack #2 in hole #107 on panel B3-2-2. Crack #2 consists of multiple cracks.

4.4 Statistical Analysis

The probability of occurrence (PoO) for all multiple hole-wall crack (MHWC) lengths for hole #32 on panel B3-2-6 and hole #107 on panel B3-2-2 is shown in Figure 4.19. This plot shows the probability of occurrence for which the damage size in the hole is larger than a given damage size, *a*. The damage size was measured by using the Hi-Scope™ to obtain images of the fastener holes surface and importing the images into Adobe Photoshop. A calibration factor was obtained using the travelling microscope so that the crack lengths could be measured in Photoshop. Hole #32 had 68 identifiable damage sites, while 34 were present in hole #107.

The PoO shown in Figure 4.19 is in good agreement with the PoO for the preliminary inspection, which is shown in Chapter 2, Figure 2.7. It should be noted that in Figure 4.19, multiple cracks were measured individually, where the individual crack lengths which make up the total length were used rather than the total length. In addition, repeated crack lengths were independently accounted for in this model, and they appear as vertically aligned points. The PoO in Figure 2.7 uses the total length of the multiple crack and does not independently account for repeated crack lengths.

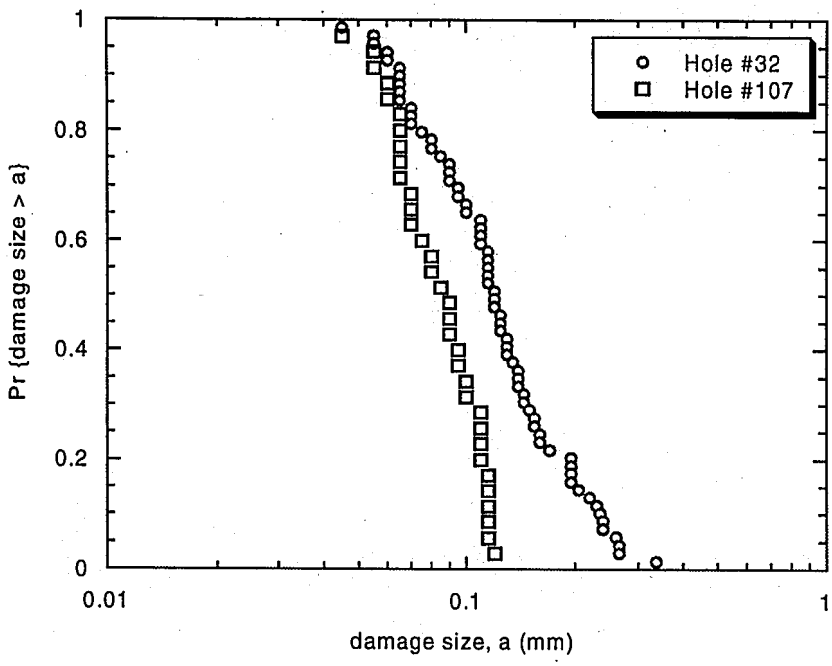

Figure 4.19: PoO for all MHWC lengths for Hole #32 and Hole #107 measured using video imaging microscopy.

4.5 Non-Destructive Inspection (NDI)

NDI techniques were performed on one-half of hole #107 from panel B3-2-2 with the help of Jerrold Green and Richard Brazill at ALCOA. The hole that was inspected using NDI is the same hole for which serial sectioning was later performed. This hole was selected for NDI because of its two distinct regions of cracking. Cracking occurs near the wingskin surface of the hole and also about midway along the fastener hole. If NDI can detect the cracks in these regions, it will output an image that clearly shows discontinuities where cracking occurs, and how the cracks are distributed along the fastener hole. Since it appears that no significant surface cracking occurs for a distance of about 1mm between the two regions of cracking (see Figure 4.2), it is expected that the NDI techniques will not show crack discontinuities in the output for this area.

The specimen was placed in a medium of water, and ultrasonic waves traveled thorough the water to the fastener hole in a direction perpendicular to the cracks, as described in Chapter 3.3. If the waves reach a crack, or a discontinuity in the material, the image returned will show the location of the crack and its depth into the material. NDI output is shown for this hole in Figure 4.20. Certainly NDI has acknowledged that damage exists in the fastener holes, but the resolution of this technique is inadequate for determining the character of cracks. The actual shape of the damage cannot be discerned from these figures, although it does show that relatively shallow and deep damage exists in the hole.

Other inadequacies with NDI techniques for these fastener holes is that if any damage is "hidden" behind a larger crack, eg., if a crack 0.2mm in depth is behind a

crack 0.3mm in depth, the more shallow crack will not appear on the output. In other words, smaller damage sites are blocked by larger damage sites and will not be detected using this NDI technique. Similarly, if there is deeper damage behind the first detected crack, it will not show that there are separate cracks, but it will appear as if the deeper damage is part of the smaller detected crack. It is also unlikely that fine cracks, near the crack tip especially, will be detected using NDI since the resolution for even large damage is not good.

Although NDI acknowledges the presence of damage in the fastener holes, it is not adequate for a fastener hole with multiple cracks along the surface and through the thickness. The actual shape of damage for multiple cracks cannot be resolved from the output, and not all cracks will be detected. Perhaps for a single, isolated crack in a fastener hole NDI would return better results.

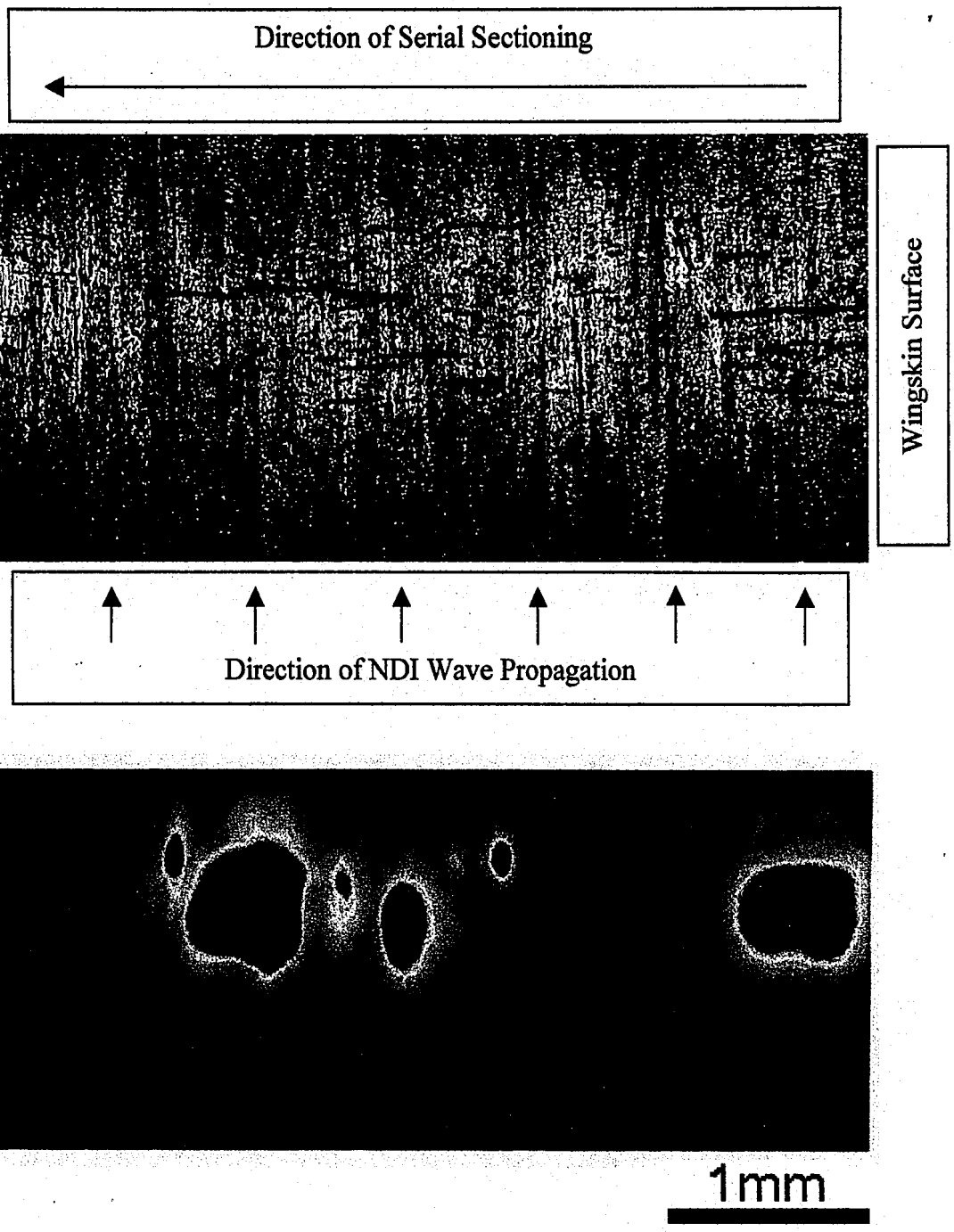

Figure 4.20: NDI photo of hole #107 on panel B3-2-2. NDI was performed with assistance from ALCOA.

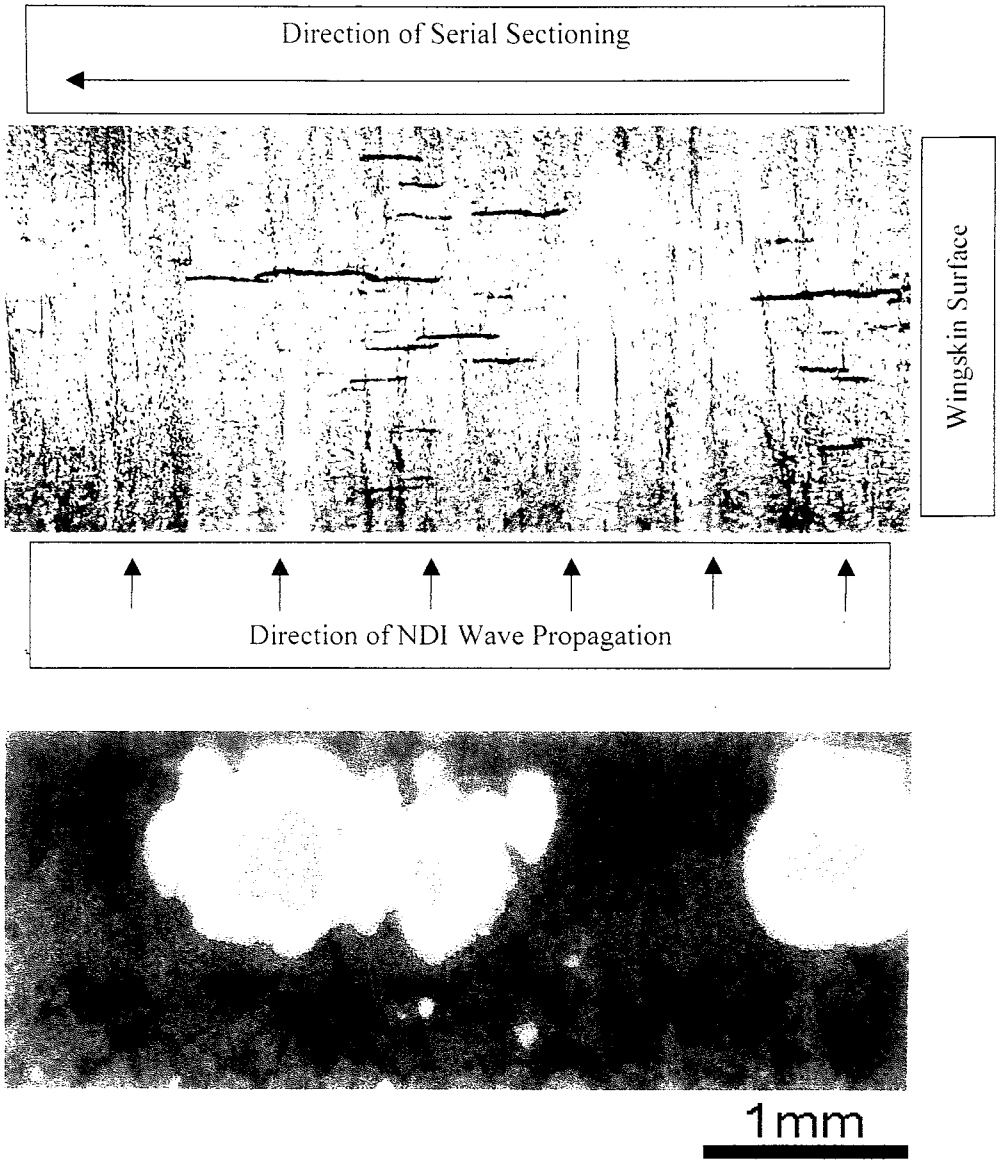

Figure 4.20: NDI photo of hole #107 on panel B3-2-2. NDI was performed with assistance from ALCOA.

CHAPTER 5 – SUMMARY AND FUTURE WORK

5.1 Summary

A detailed metallographic analysis was conducted to characterize the accumulated corrosion fatigue (CF) damage in the fastener holes of a torn-down Boeing 707. A more detailed investigation of the fastener holes allowed the actual shape of the damage and the character of multiple cracks to be determined. Based on the findings, the information will be used to make refinements to the existing mechanistically based probability model and in doing so, improve the model.

Serial sectioning was performed on selected fastener holes constructed of 2024-T3 aluminum alloy from the lower left wingskin panel of a 24 year old B707-321B aircraft. Single, isolated cracks and multiple cracks that linked together to form a single crack were sectioned to reveal the shape of these cracks. Optical and scanning electron microscopy (SEM) observations of the sections were made to measure the geometry of the cracks and to obtain micrographs so that a crack profile could be constructed. This illustrated the character of the cracks and their growth trends.

It was determined that the crack profiles were semi-elliptical in shape, as opposed to semi-circular as previously modeled. This semi-elliptical crack growth occurs as a result of higher stress concentrations at the surface edges of the crack, with decreasing stress elevation in the direction of crack depth. The existing mechanistically based probability model must be refined to include this actual geometry and stress distribution so that more accurate predictions can be made.

A detailed analysis also revealed that multiple cracks linking-up to form a single crack differ in character from a single, isolated crack and therefore should not be modeled as a single dominant crack. This is especially true when crack growth is in the early stages. In the early stages of crack growth, the multiple cracks grow independently of each other until they join. Once they join, or link-up, they continue to grow independently until a dominant crack is formed. This dominant crack will outgrow and engulf the other cracks that have linked-up in the later stages of growth. Once the cracks link-up and grow as a dominant crack, it may be suitable to model such behavior as a single, dominant crack, but further work is needed in this area. In the meantime, the mechanistically based probability model must be refined to include geometrical variations as well as the character of multiple cracks.

6.2 Future Work

While the work done for this research has established the character of CF damage in an aircraft's fastener holes, more work remains to be done. This research prompted the need for refinement to the mechanistically based probability model in terms of crack geometry and multiple versus single crack character. Therefore, a project that incorporates this information into the existing model and produces results would be useful. A comparison of the refined model to the preliminary model could then be conducted.

A study that investigates the early stages of multiple crack growth would be interesting, especially since many cracks are made up of multiple cracks. Further

analysis of multiple damage should be performed, and perhaps it would reveal that following the early stages of crack growth, the multiple cracks could be ignored and thus modeled as one dominant crack. However, the early stages of multiple crack growth still must be accounted for in the model. Further work on the influence of lateral and longitudinal spacing of multiple cracks could also be conducted. Another possible research area involves the transition from early crack growth (multiple crack are growing individually), to link-up, and finally later crack growth (cracks have linked-up and a dominant crack prevails). This will examine the behavior of how multiple cracks form and develop into a single crack.

Although non-destructive inspection (NDI) techniques were not used extensively in this research due to resolution problems, it would be interesting to continue with fatigue crack analysis using a method other than serial sectioning. By locating a fastener hole that is not severely cracked, or having a single crack in an isolated area, NDI may yield good results. Other NDI techniques should be explored if the resources are available.

APPENDIX A

Serial Sectioning Measurements for the Fastener Holes

Table A.1: Crack Measurements for Crack #1 of Hole #32 on Panel B3-2-6.

Crack Length = 0.945mm

Section Number	Section Distance (mm)	Crack Depth (μm)
1	0.18	331
2	0.39	381
3	0.66	335
4	0.82	222

Table A.2: Crack Measurements for Crack #2 of Hole #32 on Panel B3-2-6.

Crack Length = 0.83mm

Section Number	Section Distance (mm)	Crack Depth (μm)
1	0.09	104
2	0.26	362
3	0.49	410
4	0.60	407
5	0.75	190

Table A.3: Crack Measurements for Crack #3 of Hole #32 on Panel B3-2-6.

Crack Length = 0.446mm

Section Number	Section Distance (mm)	Crack Depth (μm)
1	0.05	31
2	0.28	160
3	0.39	117

Table A.4: Crack Measurements for Crack #4 of Hole #32 on Panel B3-2-6.

Crack Length = 0.83mm

Section Number	Section Distance (mm)	Crack Depth (μm)
1	0.08	287
2	0.22	319
3	0.33	367

Table A.5: Crack Measurements for Crack #5 of Hole #32 on Panel B3-2-6.

Crack Length = 1.17mm ** (L) denotes crack link-up measurement **

Section Number	Section Distance (mm)	Crack Depth (μm)
1	0.07	28
2	0.15	394
3	0.32	386
4	0.40	73(L) 417
5	0.45	305(L) 406
6	0.51	382(L)
7	0.74	61(L-1) 329(L)
8	0.97	57(L-1)

Table A.6: Crack Measurements for Crack #1 of Hole #107 on Panel B3-2-2.

Crack Length = 0.865mm ** (L) denotes crack link-up measurement **

Section Number	Section Distance (mm)	Crack Depth (μm)
1	0.025	164
2	0.18	199
3	0.33	301
4	0.47	287
5	0.61	174(L)
6	0.74	200(L)
7	0.77	226(L)
8	0.79	220(L)

Table A.7: Crack Measurements for Crack #2 of Hole #107 on Panel B3-2-2.

Crack Length = 1.45mm ** (L) denotes crack link-up measurement **

Section Number	Section Distance (mm)	Crack Depth (μm)
1	0.1	110
2	0.22	175
3	0.75	342
4	0.95	328
5	1.02	115 (L) 310
6	1.10	207(L)
7	1.23	206(L)
8	1.32	138(L)

APPENDIX B

SEM micrographs for Crack #4 in Hole #32 on Panel B3-2-6

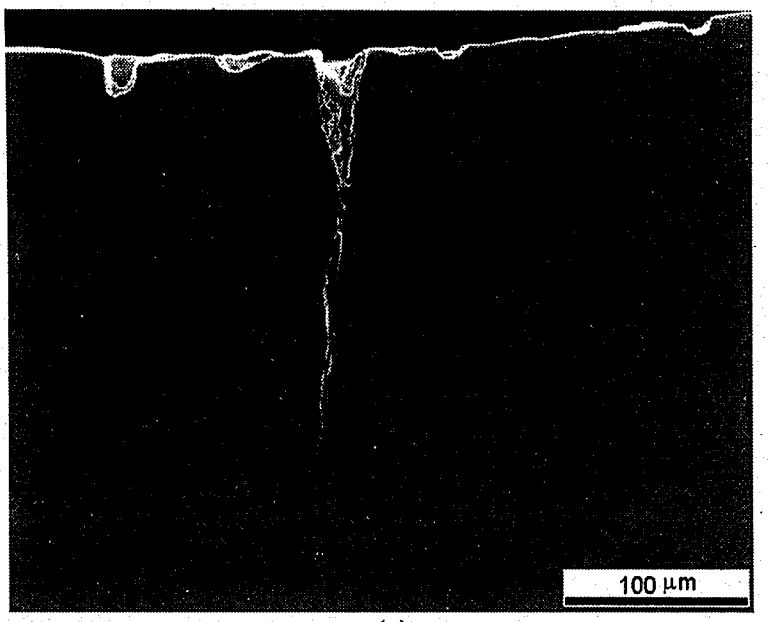

(a)

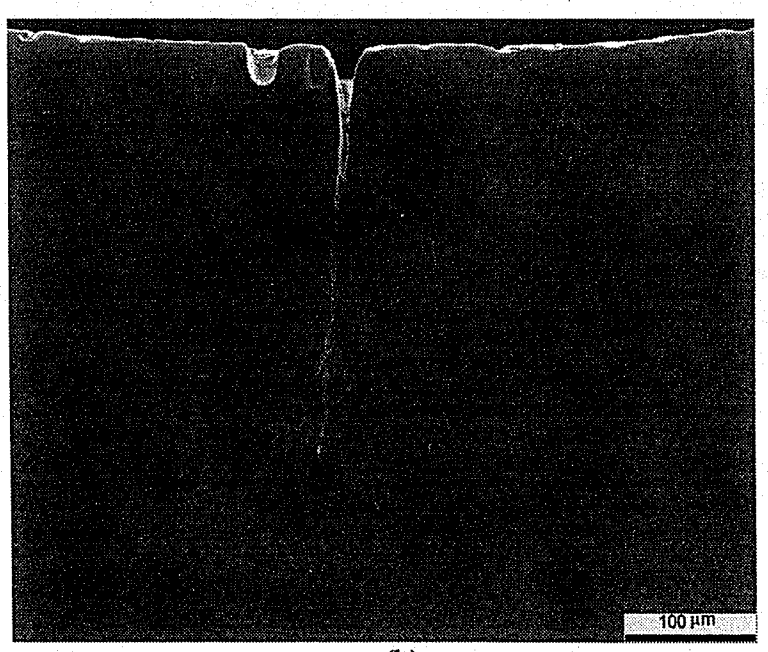

(b)

Figure B.1: SEM micrographs shown of Crack #4 in hole #32 on panel B3-2-6 for (a) Section 2 at 270X and (b) Section 3 at 170X.

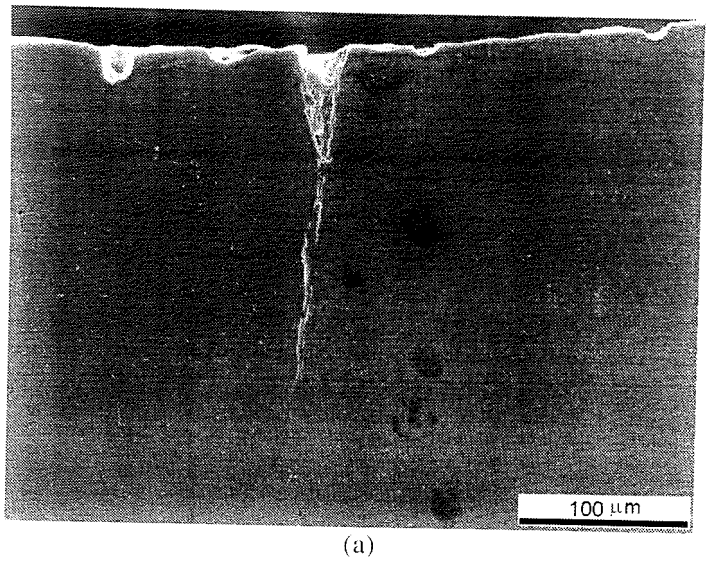

(a)

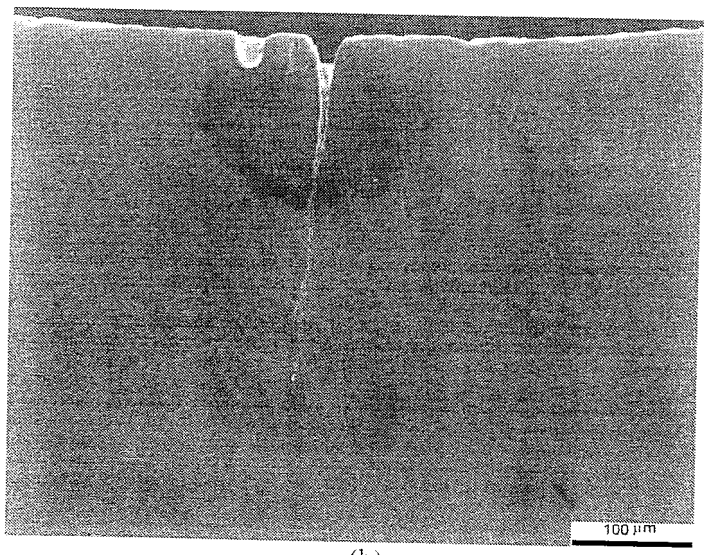

(b)

Figure B.1: SEM micrographs shown of Crack #4 in hole #32 on panel B3-2-6 for (a) Section 2 at 270X and (b) Section 3 at 170X.

APPENDIX C

SEM micrographs for Crack #5 in Hole #32 on Panel B3-2-6

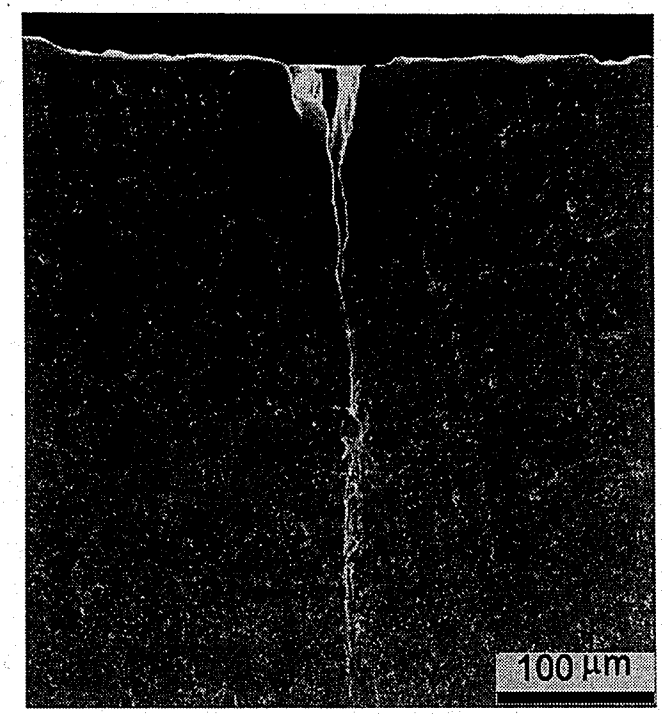

(a)

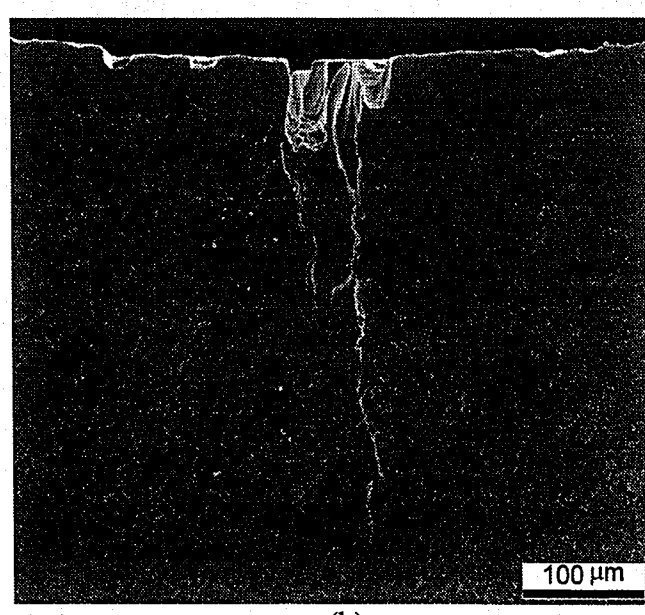

(b)

Figure C.1: SEM micrographs for Crack #5 in hole #32 on panel B3-2-6 taken for (a) Section 4 at 160X and (b) Section 5 at 170X.

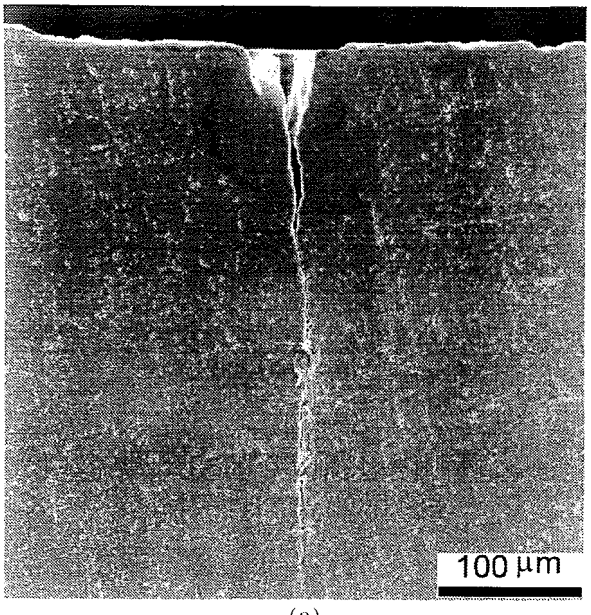

(a)

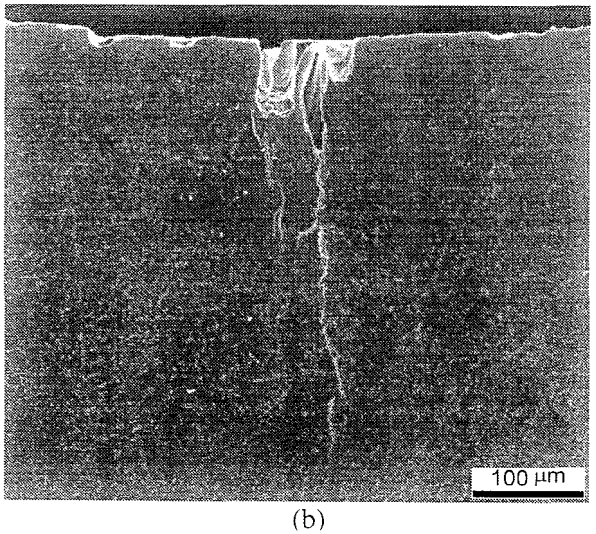

(b)

Figure C.1: SEM micrographs for Crack #5 in hole #32 on panel B3-2-6 taken for (a) Section 4 at 160X and (b) Section 5 at 170X.

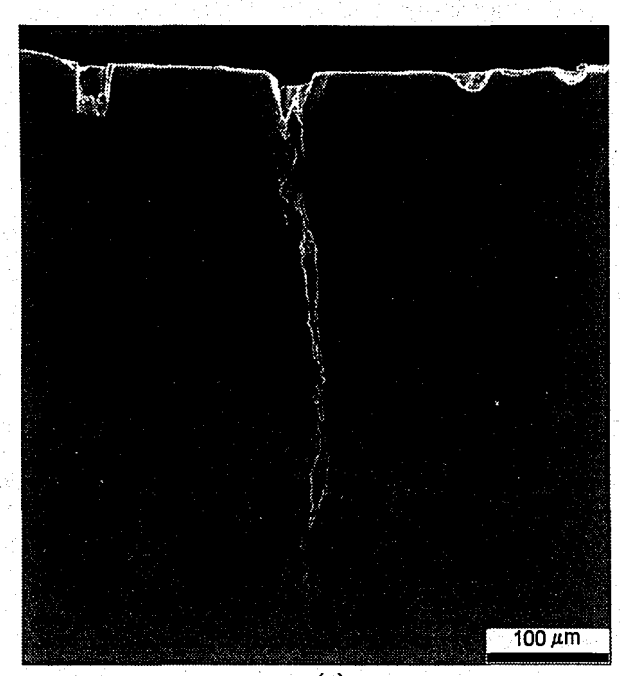

(c)

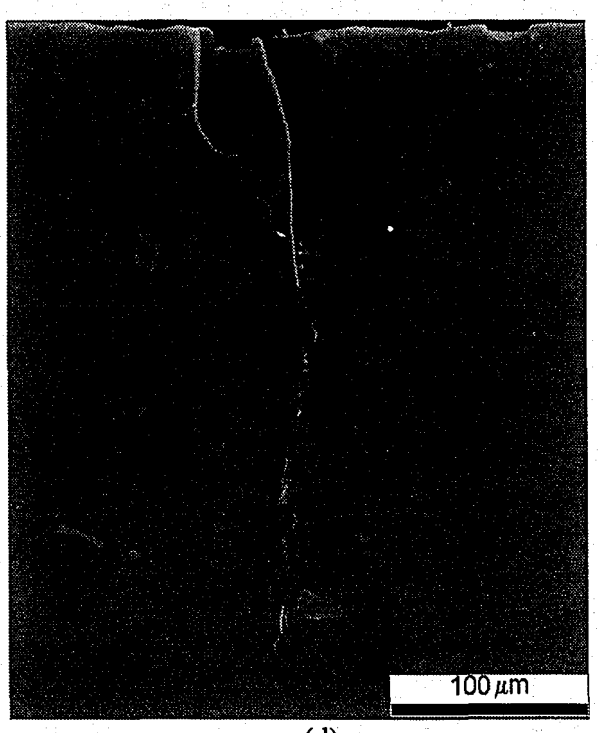

(d)

Figure C.1 (cont'd): SEM micrographs for Crack #5 in hole #32 on panel B3-2-6 taken for (c) Section 6 at 180X and (d) Section 7 at 200X.

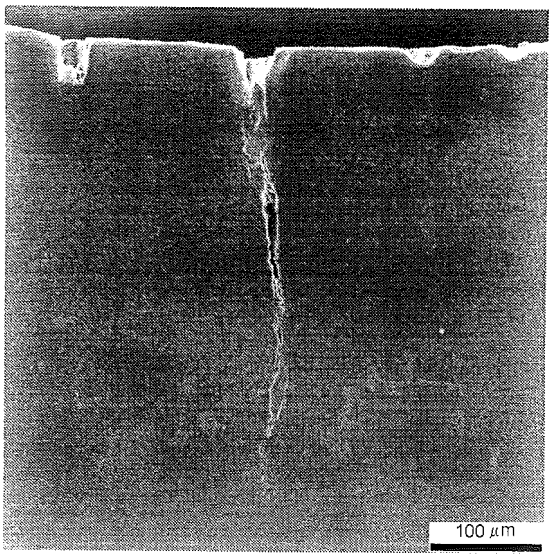

(c)

(d)

Figure C.1 (cont'd): SEM micrographs for Crack #5 in hole #32 on panel B3-2-6 taken for (c) Section 6 at 180X and (d) Section 7 at 200X.

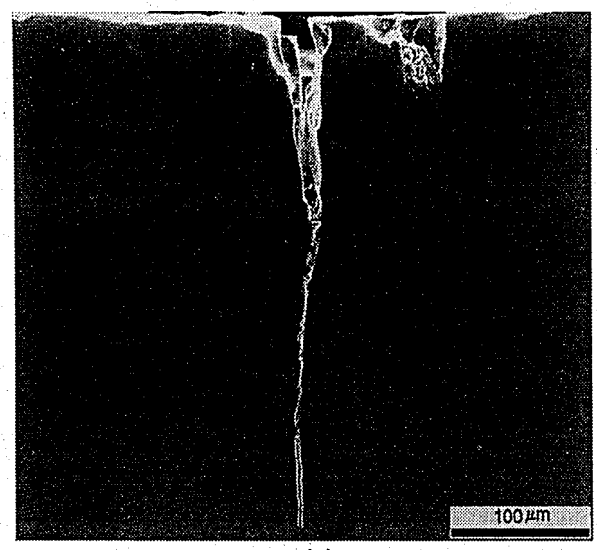

(e)

Figure C.1 (cont'd): SEM micrographs for Crack #5 in hole #32 on panel B3-2-6 taken for (e) Section 8 at 200X.

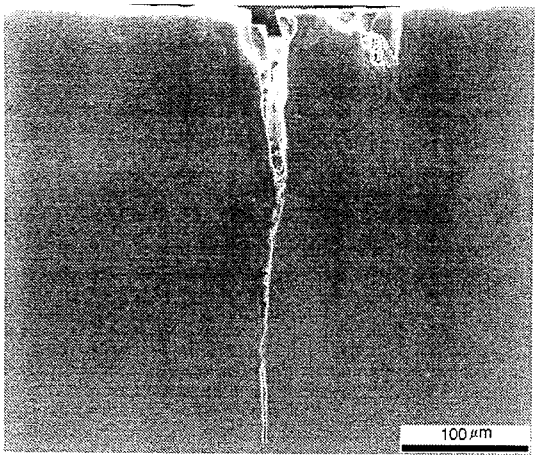

(e)

Figure C.1 (cont'd): SEM micrographs for Crack #5 in hole #32 on panel B3-2-6 taken for (e) Section 8 at 200X.

APPENDIX D

SEM micrographs for Crack #1 in Hole #107 on Panel B3-2-2

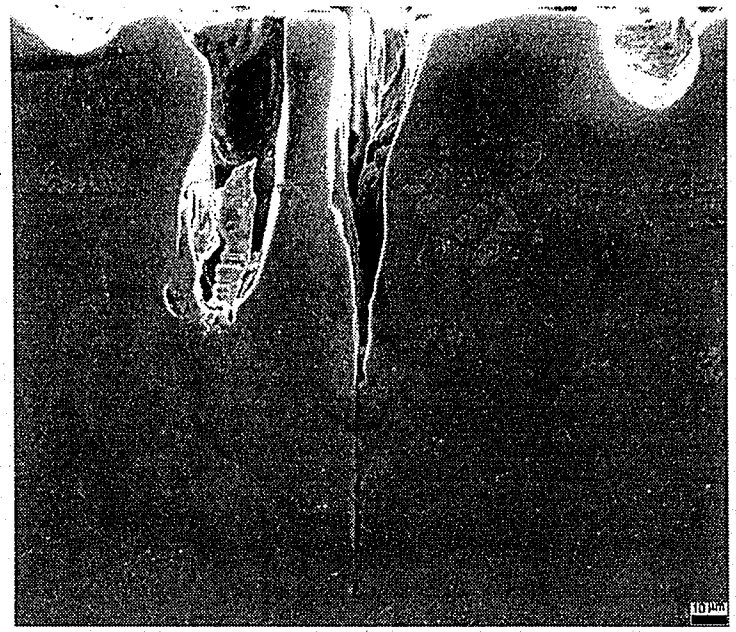

(a)

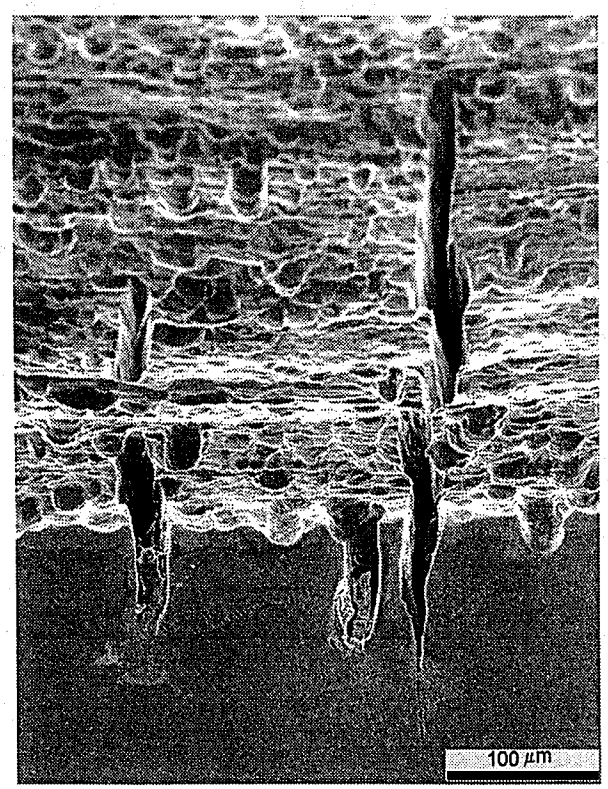

(b)

Figure D.1: SEM micrographs for Crack #1 in hole #107 on panel B3-2-2 taken for (a) Section 1 at 450X and (b) 30° tilted micrograph at 200X for Section 1.

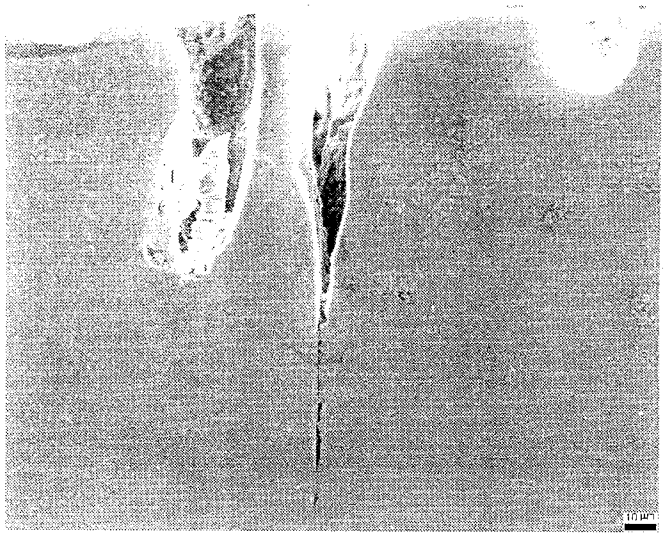

(a)

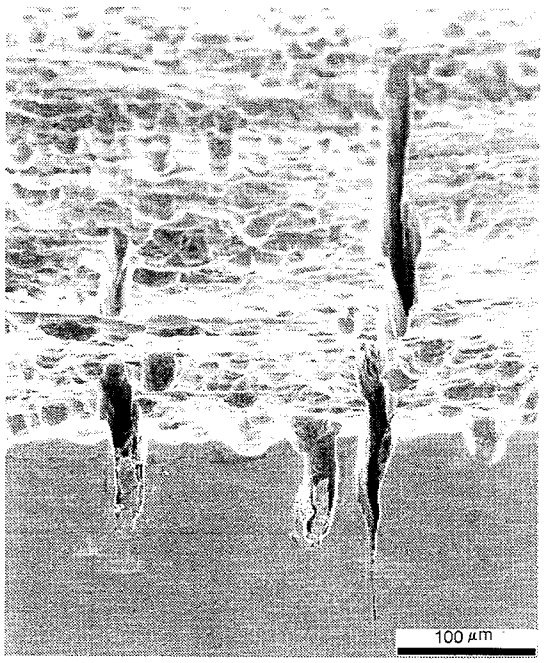

(b)

Figure D.1: SEM micrographs for Crack #1 in hole #107 on panel B3-2-2 taken for (a) Section 1 at 450X and (b) 30° tilted micrograph at 200X for Section 1.

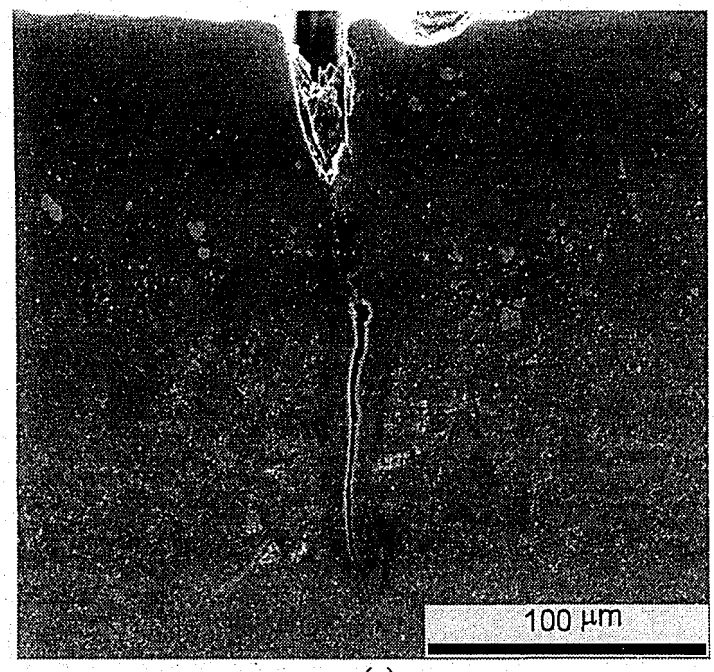

(a)

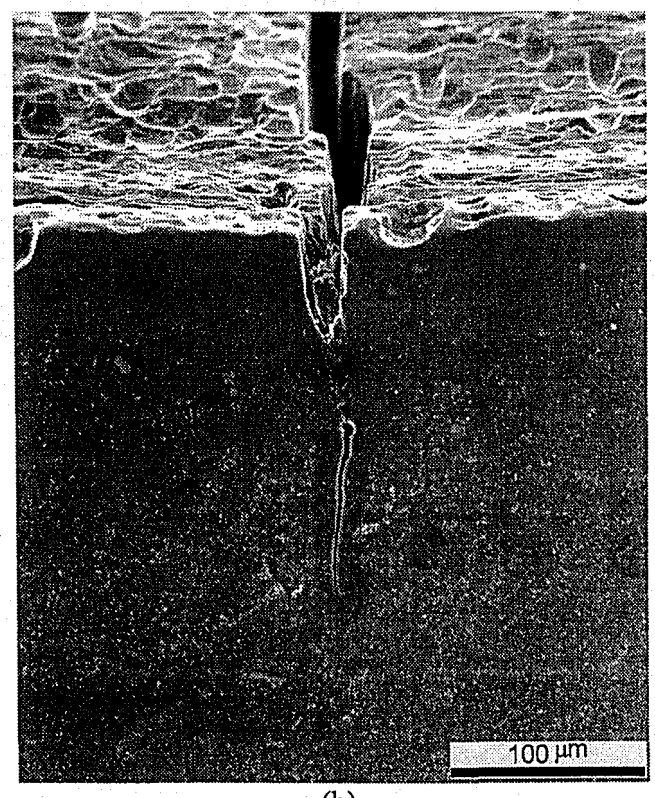

(b)

Figure D.2: SEM micrographs for Crack #1 in hole #107 on panel B3-2-2 taken for (a) Section 2 at 200X and (b) 30° tilted micrograph at 250X for Section 2.

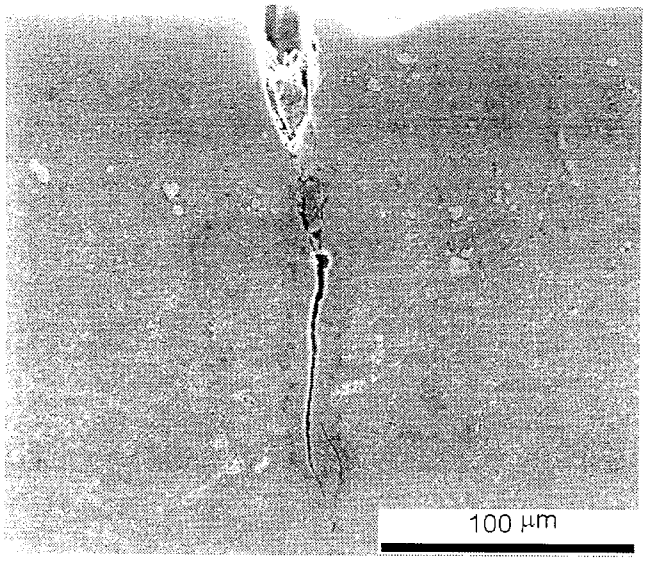

(a)

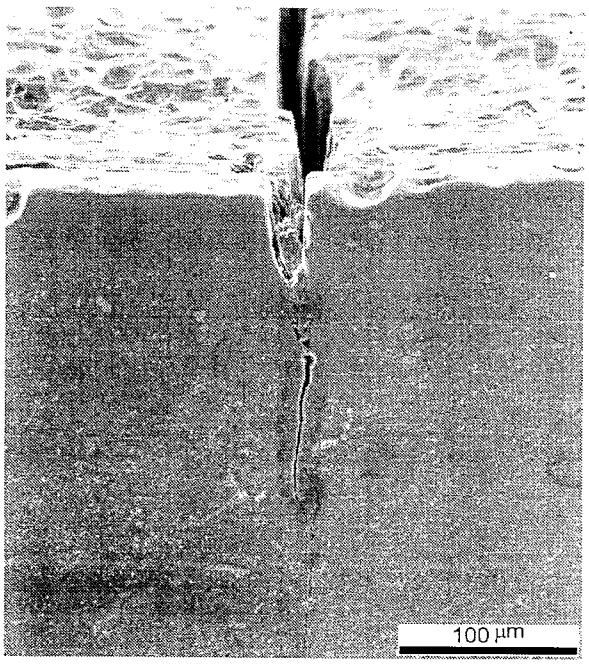

(b)

Figure D.2: SEM micrographs for Crack #1 in hole #107 on panel B3-2-2 taken for (a) Section 2 at 200X and (b) 30° tilted micrograph at 250X for Section 2.

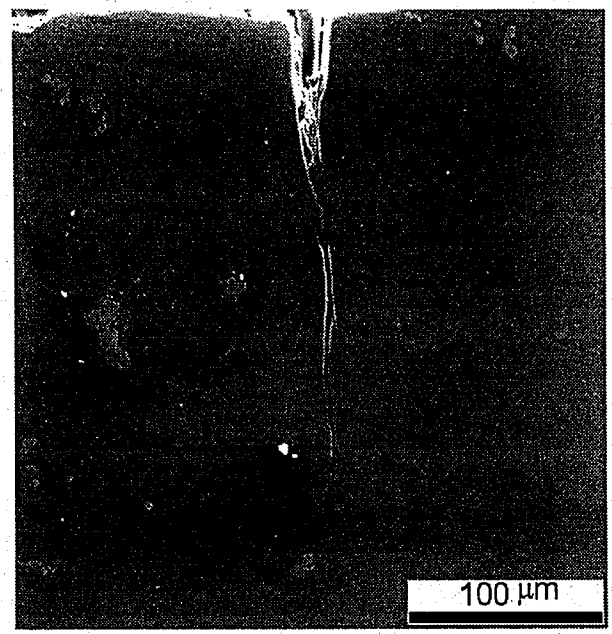

(a)

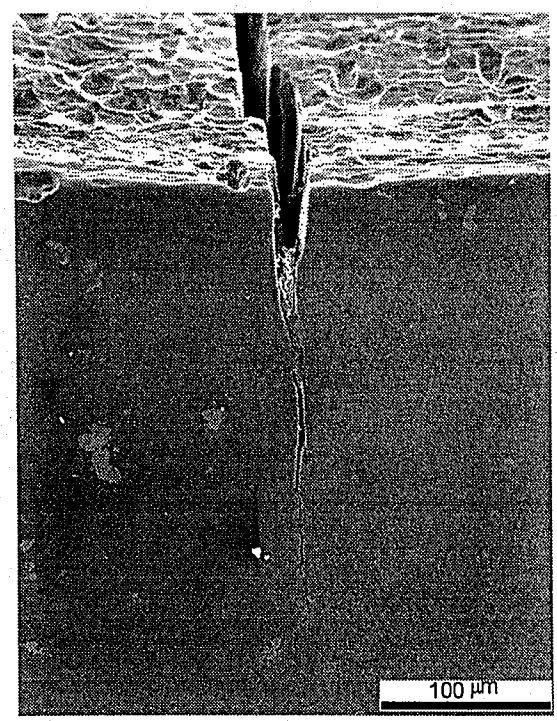

(b)

Figure D.3: SEM micrographs for Crack #1 in hole #107 on panel B3-2-2 taken for (a) Section 3 at 200X and (b) 30° tilted micrograph at 250X for Section 3.

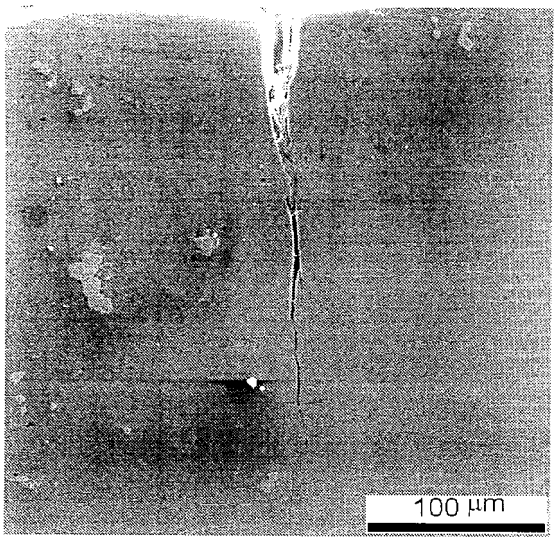

(a)

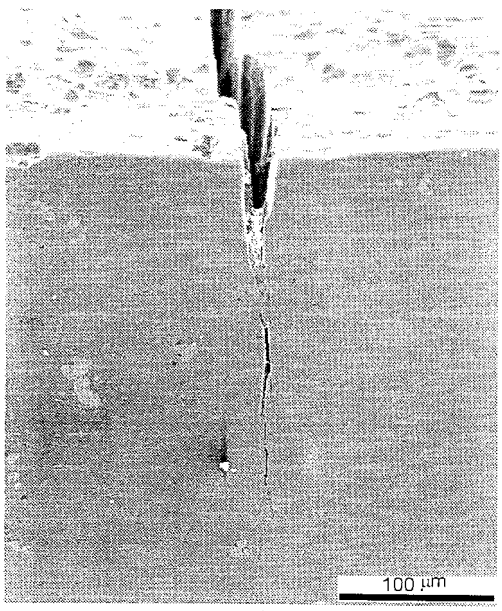

(b)

Figure D.3: SEM micrographs for Crack #1 in hole #107 on panel B3-2-2 taken for (a) Section 3 at 200X and (b) 30° tilted micrograph at 250X for Section 3.

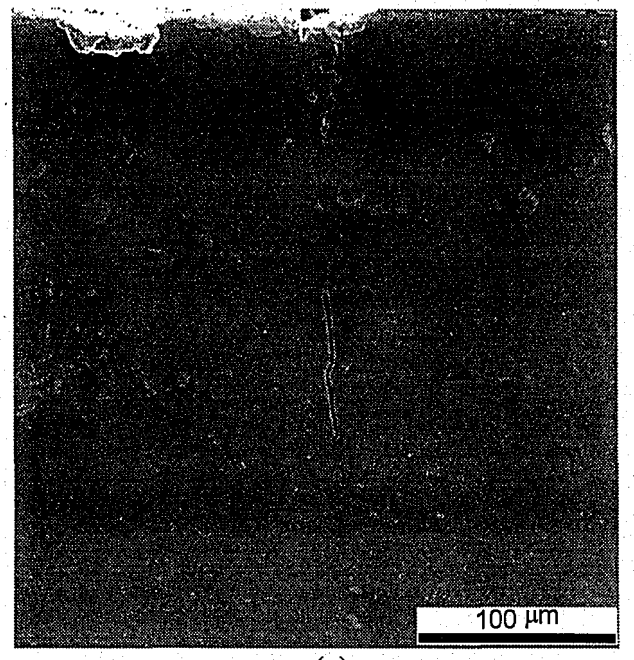

(a)

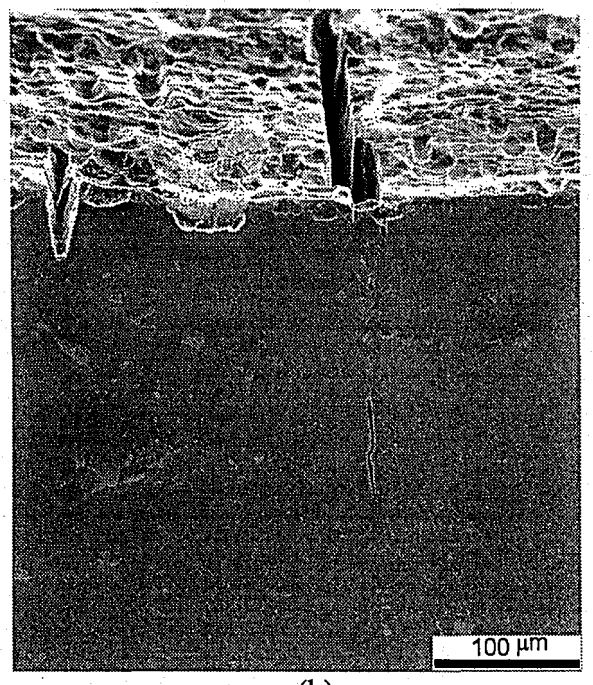

(b)

Figure D.4: SEM micrographs for Crack #1 in hole #107 on panel B3-2-2 taken for (a) Section 4 at 250X and (b) 30° tilted micrograph at 200X of Section 4.

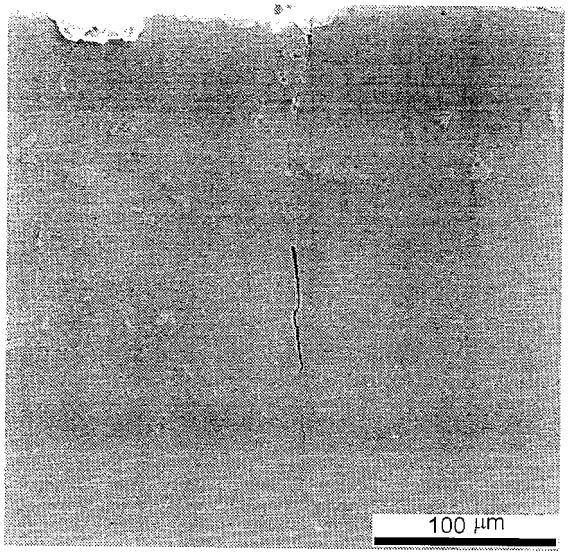

(a)

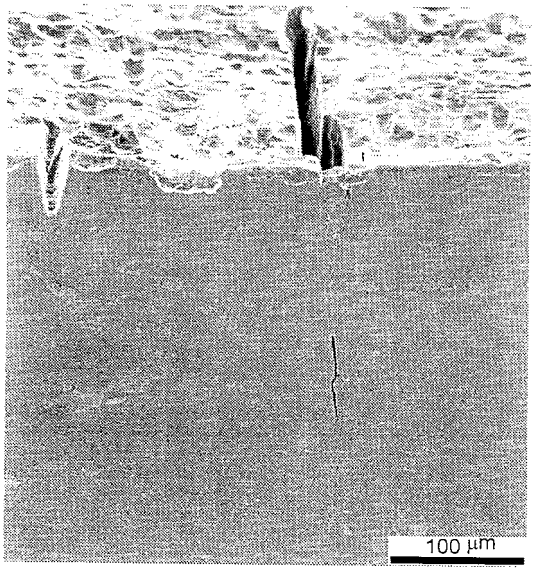

(b)

Figure D.4: SEM micrographs for Crack #1 in hole #107 on panel B3-2-2 taken for (a) Section 4 at 250X and (b) 30° tilted micrograph at 200X of Section 4.

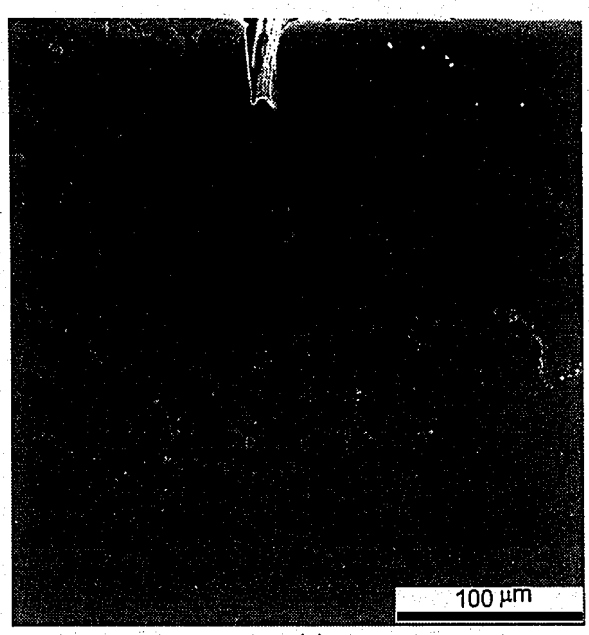

(a)

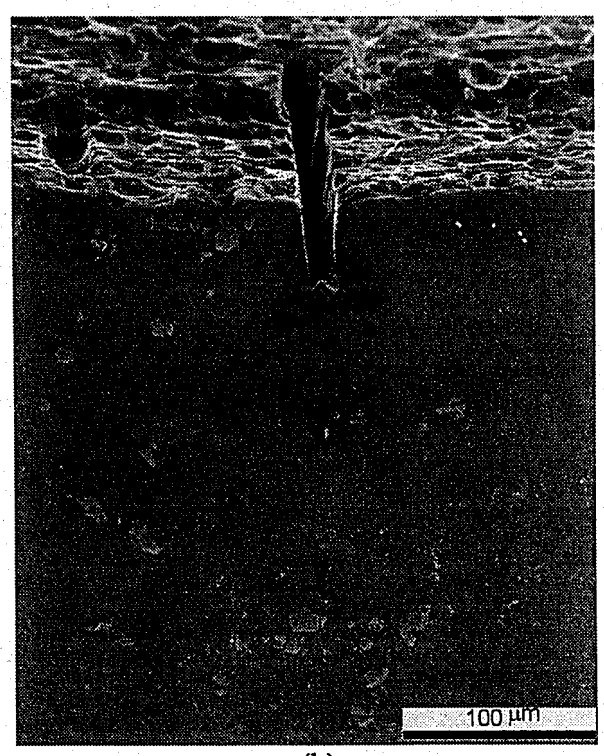

(b)

Figure D.5: SEM micrographs for Crack #1 in hole #107 on panel B3-2-2 taken for (a) Section 5 at 250X and (b) 30° tilted micrograph at 270X for Section 5.

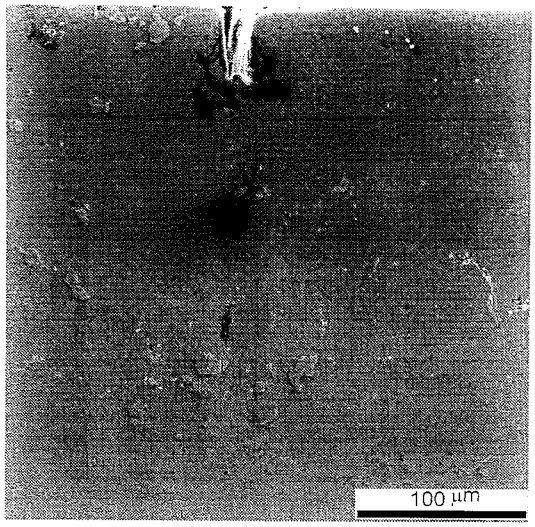

(a)

(b)

Figure D.5: SEM micrographs for Crack #1 in hole #107 on panel B3-2-2 taken for (a) Section 5 at 250X and (b) 30° tilted micrograph at 270X for Section 5.

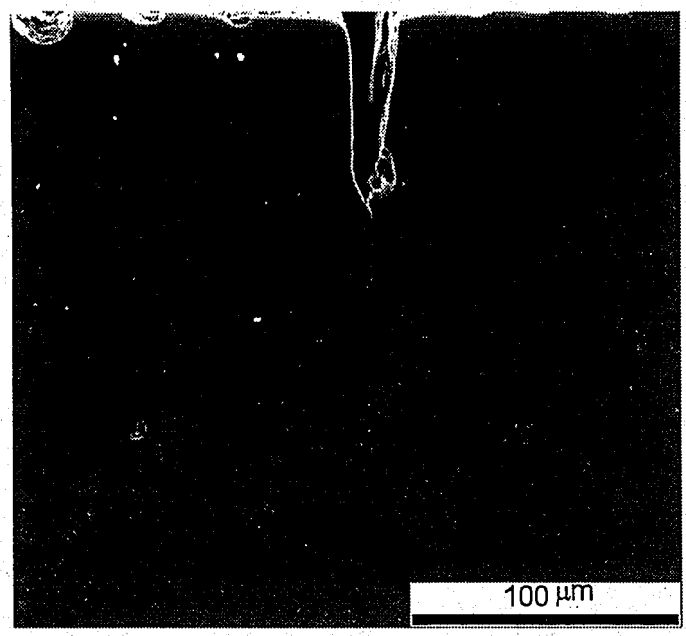

(a)

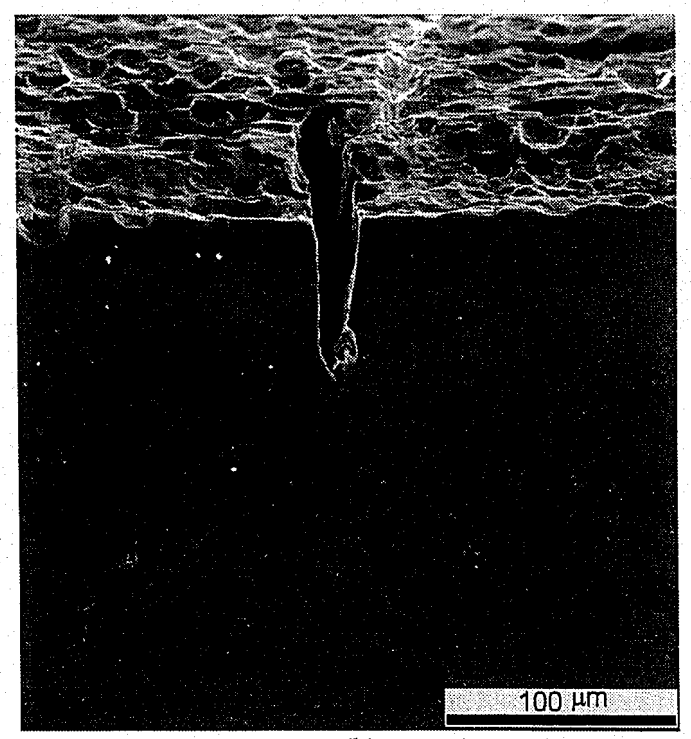

(b)

Figure D.6: SEM micrographs for Crack #1 in hole #107 on panel B3-2-2 taken for (a) Section 6 at 300X and (b) 30° tilted micrograph at 270X for Section 6.

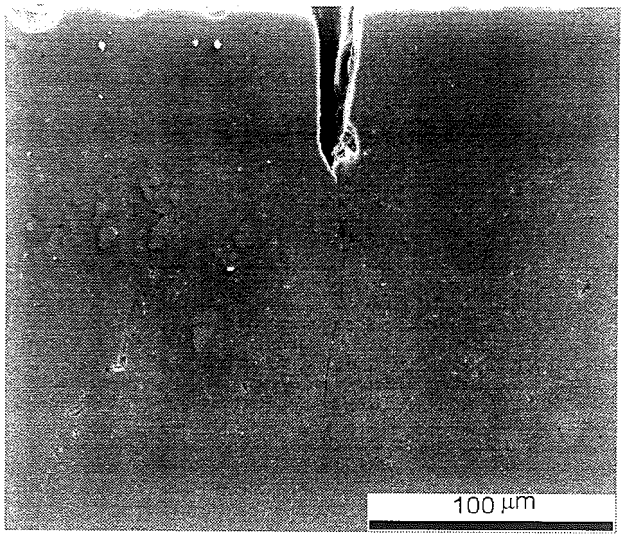

(a)

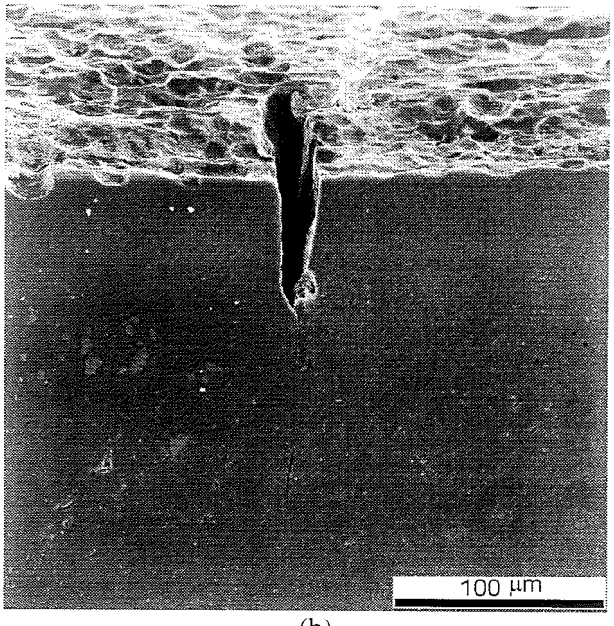

(b)

Figure D.6: SEM micrographs for Crack #1 in hole #107 on panel B3-2-2 taken for (a) Section 6 at 300X and (b) 30° tilted micrograph at 270X for Section 6.

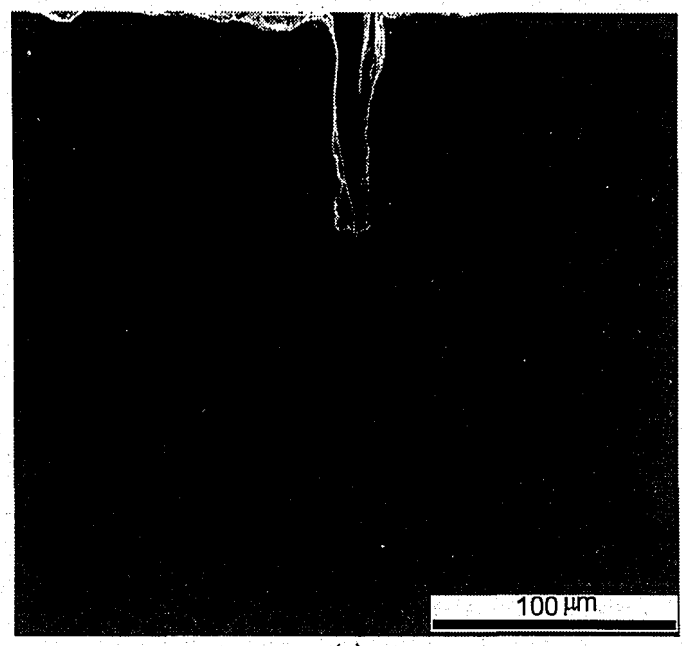

(a)

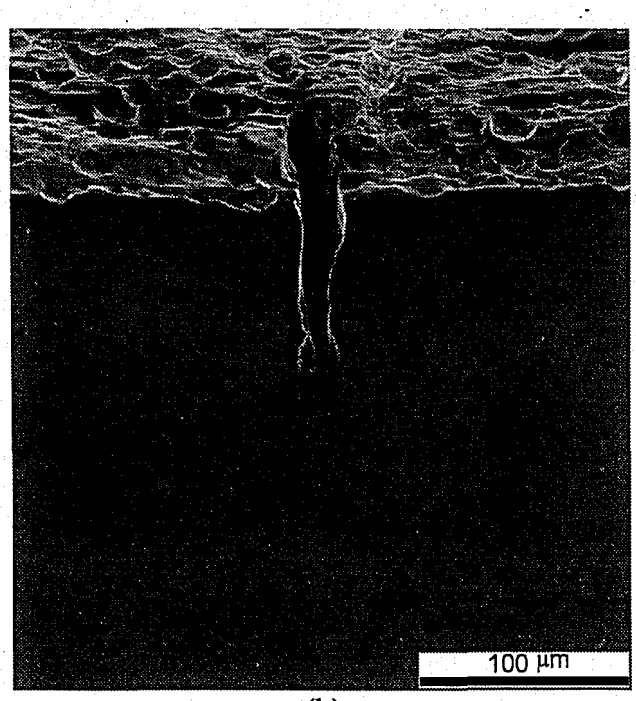

(b)

Figure D.7: SEM micrographs for Crack #1 in hole #107 on panel B3-2-2 taken for (a) Section 7 at 300X and (b) 30° tilted micrograph at 270X for Section 7.

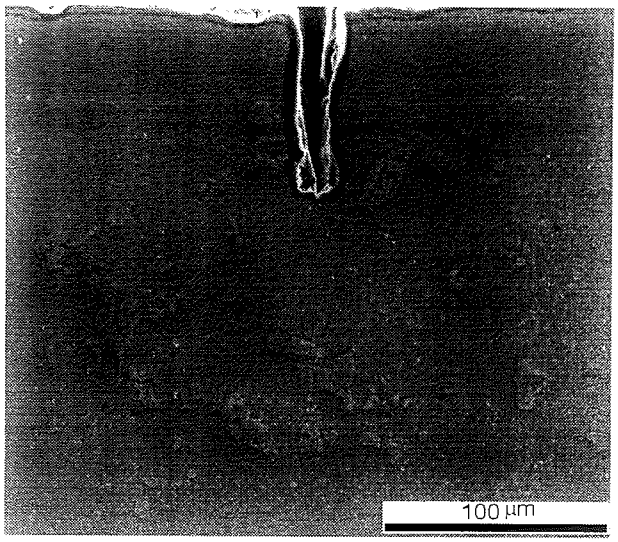

(a)

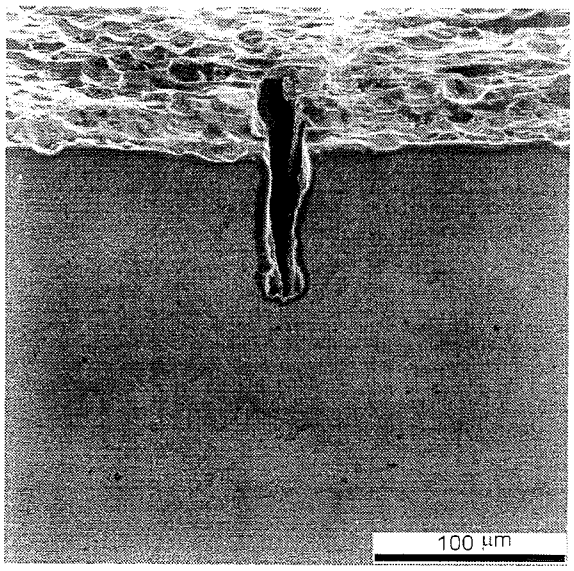

(b)

Figure D.7: SEM micrographs for Crack #1 in hole #107 on panel B3-2-2 taken for (a) Section 7 at 300X and (b) 30° tilted micrograph at 270X for Section 7.

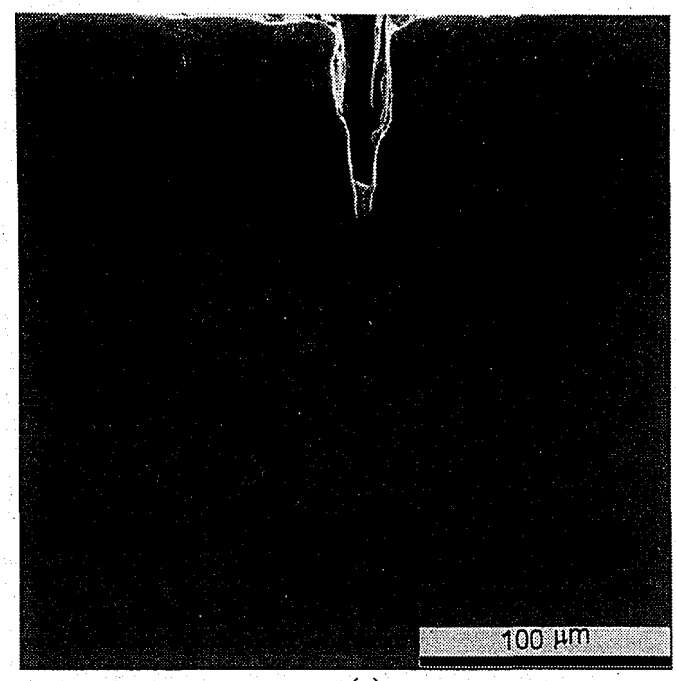

(a)

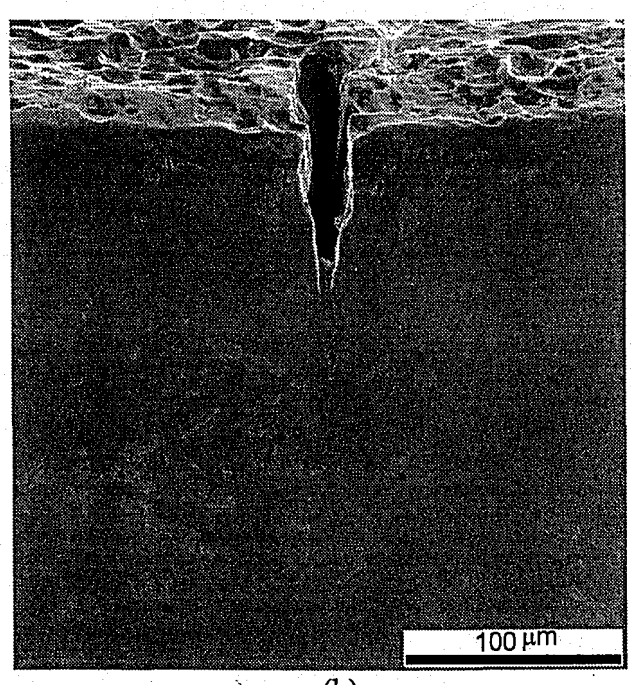

(b)

Figure D.8: SEM micrographs for Crack #1 in hole #32 on panel B3-2-2 taken for (a) Section 8 at 300X and (b) 30° tilted micrograph at 270X for Section 8.

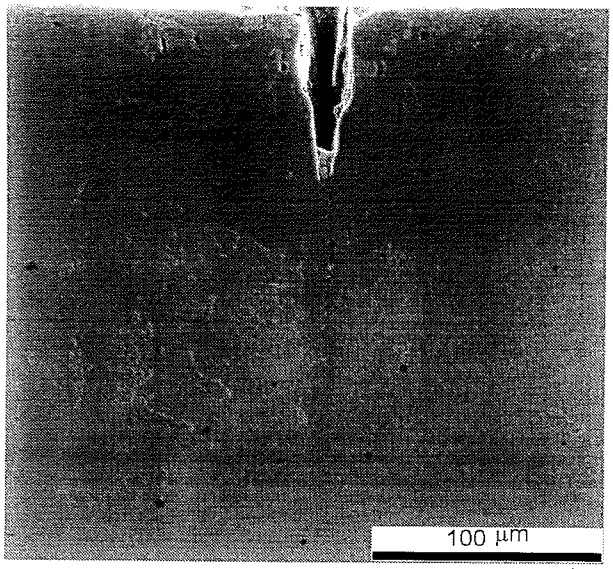

(a)

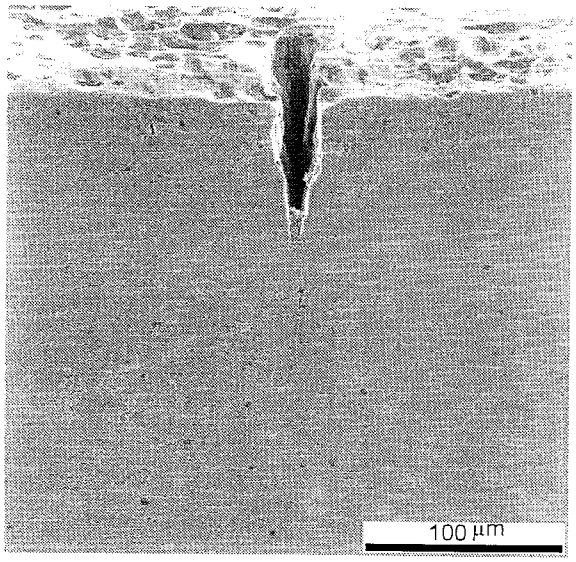

(b)

Figure D.8: SEM micrographs for Crack #1 in hole #32 on panel B3-2-2 taken for (a) Section 8 at 300X and (b) 30° tilted micrograph at 270X for Section 8.

APPENDIX E

SEM micrographs for Crack #2 in Hole #107 on Panel B3-2-2

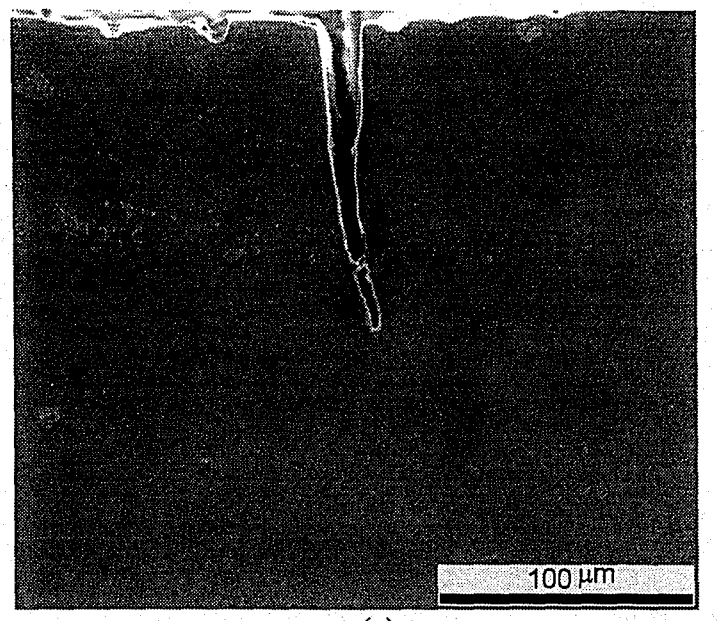

(a)

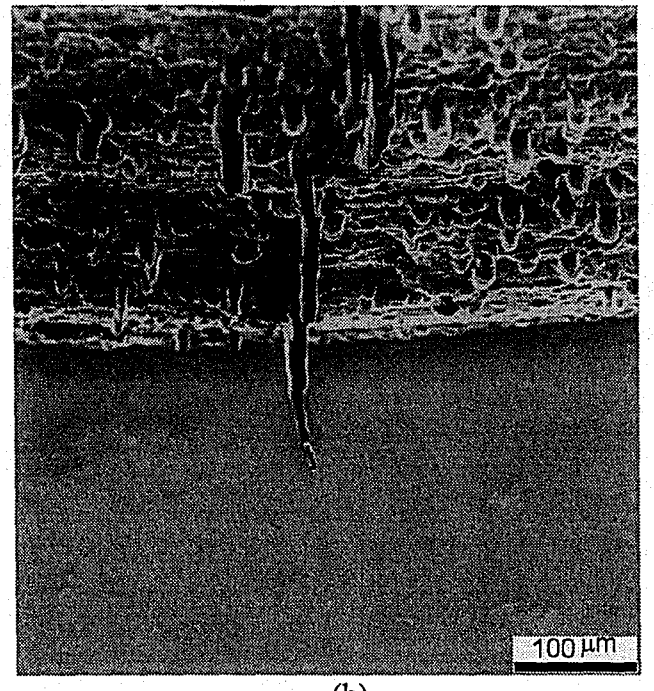

(b)

Figure E.1: SEM micrographs of Crack #2 in hole #107 on panel B3-2-2 taken for (a) Section 1 at 300X and (b) 45° tilted micrograph at 150X of Section 1.

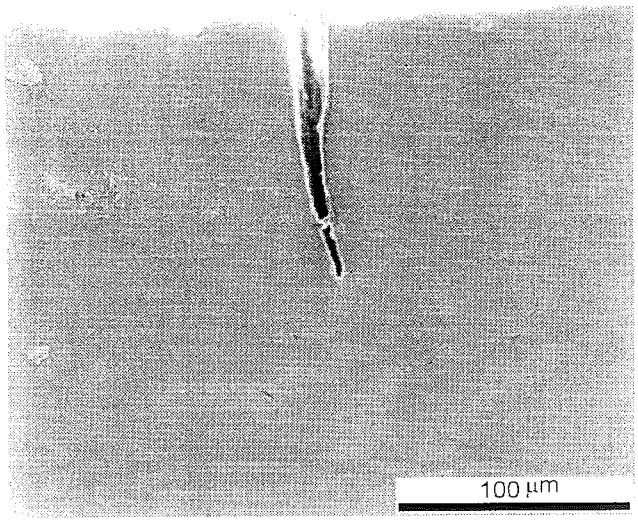

(a)

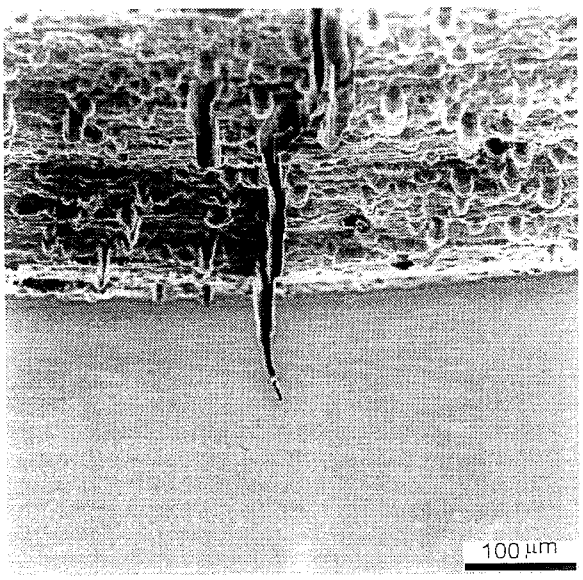

(b)

Figure E.1: SEM micrographs of Crack #2 in hole #107 on panel B3-2-2 taken for (a) Section 1 at 300X and (b) 45° tilted micrograph at 150X of Section 1.

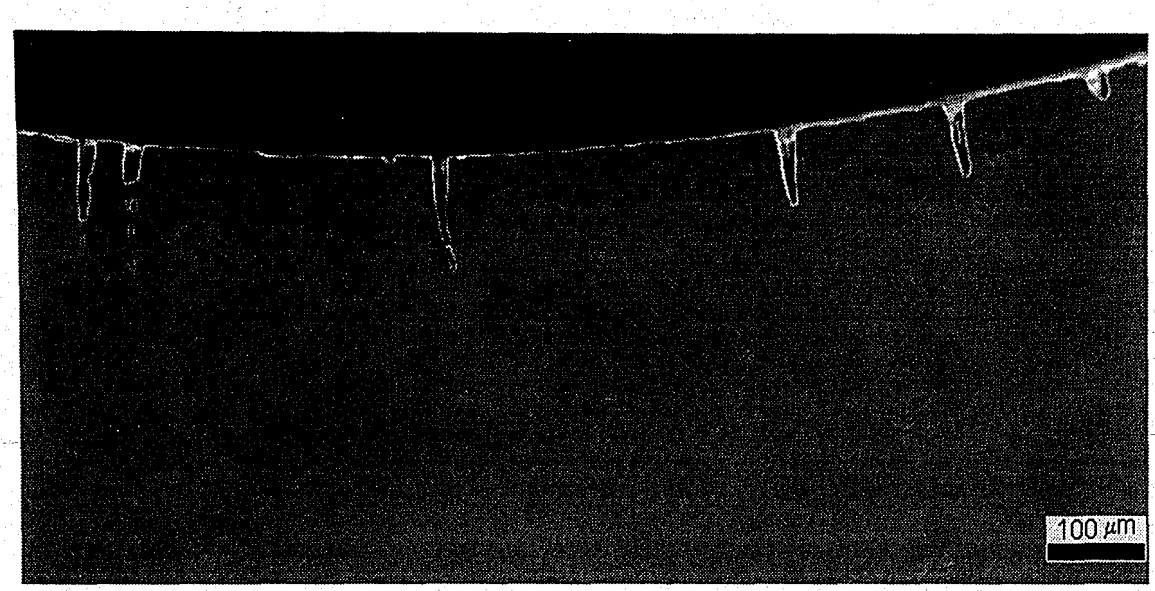

(c)

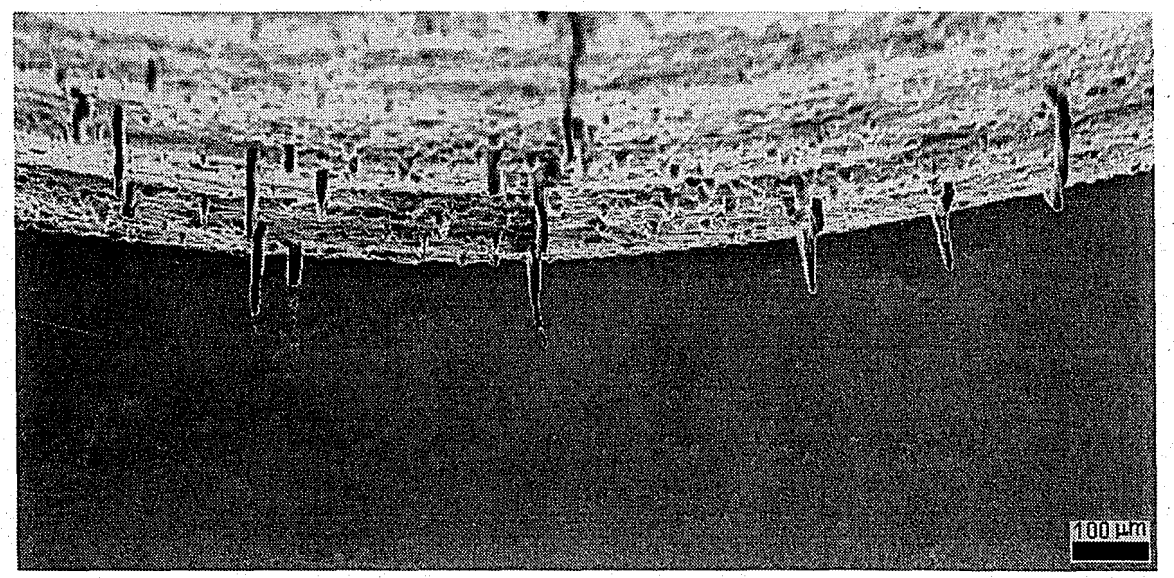

(d)

Figure E.1 (cont'd): SEM micrographs of Section 1 that show (c) several cracks are present at the section at 70X and (d) 30° tilted micrograph at 50X which shows the numerous cracks as well as Crack #2 at Section 1.

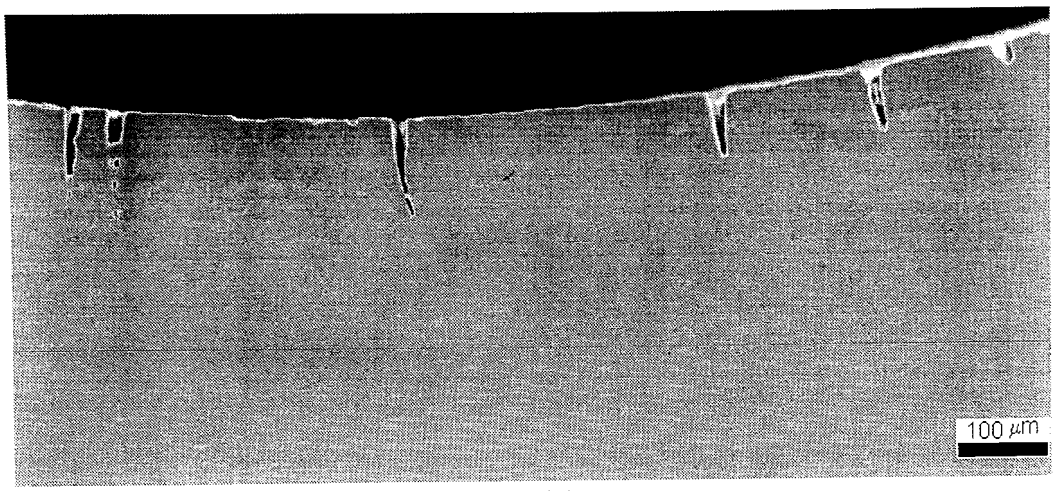

(c)

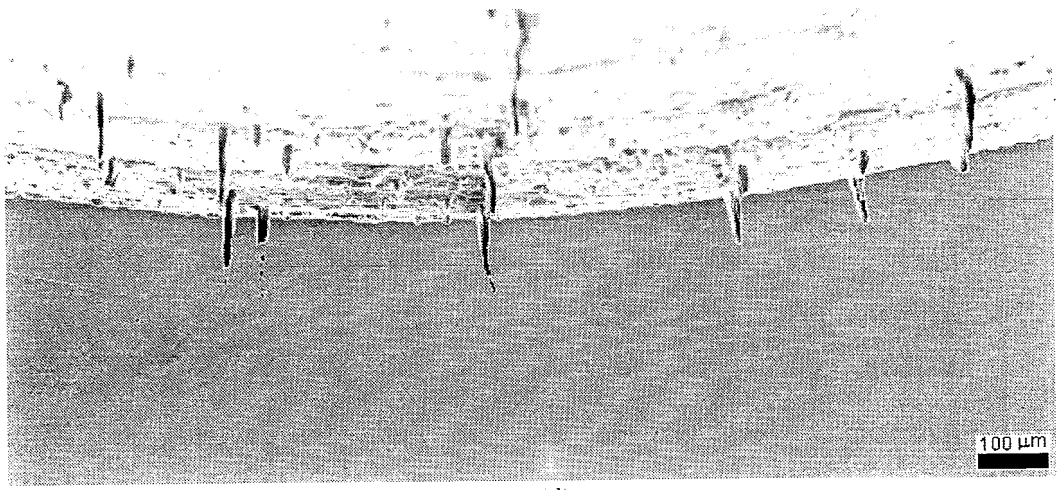

(d)

Figure E.1 (cont'd): SEM micrographs of Section 1 that show (c) several cracks are present at the section at 70X and (d) 30° tilted micrograph at 50X which shows the numerous cracks as well as Crack #2 at Section 1.

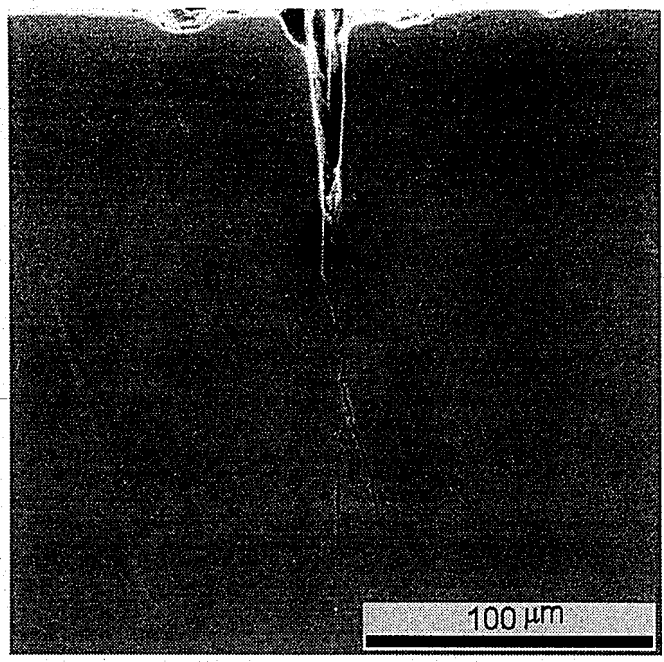

(a)

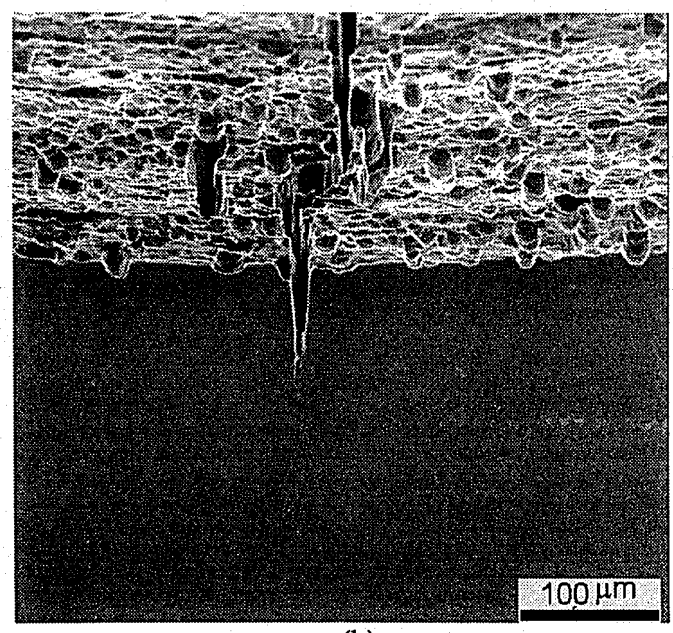

(b)

Figure E.2: SEM micrographs of Crack #2 in hole #107 on panel B3-2-2 that show (a) Section 2 with crack branching at 300X and (b) 30° tilted micrograph of Section 2 at 150X.

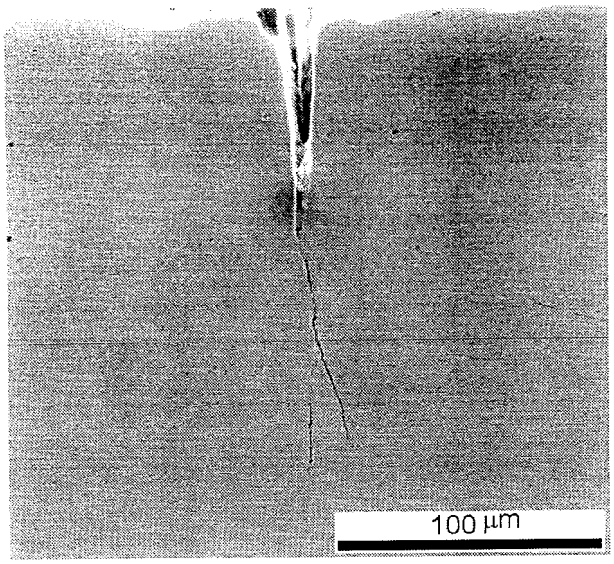

(a)

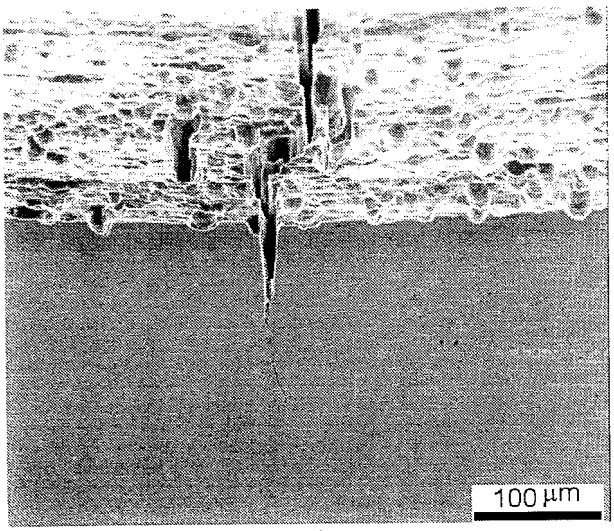

(b)

Figure E.2: SEM micrographs of Crack #2 in hole #107 on panel B3-2-2 that show (a) Section 2 with crack branching at 300X and (b) 30° tilted micrograph of Section 2 at 150X.

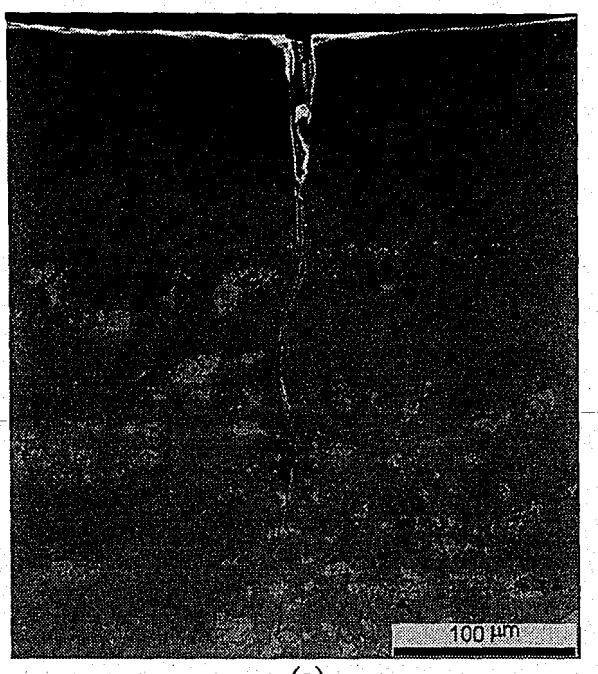

(a)

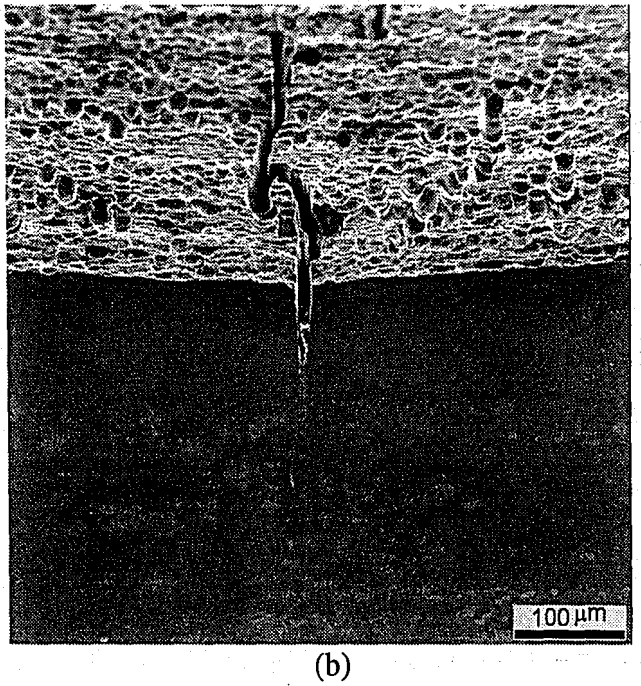

(b)

Figure E.3: SEM micrographs of Crack #2 in hole #107 on panel B3-2-2 that show (a) Section 3 at 270X and (b) 30° tilted micrograph at 150X of Section 3.

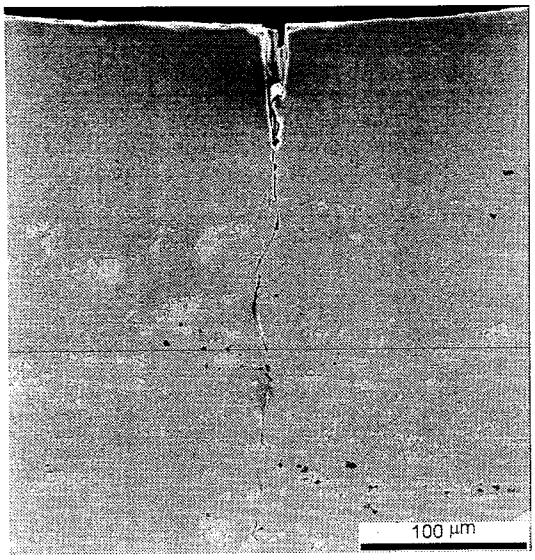

(a)

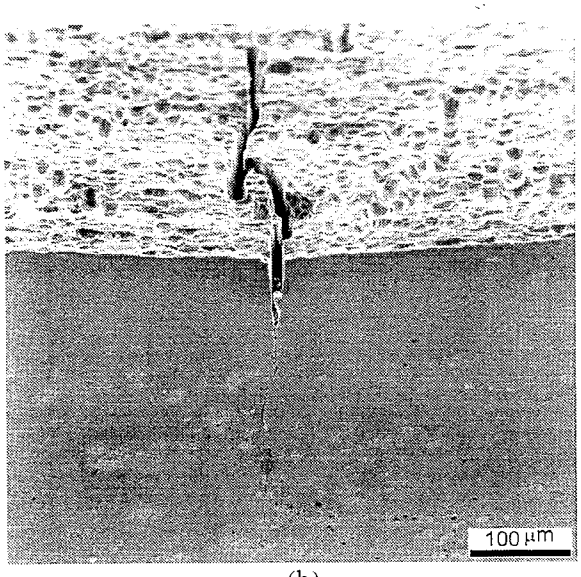

(b)

Figure E.3: SEM micrographs of Crack #2 in hole #107 on panel B3-2-2 that show (a) Section 3 at 270X and (b) 30° tilted micrograph at 150X of Section 3.

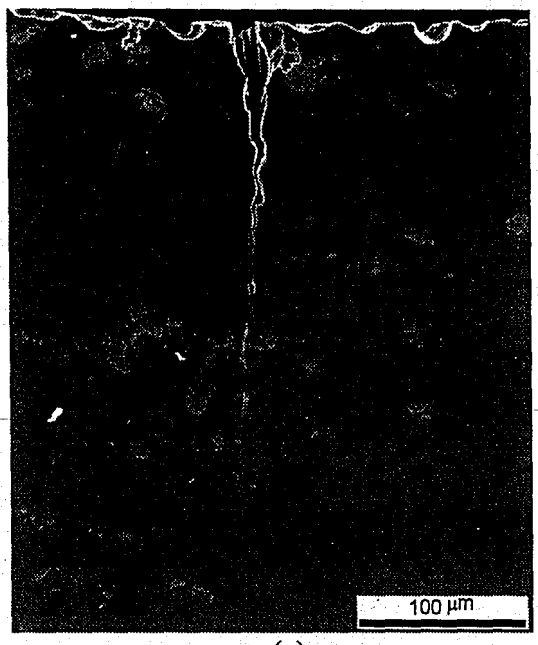

(a)

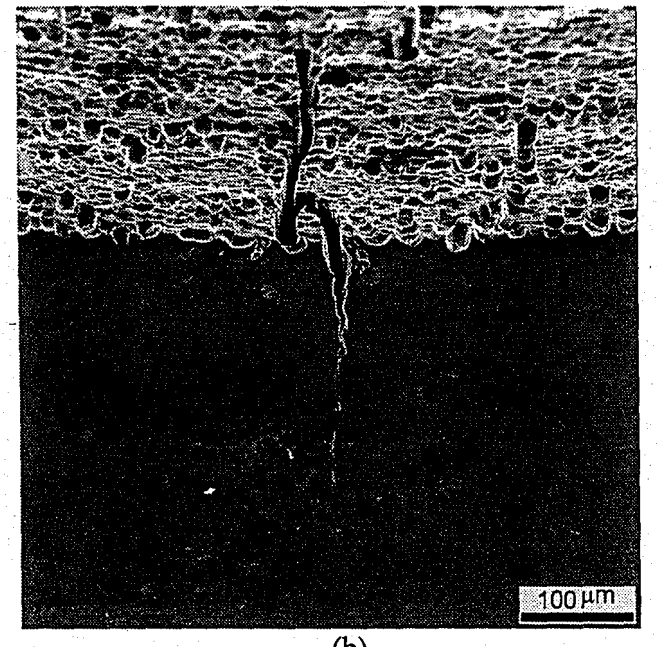

(b)

Figure E.4: SEM micrographs of Crack #2 in hole #107 on panel B3-2-2 that show (a) Section 4 at 270X and (b) 30° tilted micrograph at 150X of Section 4.

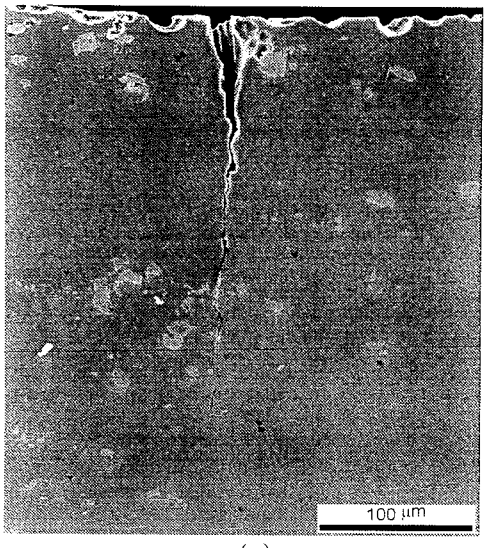

(a)

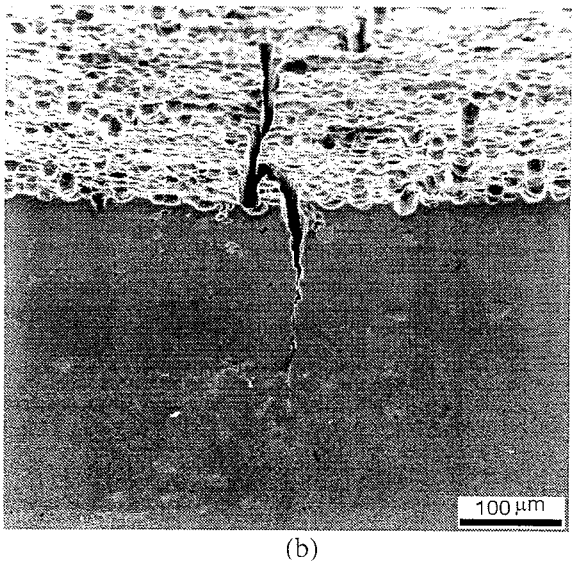

(b)

Figure E.4: SEM micrographs of Crack #2 in hole #107 on panel B3-2-2 that show (a) Section 4 at 270X and (b) 30° tilted micrograph at 150X of Section 4.

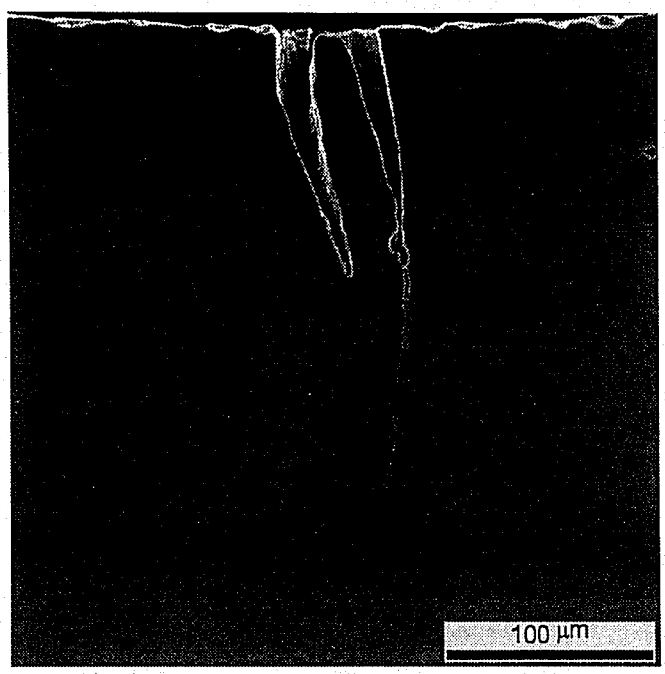

(a)

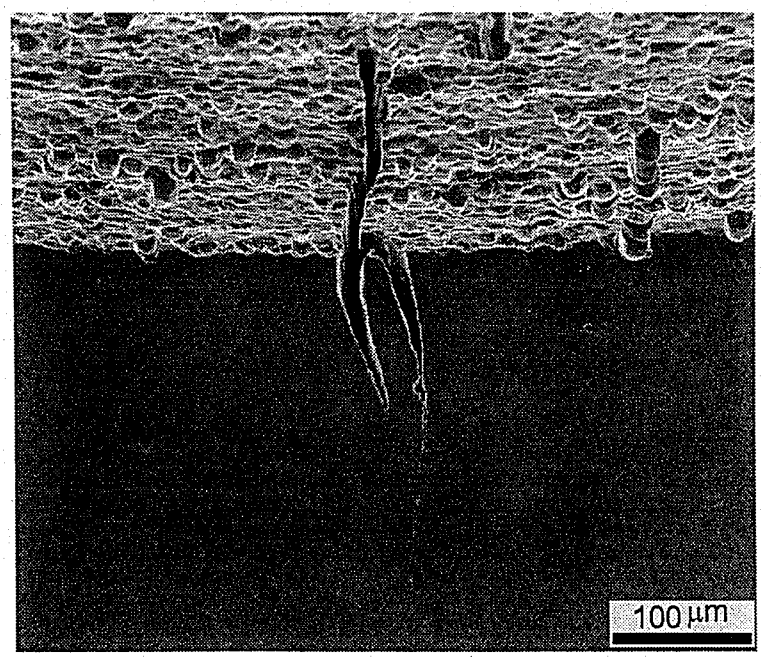

(b)

Figure E.5: SEM micrographs of Crack #2 in hole #107 on panel B3-2-2 that show (a) Section 5 and the link-up at 270X and (b) 30° tilted micrograph at 150X of Section 5 and the associated link-up.

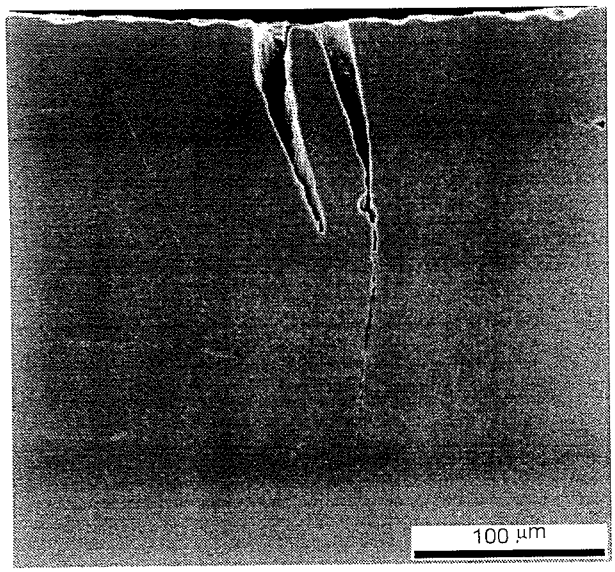

(a)

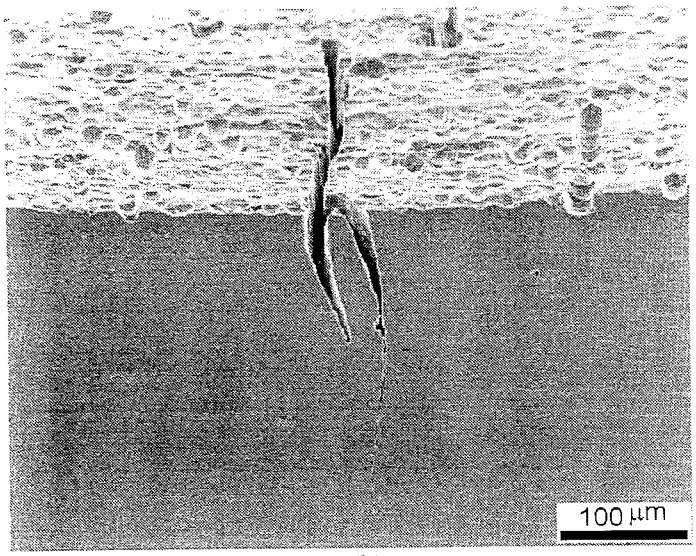

(b)

Figure E.5: SEM micrographs of Crack #2 in hole #107 on panel B3-2-2 that show (a) Section 5 and the link-up at 270X and (b) 30° tilted micrograph at 150X of Section 5 and the associated link-up.

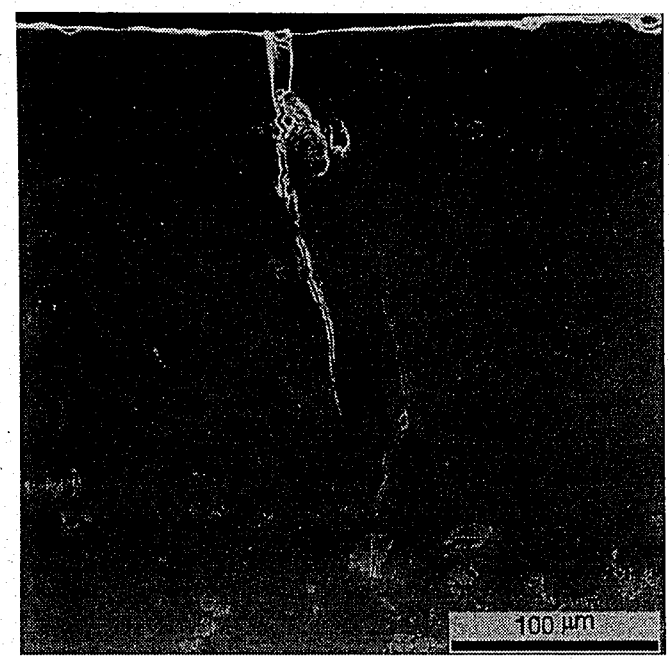

(a)

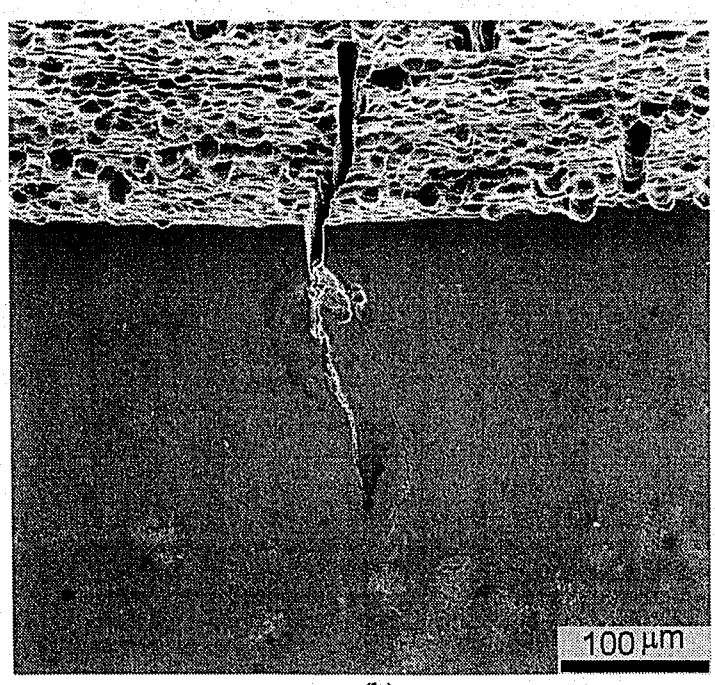

(b)

Figure E.6: SEM micrographs of Crack #2 in hole #107 on panel B3-2-2 to show (a) Section 6 at 270X and (b) 30° tilted micrograph at 150X of Section 6.

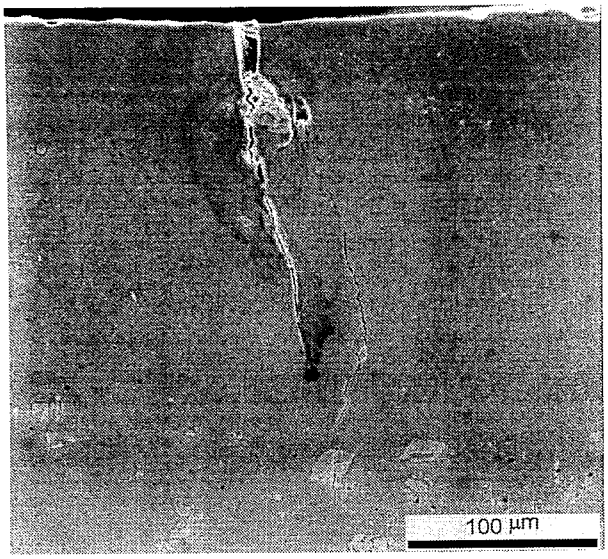

(a)

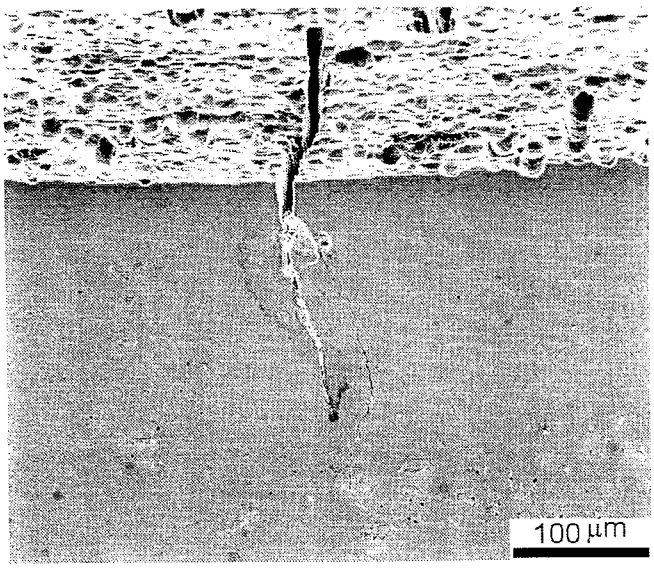

(b)

Figure E.6: SEM micrographs of Crack #2 in hole #107 on panel B3-2-2 to show (a) Section 6 at 270X and (b) 30° tilted micrograph at 150X of Section 6.

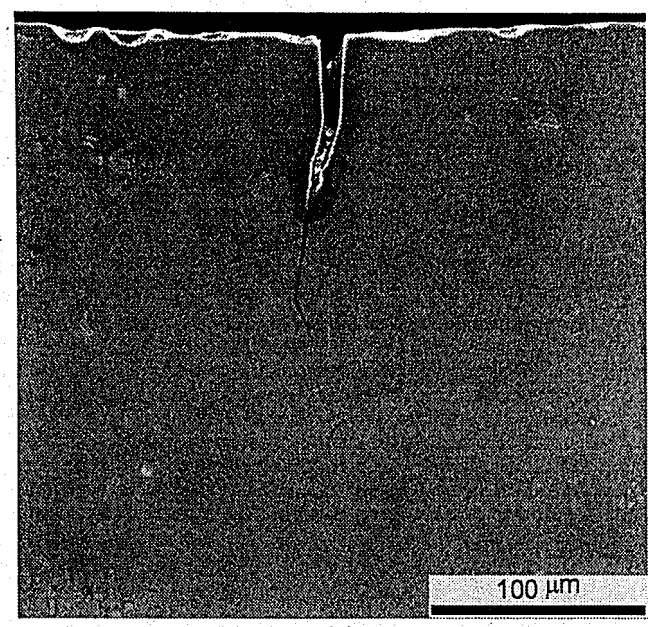

(a)

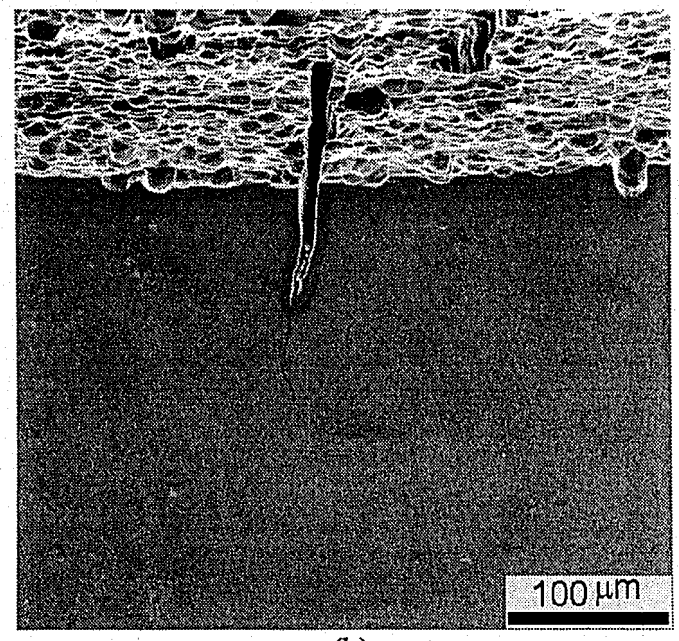

(b)

Figure E.7: SEM micrographs of Crack #2 in hole #107 on panel B3-2-2 that show (a) Section 7 at 270X and (b) 30° tilted mircograph at 150X of Section 7.

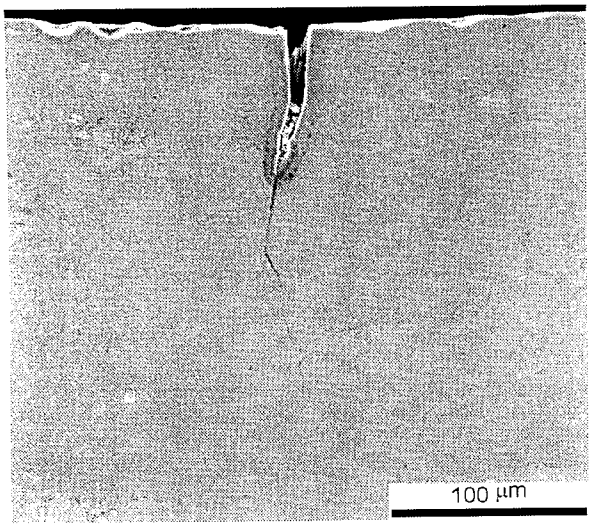

(a)

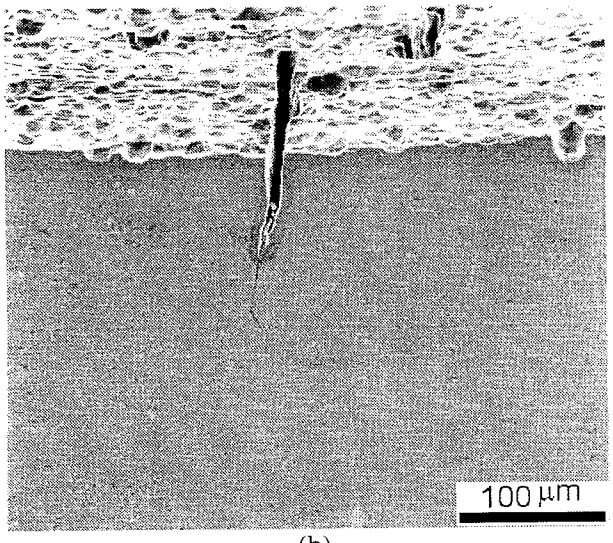

(b)

Figure E.7: SEM micrographs of Crack #2 in hole #107 on panel B3-2-2 that show (a) Section 7 at 270X and (b) 30° tilted mircograph at 150X of Section 7.

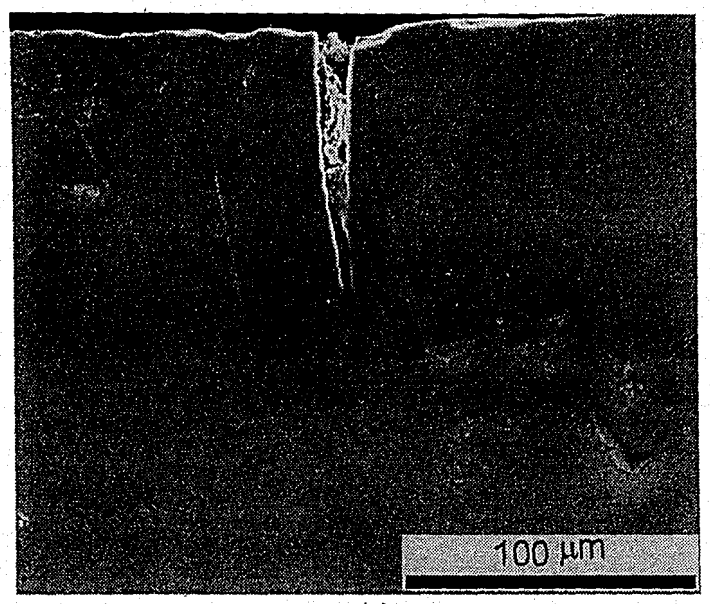

(a)

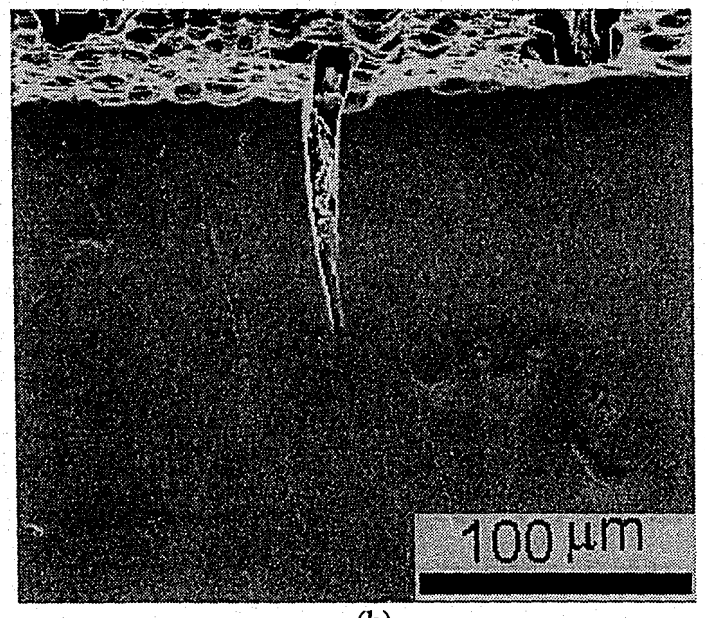

(b)

Figure E.8: SEM micrographs of Crack #2 in hole #107 on panel B3-2-2 to show (a) Section 8 at 270X and (b) 30° tilted micrograph of Section 8 at 250X.

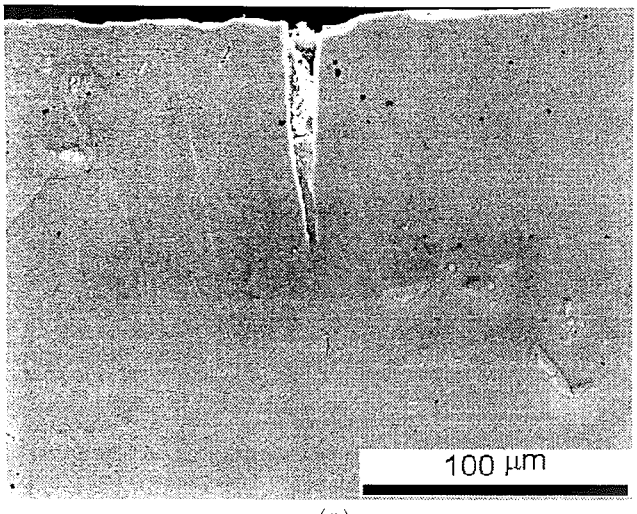

(a)

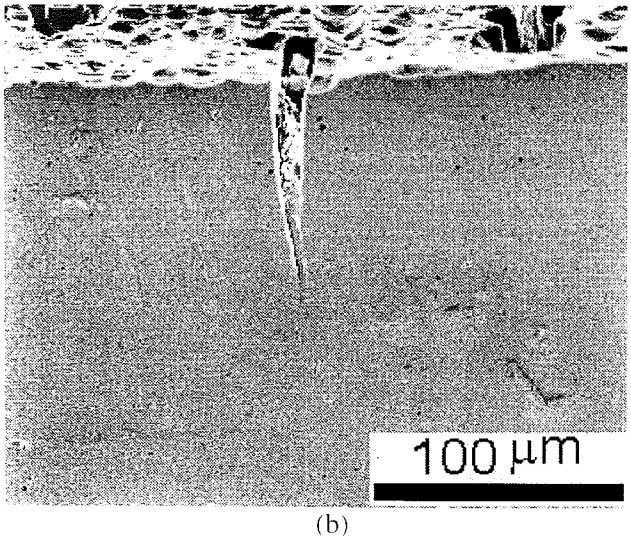

(b)

Figure E.8: SEM micrographs of Crack #2 in hole #107 on panel B3-2-2 to show (a) Section 8 at 270X and (b) 30° tilted micrograph of Section 8 at 250X.

REFERENCES

1. Wei, R.P., "Corrosion and Corrosion Fatigue of Airframe Materials," DOT/FAA/AR-00/22 Report, (2000).

2. Lee, B., "Influence of Pre-Existing Corrosion Pits on Fatigue Life in a 2024-T3 Aluminum Alloy," MS Thesis, Lehigh University, Bethlehem, PA., (1999).

3. Dolley, E.J., Lee, B., and Wei, R.P., "The Effect of Pitting Corrosion on Fatigue Life," submitted to *Fatigue and Fracture of Engineering Materials and Structures*, (1998).

4. Dolley, E.J., "Chemically Short-Crack Behavior of the 7075-T6 Aluminum Alloy," Ph.D Dissertation, Lehigh University, Bethlehem, PA., (1999).

5. Wei, R.P., "Corrosion and Corrosion Fatigue in Perspective," Chemistry and Electrochemistry of Stress Corrosion Cracking: A Symposium Honoring the Contributions of R.W. Staehle, TMS, (2001).

6. Jones, D.A., Principles and Prevention of Corrosion. Upper Saddle River: Prentice Hall, (1996).

7. Haigh, B.P., "Experiments on the Fatigue of Brasses," *Journal of the Institute of Metals*, Vol. 18, pp. 55-86, (1917).

8. Moore, R.P., "Effect of Corrosion Upon the Fatigue Resistance of Thin Duralumin," *ASTM Tentative Standards*, Vol. 27, No. 11, pp. 128-133, (1927).

9. Gough, H.J., and Sopwith, D.G., "Atmospheric Action as a Factor in Fatigue of Metals," *Journal of the Institute of Metals*, Vol. 49, pp. 93-122, (1932).

10. Wei, R.P., "Corrosion Fatigue – Science and Engineering," Keynote Paper for the Conference on Recent Advances in Corrosion Fatigue, Sheffield, UK, (1997).

11. Chen, G.S., Gao, M., and Wei, R.P., "Microconstituent-Induced Pitting Corrosion in a 2024-T3 Aluminum Alloy," *Corrosion*, Vol. 52, pp. 8-15, (1996).

12. Sih, G.C., Mechanics of Fatigue Initiation and Propagation. Boston: Kluwer Academic, (1991).

13. Erdogan, F., and Paris, P., "A Critical Analysis of Crack Propagation Laws," *Journal of Basic Engineering, Transactions of the ASME*, Vol. 85, pp. 528-534, (1963).

14. Wei, R.P., "Some Aspects of Environment-Enhanced Fatigue Crack Growth," *Engineering Fracture Mechanics*, Vol. 1, pp. 633-651, (1970).

15. Crack Growth Life Prediction Program, AFGROW, http://fibec.flight.wpafb.af.mil/fibec/afgrow.html, (1997).

16. Hoeppner, D.W., "Model for Prediction of Fatigue Lives Based upon a Pitting Corrosion Fatigue Process," *Fatigue Mechanisms*, STP 675, Fong, T.J., eds., ASTM, Philadelphia, PA, p. 841, (1979).

17. Muller, M., "Theoretical Considerations on Corrosion Fatigue Crack Initiation," *Metallurgical Transactions*, Vol. 13A, p. 649, (1982).

18. Harlow, D.G., Domanowski, L.D., Dolley, E.J., and Wei, R.P., "Probability Modeling and Analysis of J-Stars Tear-down Data from Two B707 Aircraft," (1999).

19. Hug, A.J. *et al.*, "Laboratory Inspection of Wing Lower Surface Structure from 707 Aircraft for the J-STARS Program," Boeing FSCM No. 81205, Document No. D500-12947-1, (1996).

20. Wei, R.P., and Harlow, D.G., "Probabilities of Occurance and Detection and Airworthiness Assessment," ICAF '99 Paper, (1999).

21. Pilkey, W.D., Peterson's Stress Concentration Factors. New York: John Wiley and Sons, Inc., (1997).

VITA

Mary Chilton (Mollie) Latham was born on April 2, 1977 to Joseph and Margaret Latham in Hornell, NY. She graduated from Deerfield Academy in Deerfield, MA in 1995. That fall, Mollie matriculated at Bucknell University in Lewisburg, PA where she was an undergraduate major in Mechanical Engineering. While at Bucknell, Mollie was an active member of the William Cameron Engine Company, Lewisburg's volunteer fire department. She earned her Pennsylvania Emergency Medical Technician certification in 1996 and was awarded the Ambulance Attendant of the Year award in 1997 for her dedication and ability as an EMT.

Mollie was also active in the College of Engineering, having served as the chapter president for Tau Beta Pi, the National Engineering Honor Society, from 1998-1999. She also was a teaching assistant for courses in FORTRAN, Kinematics, Thermodynamics, and Science of Materials. Mollie received the Ernest and Josephine Christensen award for Outstanding Engineering Graduates, and graduated with summa cum laude honors from Bucknell University with a Bachelor of Science degree in Mechanical Engineering in May 1999.

Mollie began her graduate studies at Lehigh University in Bethlehem, PA in August 1999 under the guidance of Professor Robert P. Wei. Her thesis topic is on the corrosion fatigue damage in the fastener holes of a torn-down Boeing 707 wing panel that was in service for 24 years. She was awarded a P.C. Rossin Fellowship during the first year of her graduate work, and was a recepient of a National Science Foundation Graduate Research Fellowship in the year 2000. Mollie will receive her Master of Science in Mechanical Engineering from Lehigh University in June 2001.

END

OF

TITLE